TOWARD UNDERSTANDING AND MODELING COMPRESSIBILITY EFFECTS ON VELOCITY GRADIENTS IN TURBULENCE

A Dissertation

by

SAWAN SUMAN

Submitted to the Office of Graduate Studies of
Texas A&M University
in partial fulfillment of the requirements for the degree of

DOCTOR OF PHILOSOPHY

December 2009

Major Subject: Aerospace Engineering

TOWARD UNDERSTANDING AND MODELING COMPRESSIBILITY EFFECTS ON VELOCITY GRADIENTS IN TURBULENCE

A Dissertation

by

SAWAN SUMAN

Submitted to the Office of Graduate Studies of
Texas A&M University
in partial fulfillment of the requirements for the degree of

DOCTOR OF PHILOSOPHY

Approved by:

Chair of Committee,	Sharath S. Girimaji
Committee Members,	Hamn-Ching Chen
	Rodney D. W. Bowersox
	Simon W. North
Head of Department,	Dimitris C. Lagoudas

December 2009

Major Subject: Aerospace Engineering

ABSTRACT

Toward Understanding and Modeling Compressibility Effects on Velocity Gradients in Turbulence. (December 2009)

Sawan Suman, B.Tech., Indian Institute of Technology-Kanpur, India

Chair of Advisory Committee: Dr. Sharath S. Girimaji

Development of improved turbulence closure models for compressible fluid flow simulations requires better understanding of the effects of compressibility on various underlying processes of turbulence. Fundamental studies of turbulent velocity gradients hold the key to understanding several non-linear processes like material element deformation, energy cascading, intermittency and mixing. Experiments, direct numerical simulation (DNS) and simple mathematical models are three approaches to study velocity gradients. With the goal of furthering our understanding of the effects of compressibility on turbulent velocity gradients, this dissertation (i) employs DNS results to characterize some of the effects of compressibility on turbulent velocity gradients, and (ii) develops simple mathematical models for velocity gradient dynamics in compressible turbulence.

In the first part of the dissertation, effects of compressibility on velocity gradient invariants and the local topology of compressible turbulence are characterized employing DNS results of compressible decaying isotropic turbulence. Joint statistics of second and third invariants of velocity gradient tensor and the exact probability of occurrence of associated topologies conditioned upon dilatation (degree of compression/expansion of fluid) are computed. These statistics are found to be (i) highly dependent on dilatation and (ii) substantially different from the statistics observed in incompressible turbulence. These dilatation-conditioned statistics of compressible turbulence, however, are found to be fairly independent of Mach number and Reynolds

number.

In the second part of the dissertation, two mathematical models for compressible velocity gradient dynamics are developed. To take into account the significant aero-thermodynamic coupling that exists in compressible flows, the models are derived explicitly using the continuity, energy and state equations, along with the momentum equation. The modeling challenge involved in the development of these models lies in capturing the inherently non-local nature of pressure and viscous effects as a function of local terms to derive a closed set of ordinary differential equations. The models developed in this dissertation are evaluated in a variety of flow regimes - incompressible limit (low Mach number); pressure-released limit (extremely high Mach number); and intermediate (sub-sonic Mach numbers) - and are shown to recover a range of known compressibility effects.

To Jesus, the Almighty

ACKNOWLEDGMENTS

I would like to thank my advisor, Dr. Sharath Girimaji, for teaching me the subject of fluid turbulence. I express my earnest gratitude to him for providing me continuous guidance, encouragement and support during the five years of my Ph.D. program. I also thank my committee members, Dr. Rodney Bowersox, Dr. Hamn-Ching Chen, and Dr. Simon North. Their comments and advice have been essential for this dissertation.

I want to express my thankfulness to Dr. Jacques Richard for many valuable suggestions that I have received from him for improving the presentation of my research. Thanks are due to all the graduate students of Dr. Girimaji's research group. Working and interacting with them has been an extremely pleasant and an educative experience for me. I would also like to thank Dr. Walter Haisler, Ms. Karen Knabe, and Ms. Colleen Leatherman, for helping me meet all the official requirements of my graduate studies.

I thank my parents, my sisters, and my brother-in-law, for the encouragement and emotional support that I received from them. Special thanks are due to my friends Gaurav Kumar and Jyothsana Chandramohan, who helped me overcome many of the non-academic challenges that I faced during the last year of my Ph.D. program. Their ever-available support in tackling these challenges enabled me to stay focused on my research work.

TABLE OF CONTENTS

CHAPTER Page

LIST OF TABLES

TABLE Page

LIST OF FIGURES

FIGURE Page

FIGURE Page

FIGURE Page

CHAPTER I

INTRODUCTION

Development of improved turbulence closure models for compressible flow computations relies on our ability to understand the underlying physics of various processes and the influence of compressibility on these processes. Examination of velocity gradients offers a viable route to understanding several important non-linear turbulence phenomena such as energy cascade, scalar mixing, material element deformation and intermittency. This dissertation attempts to advance the current understanding of the effects of compressibility on turbulent velocity gradients.

Velocity gradient tensor is an exact representation of the deformation rate of a fluid element. While the symmetric part of velocity gradient tensor - the strain-rate tensor - represents the rate of stretching of a fluid element, the anti-symmetric portion – the rotation-rate tensor – represents the rate of rotation, or equivalently vorticity, associated with a fluid element. On the other hand, trace of the velocity gradient tensor or dilatation represents the rate of change in the volume of a fluid element. In incompressible flows, dilatation is identically zero. However, in compressible flows dilatation can assume a range of values across the flow domain: positive values for expanding fluid elements; and negative values for contracting ones. Invariants of the velocity gradient tensor can be used to directly infer the local streamline pattern/local topology of flow, thus aiding in flow visualization [1]. Some of the most popular vortex eduction techniques – required for isolating and understanding coherent structures of a turbulent flow field – rely on the knowledge of velocity gradient invariants [2, 3]. Topology of a turbulent flow field is intrinsically interesting, not only as an aid

---

This dissertation follows the style of Journal of Turbulence.

to flow visualization, but also, provides insight into material element deformation and mixing. A non-focal topology will deform a fluid element and lead to increased mixing. A focal-topology, on the other hand, will merely re-orient a fluid element without significant increase in mixing. On the other hand, magnitude and sign of the principal strain-rates reveal the nature of self-straining of a fluid element. Orientation of the vorticity vector, with respect to the strain-rate eigenvectors, influences the extent of vortex stretching. This in turn leads to generation of smaller length scales in a flow field and the associated transfer of kinetic energy from large to smaller scales of motion [4, 5]. Interaction of vorticity vector with strain-rate tensor also influences the orientation tendencies of scalar gradients, thus influencing mixing [5]. The phenomenon of intermittency is related to the localized magnification of velocity gradients [6]. Higher order structure tensor functions of velocity gradients can be employed to directly study many features of anisotropic turbulence [7].

Experimental observations, direct numerical simulations (DNS) and mathematical models are three approaches to studying velocity gradients in a turbulent flow field. Each of these modes has advantages and disadvantages. Recent developments in non-invasive methods [8] have enabled experiments to capture velocity gradient data with high accuracy. However, availability of experimental data is limited and often restricted to small regions in a flow field. In recent years, direct simulation of Navier - Stokes equations has emerged as a powerful tool to simulate turbulent flow field over large volumes. Though DNS computations do provide an almost time-continuous, domain-spanning data of the velocity gradient field, the computational demand for such simulations is quite high, especially at large Reynolds numbers. A mathematical model for the evolution of velocity gradient tensor is the third alternative for studying velocity gradient physics. Such a model is expected to be a closed set of autonomous ordinary differential equations and can provide a very simple, although less accurate,

way to study the evolution of velocity gradients. Moreover, such a model – owing to its Lagrangian nature – can prove to be a more intuitive method to develop insights into velocity gradient physics and the non-linear processes of turbulence. Another advantage of having a velocity gradient model is that it can provide a direct closure for the stochastic methods of turbulence computations [9, 10].

A. Literature review

The research presented in this dissertation can be categorized into two parts. In the first part (Chapter II), DNS results are employed to characterize the effects of compressibility on velocity gradient invariants and the related local topology of compressible turbulence. In the second part (Chapters III and IV), mathematical models for compressible velocity gradient dynamics are developed. Accordingly, in this section separate literature reviews corresponding to these two parts of the dissertation are presented.

1. Effects of compressibility on velocity gradient invariants and local topology

Motivated by the need for a general classification methodology to categorize flow topology, Chong et al. [11] proposed a scheme based on the three invariants (P, Q, R) of velocity gradient tensor. Employing this scheme, the local streamline pattern or the local topology of the velocity field can be inferred. Subsequently, Soria et al. [12] studied the joint statistical distributions of Q and R at small scales of motion in incompressible mixing layers. They found that the scatter plot of the second and third invariants has two prominent features: (i) a significant amount of data lies in lower right quadrant, and (ii) the bulk of data lies in the upper left quadrant roughly distributed uniformly over an elliptical region. The local topologies associated

with these two regions are unstable node/saddle/saddle and stable focus stretching (described in detail in Chapter II). These prominent topological features immediately attracted considerable research attention and were later found to be quite robust across a variety of turbulent flows: in high symmetry flow by Boratav et al. [13]; boundary layer flow by Chacin et al. [14]; channel flow by Blackburn et al. [15]; and turbulent/non-turbulent interface by da Silva et al. [16]. In addition to inferring the dominant local topologies, invariant studies have also been used by several workers to develop more insightful understanding of turbulence. Boratav et al. [13] suggested the usefulness of studying turbulence statistics conditioned on the value of Q, as this quantity directly corresponds to the right hand side of the Poisson equation for pressure. Thus, such conditioning can isolate the role of pressure. Chacin et al. [14] identified the strong association of various production mechanisms with the sign of the discriminant, D ($\equiv 27R^2/4 + Q^3$). Soria et al. [17] explained the preferred vorticity alignment tendencies and the preferred sign of the intermediate strain-rate using volume integrals of the invariants. O'Neill et al. [18] studied the association between scalar dissipation and topological structures. Kobayashi et al. [19] used a normalized form of the second invariant Q to develop a subgridscale (SGS) model for large eddy simulation (LES) applications.

All the above cited works are in the context of incompressible turbulence wherein the first invariant, P (which is the additive inverse of dilatation) is zero. Some studies have been performed for compressible turbulence as well. Chen et al. [20] and Cantwell et al. [21] studied the dynamics of invariants and the associated flow topologies in compressible wakes and flames. Chen et al. [22] examined the statistics of second and third invariants in a compressible mixing layer. Maekawa et al. [23] studied flow patterns/local topologies in decaying isotropic compressible turbulence and reported the percentage occurrence of various flow patterns conditioned on the

sign of dilatation. Miura [24] performed a comparative study of compressible and incompressible decaying turbulence in terms of (a) vortical structures and (b) root mean square of the fluctuations in Q. Pirozzoli et al. [25] studied the invariants of the traceless anisotropic portion of the velocity gradient tensor in compressible isotropic turbulence.

In all these studies of compressible turbulence, however, the effect of the first invariant (P) on the statistics of the second and third invariants has largely been ignored. As mentioned before, P being the additive inverse of dilatation, is trivially zero in incompressible flows. However, in compressible flows it can be considerably different from zero. A non-zero P signifies the degree of compression/expansion of a fluid element, and thus is a very significant quantity in compressible turbulence. Maekawa et al.[23] does consider the first invariant, but is concerned only with the sign of P, but not with the magnitude of P.

Recently, Suman et al. [26] and Lee et al. [27] have demonstrated the strong dependence of strain-rate statistics on normalized dilatation in compressible turbulence. Previous studies [22] of compressible velocity gradients fields at low and moderate Mach numbers concluded that the overall statistics of second and third invariants are very similar to the behavior seen in incompressible turbulence. As discussed in [27], this behavior may be due to the following two factors: (i) the dilatational component of velocity gradient in these studies is small; and (ii) the effects of positive and negative dilatation may be canceling each other, thus showing no significant difference between the overall statistics of incompressible and compressible turbulence. This scenario can substantially change at higher Mach numbers. Lee et al. [27] demonstrate that the percentage occurrence of a non-zero dilatation value steadily grows as Mach number increases in decaying isotropic turbulence. Moreover, with increasing Mach number, more extreme values (both positive and negative) are encountered

in the domain. Therefore, it is reasonable to expect that at very high Mach numbers, overall turbulence behavior can be substantially different from incompressible turbulence.

These studies [26, 27] prompt the following questions: (i) are the statistics of second and third invariants also strongly dependent on normalized dilatation? (ii) how does this dependence change at different levels of normalized dilatation? (iii) what are the preferred local topologies at different non-zero dilatations? (iv) How do the initial parameters, such as Mach number and Reynolds number, influence this dependence? The first part of the dissertation (Chapter II) attempts to answer these questions.

2. Development of mathematical models for compressible velocity gradient dynamics

The first attempt to derive a Lagrangian model for velocity gradient dynamics in incompressible turbulence was made by Vieillefosse [4]. This model - called the restricted Euler equation (REE) - is based on the Euler equation and is an autonomous system of ordinary differential equations describing the nonlinear velocity gradient dynamics in incompressible flows. Ashurst et al. [5] demonstrated that REE accurately captures many important features of velocity gradient geometry seen in DNS of homogeneous shear and decaying isotropic turbulence. Subsequently, several modifications have been proposed to enhance the REE. Cantwell [28] presented invariant maps of velocity gradient tensor to develop more insight into the tensor geometry. Cantwell [29] also proposed a modeled form of the neglected pressure effects and demonstrated that this modification captures some additional features of velocity gradient physics seen in DNS results. Girimaji et al. [7] identified a limitation in the original REE in the context of non-zero mean flows and proposed modified REE to

ensure momentum conservation. Also, a computational strategy to circumvent the problem of finite-time singularity was developed. Chertkov et al. [30] proposed an improvement to REE based on Lagrangian tetrad dynamics. Jeong et al. [31] incorporated further physics into the REE to take into account the viscous effects and consequently, removed the finite-time singularity problem altogether. Recently, Li et al. [6] have used the restricted Euler dynamics to propose a simple nonlinear dynamical model to explain the origins of intermittency in turbulent flows. Furthermore, Chevillard et al [32], Biferale et al. [33] and Chevillard et al. [34] have used a more unified approach to model both the anisotropic pressure Hessian and viscous effects employing Eulerian-Lagrangian change of variables (also used by Jeong et al. [31] to model viscous effects) and the so-called "recent fluid deformation closure". With these modifications, REE reproduces several stationary statistics of incompressible velocity gradients seen in DNS. Overall, REE is emerging as an important analytical tool for studying various turbulence mechanisms in incompressible flows.

However, even in its most advanced form, REE is fundamentally unsuited for modeling velocity gradient dynamics in compressible flows. The modeled pressure Hessian tensor in REE hinges on the Poisson equation and involves no thermodynamic considerations. The interaction of pressure with velocity field plays an important role in velocity gradient dynamics. In incompressible flows, the pressure field depends exclusively upon velocity field via the Poisson equation. The restricted Euler model takes advantage of this fact and closes the pressure Hessian in terms of the velocity gradient itself by completely neglecting the anisotropic portion of the tensor. In compressible flows the pressure field evolution is dictated by state and energy equations. Variations in temperature and density manifest on the turbulent velocity field via pressure effects. The momentum and energy equations become coupled, and thermodynamics can significantly influence the velocity field. A velocity gradi-

ent model for compressible flow field must necessarily take into account this coupling between turbulence and thermodynamics. The REE approximation, which hinges on the Poisson equation, is fundamentally unsuited for extension to compressible flows. Thus, there is a need to develop a suitable model, which can be used for compressible turbulent flows. Unlike REE, such a model requires the explicit inclusion of energy and state equations along with the continuity and momentum equations. The challenge involved in developing such models lies in capturing the inherently non-local nature of pressure and viscous effects as a function of local terms to derive a closed set of autonomous ordinary differential equations.

B. Dissertation goals

In light of the literature review presented above, the following two goals are identified for this dissertation.

(1) The first goal of the dissertation is to characterize the effects of compressibility on velocity gradient invariants and the local topology of compressible turbulence. Toward this end, the following specific objectives are pursued: (i) examination of the dependence of the joint statistics of second and third invariants of velocity gradient tensor on dilatation (degree of compression/expansion of a fluid element) in compressible decaying isotropic turbulence, (ii) identification of the predominant topologies at various levels of normalized dilatation, and (iii) evaluation of the dependence of conditional statistics on initial turbulent Mach number and Reynolds number. Furthermore, the performance of a recently developed model for compressible velocity gradients – homogenized Euler equation [26] - is evaluated against the behavior seen in DNS.

(2) The second goal of the dissertation is to develop mathematical models to com-

pute the evolution of velocity gradients in compressible turbulence. Toward this goal, two models are developed: (a) homogenized Euler equation (HEE); and (b) enhanced homogenized Euler equation (EHEE). The HEE model ignores all the non-local effects on the evolution of velocity gradients and can be considered base line model for compressible velocity gradients. On the other hand, in the EHEE model, several non-local pressure and viscous effects are included. Both models are extensively evaluated in various flow regimes - incompressible, intermediate and pressure-released – against a range of available DNS and analytical results of turbulence.

The dissertation is organized into 5 chapters. In Chapter II the effects of compressibility on velocity gradient invariants is characterized. In Chapter III the HEE model is developed and evaluated. Chapter IV presents an account of the development and evaluation of the EHEE model. Chapter V concludes the dissertation with a summary.

CHAPTER II

EFFECTS OF COMPRESSIBILITY ON VELOCITY GRADIENT INVARIANTS AND LOCAL TOPOLOGY OF TURBULENCE

The objectives of this chapter are (i) to examine the dependence of the joint statistics of second and third invariants of velocity gradient tensor on dilatation in compressible decaying isotropic turbulence, (ii) to identify the predominant topologies at various levels of normalized dilatation, and (iii) to evaluate the dependence of the conditional statistics on initial turbulent Mach number and Reynolds number. Furthermore we also investigate whether the invariant statistics seen in direct numerical simulation (DNS) of compressible turbulence can be recovered by a recently proposed model (homogenized Euler equation [26]) for compressible velocity gradient dynamics.

The organization of this chapter is as follows. Section B includes an overview of the three-dimensional phase space of P, Q and R and the methodology of inferring the local flow topology. Section C, D include results from DNS and HEE computations, respectively.

A. The phase space of $P - Q - R$ and topology of compressible turbulence

The local topology at a point in a flow field can be deduced with a knowledge of the eigenvalues (λ_i) of the local velocity gradient tensor, A_{ij} [11]. These eigenvalues satisfy the following characteristic equation:

$$\lambda^3 + P\lambda^2 + Q\lambda + R = 0 \tag{2.1}$$

The quantities P, Q and R appearing in (2.1) are the first, second and third invariants of A_{ij}:

$$\begin{aligned} P \equiv -tr[A] &= -S_{ii}; \\ Q \equiv \frac{1}{2}\left(P^2 - tr[A^2]\right) &= \frac{1}{2}\left(P^2 - S_{ij}S_{ji} - W_{ij}W_{ji}\right); \\ R &= \frac{1}{3}\left(-P^3 + 3PQ - S_{ij}S_{jk}S_{ki} - 3W_{ij}W_{jk}S_{ki}\right). \end{aligned} \quad (2.2)$$

The quantities S_{ij} and W_{ij} represent the strain-rate and rotation rate tensors respectively: $S_{ij} \equiv \frac{1}{2}\left(A_{ij} + A_{ji}\right)$ and $W_{ij} \equiv \frac{1}{2}\left(A_{ij} - A_{ji}\right)$. The characteristic equation (2.1) has three roots. The nature of solution and the local flow topology can be categorized based on these roots. The possibilities are: (i) all real and distinct roots; (ii) all real and two equal roots; (iii) all real and equal roots ; and (iv) one real and two complex conjugate roots. However, to infer category of solution we do not need to solve the characteristic equation. Topology can be directly inferred using the properties of $P - Q - R$ space and the values of the invariants P, Q and R.

Chong et al. [11] explain that the $P - Q - R$ space is partitioned into different spatial regions by a set of surfaces. Each of these regions corresponds to a particular category of the solution of the characteristic equation and hence is associated with a particular topology. The surface that separates the regions of real and complex roots is:

$$27R^2 + \left(4P^3 - 18PQ\right)R + \left(4Q^3 - P^2Q^2\right) = 0. \quad (2.3)$$

This surface can be split into two surfaces $S1a$ and $S1b$, which osculate each other to form a cusp. The equations for $S1a$ and $S1b$ are:

$$\frac{1}{3}P\left(Q - \frac{2}{9}P^2\right) - \frac{2}{27}\left(-3Q + P^2\right)^{\frac{3}{2}} - R = 0; \quad (2.4)$$

$$\frac{1}{3}P\left(Q\frac{2}{9}P^2\right) + \frac{2}{27}\left(3Q + P^2\right)^{\frac{3}{2}} - R = 0. \quad (2.5)$$

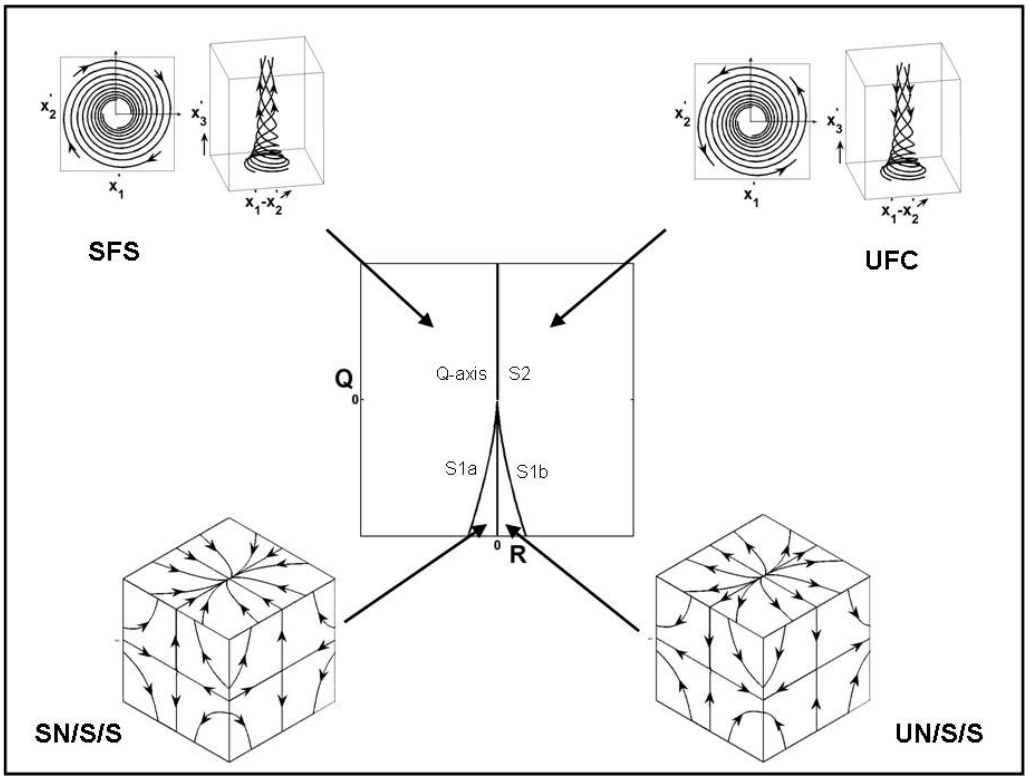

Fig. 1. Regions on the $p = 0$ ($A_{ii} = 0$) plane and the corresponding flow patterns. Description of acronyms provided in Table I.

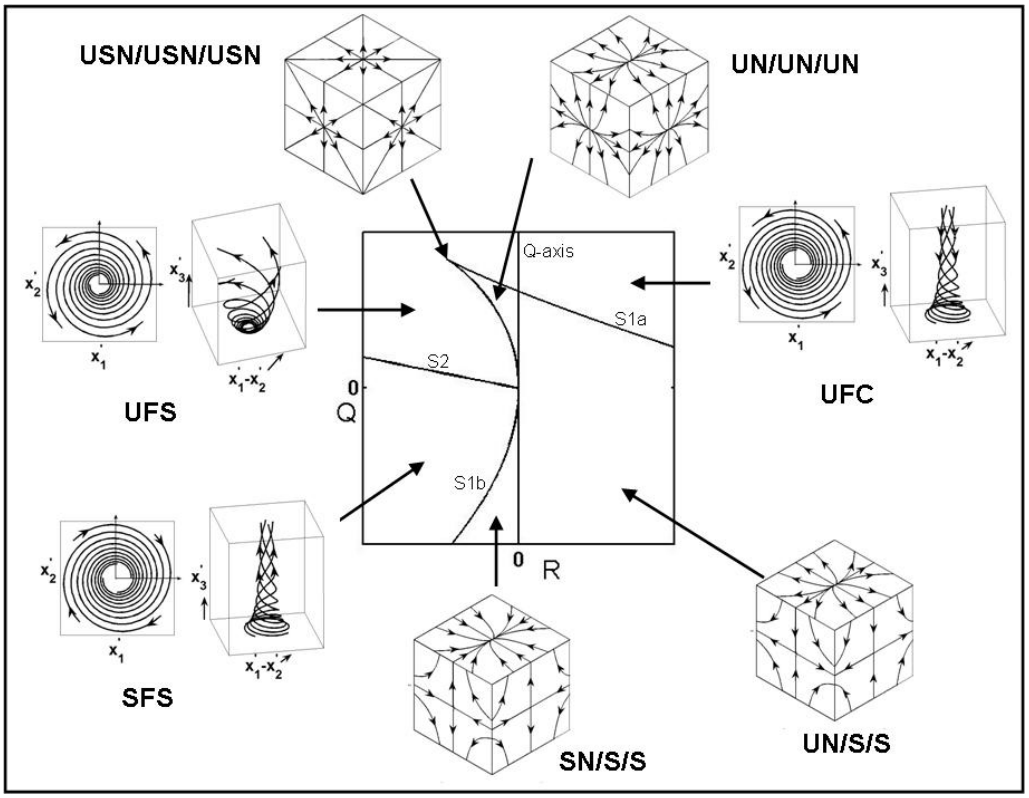

Fig. 2. Regions on a negative p (or a positive A_{ii}) plane and the corresponding flow patterns. Description of acronyms provided in Table I.

The region of complex roots has another dividing surface, S_2, which contains the points associated with purely imaginary roots:

$$PQ - R = 0. \tag{2.6}$$

It is convenient to visualize the $P - Q - R$ space and the various regions (that determine various local flow topologies) by considering planes of Q and R at discrete values of P. On such a plane, surfaces $S1a$, $S1b$ and $S2$ appear simply as curves which divide the plane into different planar regions. In Figures 1 – 3, we show three

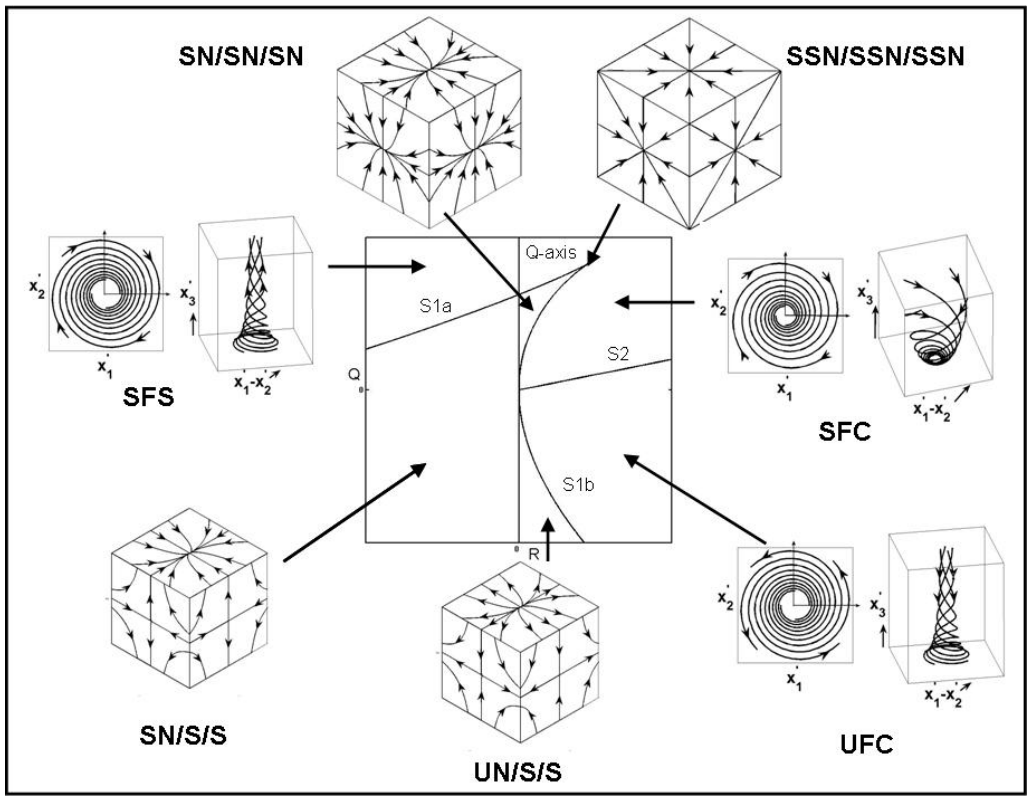

Fig. 3. Regions on a positive p (or a negative A_{ii} plane) and the corresponding flow patterns. Description of acronyms provided in Table I.

representative $Q-R$ planes at $P=0$, $P<0$ and $P>0$. On the $P=0$ plane (Figure 1) the surface $S2$ is coincident with the Q axis. The surfaces $S1a$ and $S1b$ are symmetric with respect to each other about the Q axis thus dividing the plane into four regions. These four regions are associated with four distinct flow patterns which are schematically shown in Figure 1. These flow patterns are UFC, UNSS, SNSS and SFS. The description of these acronyms and the others which appear elsewhere in this chapter are included in Table I. While UNSS and SNSS are non-focal structures (all real eigenvalues), UFC and SFS are structures with a focus and an out-of-plane strain (one real and two complex conjugates roots). As P assumes a non-zero value, two qualitative differences appear on the Q-R plane: (i) surface $S2$ is no longer co-incident with the Q-axis, and (ii) the symmetry of surfaces $S1a$ and $S1b$ is lost (Figures 2 and 3). Consequently, additional regions appear on these planes. Both $P<0$ and $P>0$ planes are now divided into six regions. An increase in the number of regions results in an increase in the number of possible topologies as well. On both $P<0$ and $P>0$ planes, there are three focal and three non-focal topologies. The schematic of these patterns and their correspondence with the six regions are illustrated in Figures 2 and 3. On each of these figures, in addition to the flow patterns associated with the six regions, we include an illustration of the topology associated with the osculation point of $S1a$ and $S1b$ curves. This topology is USN/USN/USN and SSN/SSN/SSN on $P<0$ and $P>0$ planes, respectively. The significance of these two point-associated topologies in compressible turbulence will be discussed in the next section.

Notably, the associated topology for a given A_{ij} tensor does not depend on the magnitude of the tensor. It depends only on the structure of the tensor. We can define a normalized form of the velocity gradient tensor that retains all the information

Table I. Description of acronyms.

Acronyms	Description
SFS	Stable Focus Stretching
UFS	Unstable Focus Stretching
SFC	Stable Focus Compressing
UFC	Unstable Focus Compressing
SN/S/S	Stable Node/Saddle/Saddle
UN/S/S	Unstable Node/Saddle/Saddle
SN/SN/SN	Stable Node/Stable Node/Stable Node
UN/UN/UN	Unstable Node/Unstable Node/Unstable Node
SSN/SSN/SSN	Stable Star Node/Stable Star Node/Stable Star Node
USN/USN/USN	Unstable Star Node/Unstable Star Node/Unstable Star Node

pertaining to the structure of A_{ij}. The normalized form (a_{ij}) is defined as:

$$a_{ij} \equiv \frac{A_{ij}}{\sqrt{A_{mn}A_{mn}}}. \tag{2.7}$$

Thus, the associated topology can as well be inferred by employing the same methodology as described in [11] but to the space of the normalized invariants p, q and r. These normalized invariants are defined as:

$$\begin{aligned} p \equiv -tr[a] &= -s_{ii}; \\ q \equiv \frac{1}{2}\left(p^2 - tr[a^2]\right) &= \frac{1}{2}\left(p^2 - s_{ij}s_{ji} - w_{ij}w_{ji}\right); \\ r \equiv \frac{1}{3}\left(-p^3 + 3pq - tr[a^3]\right) &= \frac{1}{3}\left(-p^3 + 3pq - s_{ij}s_{jk}s_{ki} - 3w_{ij}w_{jk}s_{ki}\right) \end{aligned} \tag{2.8}$$

where s_{ij} and w_{ij} are the normalized strain and rotation rate tensors: $s_{ij} \equiv \frac{a_{ij}+a_{ji}}{2}$ and $w_{ij} \equiv \frac{a_{ij}-a_{ji}}{2}$. The advantage of using normalized invariants is that all the quantities are bounded by their known algebraic limits. In compressible flows, p, which is negative of normalized dilatation, can vary within the algebraic limits of $-\sqrt{3}$ and $\sqrt{3}$. On the other hand the normalized invariants q and r are bounded in the intervals $[-1/2, 1]$ and $\left[-\sqrt{3}/9, \sqrt{3}/9\right]$, respectively.

B. DNS results of invariants and local topology

In this section, we present the statistics of velocity gradient invariants seen in direct numerical simulation of compressible decaying isotropic turbulence. We examine these statistics conditioned upon normalized dilatation ($a_{ii} = \frac{A_{ii}}{\sqrt{A_{mn}A_{mn}}}$). We also examine the dependence of the conditional statistics on initial Mach number and Reynolds number.

All DNS results presented in this section are computed using a Gas Kinetic Method (GKM) solver. GKM solvers have been developed and verified for various

Table II. DNS simulation cases

Parameter	Case A	Case B	Case C
Re_λ	55.6	80.0	55.6
M_t	0.70	0.70	0.43

compressible flow applications [35, 36]. Kerimo et al. [37] demonstrate the accuracy and robustness of GKM solvers for turbulent flow simulations. DNS data used for discussion in this chapter is obtained by Lee [38] over a computational domain of 256^3 box with periodic boundary conditions. We discuss results from three different simulation cases. The initial turbulent Mach number (M_t) and Taylor-scale Reynolds number (Re_λ) of these simulations are specified in Table II. Further details about the simulations are available in [38]. In each case, velocity field is obtained at the peak of dissipation. Velocity gradient field is then computed for the entire computational domain, and subsequently the three invariants are evaluated at each grid point. Using the values of p at these grid points, $q - r$ data is then binned at various chosen levels of normalized dilatation. The bin specifications and the sample size corresponding to each bin are provided in Table III.

1. Conditional invariant statistics in compressible turbulence

We study the statistics of the invariants in terms of (i) joint probability density function (PDF), and (ii) probability of occurrence of various topologies (shown in Figures 1–3) at various levels of normalized dilatations. We start the discussion with the zero dilatation case ($a_{ii} = -p = 0$). Subsequently, we study the invariant statistics conditioned upon different positive and negative dilatation values. All the conditional

Table III. Number of samples at each dilatation level. Bin size corresponding to each dilatation level is ±0.05 about the median value.

Median value of a_{ii}	Case A	Case B	Case C
1.4	657	419	-
1.1	6941	3759	7
0.7	66455	47592	2368
0.3	914684	788133	236518
0.0	3866101	4208919	7108648
-0.3	786840	762275	284889
-0.7	89321	69572	4811
-0.9	31868	22140	1150
-1.4	749	647	10

joint PDFs are obtained by considering bins of dimensions 0.008 X 0.008 on the $q-r$ plane. Unless specified otherwise, all reported results are from Case A simulation.

a. Zero dilatation

In Figure 4a we plot the joint PDF of q and r conditioned upon zero normalized dilatation. The PDF shown in Figure 4a has two prominent features: (i) a significant number of points lie in the upper left area distributed over an elliptical region; and (ii) the bulk of data lies in the lower right area concentrated around the Vieillefosse line ($q = \sqrt[3]{27r^2/4}$). Lee [38] shows that the statistics of strain-rate eigenvalues and vorticity alignment tendencies in compressible turbulence conditioned upon zero dilatation are very similar to the statistics seen in incompressible turbulence. We examine whether such similarity can be seen in terms of invariant statistics as well. In Figure 4b we present the joint PDF of q and r seen in DNS of incompressible decaying turbulence. Clearly the distribution from compressible DNS is very similar to the one from incompressible DNS. The two prominent features mentioned above are indeed the same features that are seen in a variety of incompressible flows ([12]–[22]). Further, we make quantitative comparisons between the conditional data from compressible turbulence and incompressible DNS results in terms of the percentages of various possible topologies. In Table IV we present the percentage occurrence of various possible topologies. Indeed, the probability of occurrence of each topology seen in compressible turbulence is very close to those seen in incompressible turbulence. Based on these observations, we can conclude that in decaying compressible turbulence, at the locations of negligible normalized dilatation, the joint statistics of second and third invariants is very similar to the statistics seen in incompressible turbulence.

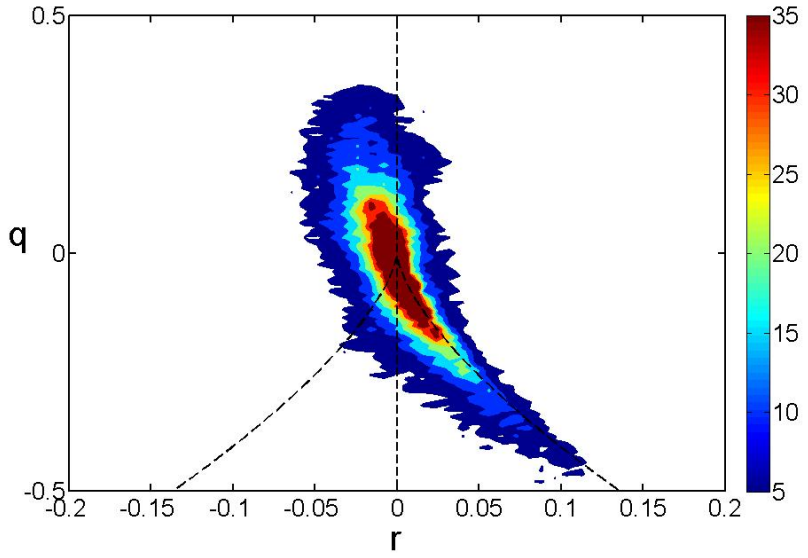

(a)

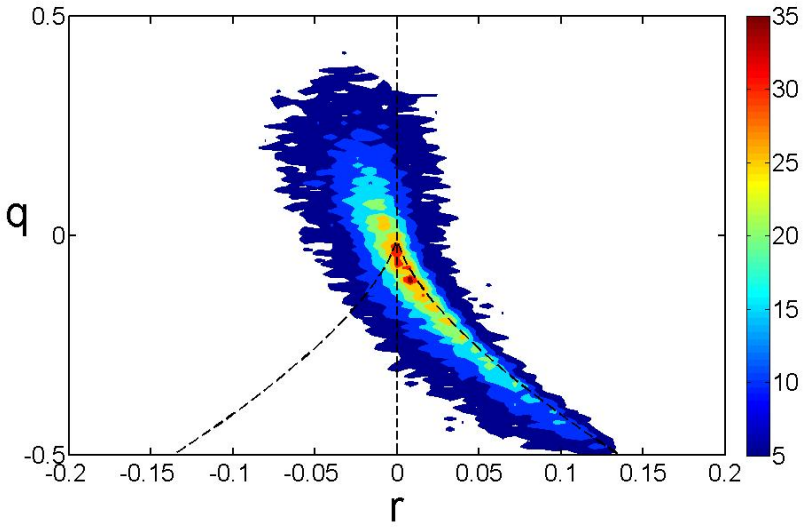

(b)

Fig. 4. (a) Joint PDF of q and r conditioned upon zero dilatation from Case A simulation, and (b) joint PDF of q and r from DNS of incompressible decaying isotropic turbulence.

Table IV. Comparison of percentage of various flow topologies conditioned upon zero dilatation

	UFC	UN/S/S	SN/S/S	SFS
Case A	25.6	24.9	6.5	43.1
Incompressible DNS	27.5	25.4	7.3	39.9

b. Positive dilatation

In Figures 5a, 5c, 5e and 5g, we plot the joint PDFs of q and r conditioned upon various positive values of normalized dilatation. The chosen levels of normalized dilatation vary from 0.3 to 1.4. A visual inspection of these figures suggests that the PDFs are strongly dependent on the value of normalized dilatation. Both the shape and concentration of distribution with respect to the various region-dividing curves ($S1a$, $S1b$, $S2$ and q-axis, see Figure 2) change significantly with changing dilatation level. In fact the shape of the distribution is seen to be following a trend: the shape changes from being elongated tear shaped at zero dilatation to a more localized elliptical shape as dilatation assumes higher positive values. Indeed at the extreme positive dilatation ($a_{ii} = \sqrt{3}$) the distribution is almost a two dimensional Dirac-delta distribution (not shown) with all points being located at the osculation point of $S1a$ and $S1b$. As shown in Figure 2, this point corresponds to a rotation free topology with all the eigenvalues being real, equal and positive. According to the nomenclature of Chong et al. [11] the topology is USN/USN/USN. This topology can also be visualized as rotation-free, isotropic (spherical) expansion of a fluid element. The corresponding eigenvalues are $\left(1/\sqrt{3}, 1/\sqrt{3}, 1/\sqrt{3}\right)$. In fact it can be shown using simple algebra that, at $a_{ii} = \sqrt{3}$, this eigenvalue set is the only possibility. Also, this state

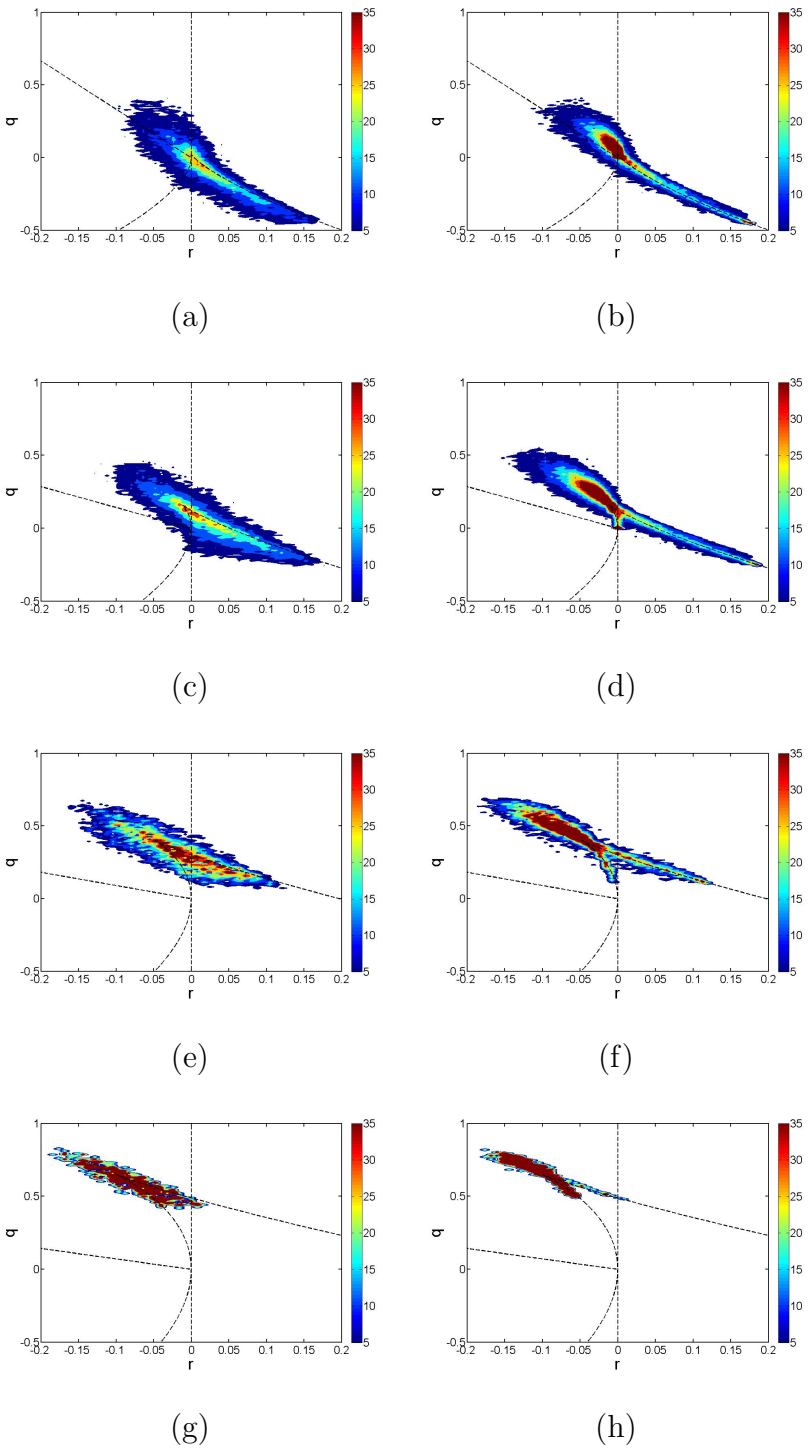

Fig. 5. Conditional joint PDF of q and r as seen in Case A DNS simulation (left column) and HEE model simulation (right column). Value of a_{ii} changes from top to bottom in the following order: 0.3, 0.7, 1.1 and 1.4.

Table V. Percentage of various flow topologies conditioned upon different positive dilatation levels from Case A simulation

a_{ii}	UFC	UN/S/S	SN/S/S	SFS	UFS	UN/UN/UN	USN/USN/USN
0.3	24.4	31.2	3.2	21.2	20.0	0.0	0.0
0.7	22.1	33.7	0.6	5.5	37.2	0.8	0.0
1.1	10.4	25.8	0.0	0.0	53.3	10.5	0.0
1.4	0.0	1.5	0.0	0.0	60.1	38.4	0.0
1.7	0.0	0.0	0.0	0.0	0.0	0.0	100.0

is one of the stable solutions of the pressure-released velocity gradient dynamics [39]. Next we examine the percentage occurrence of each of the possible topologies (see Figure 2) at $a_{ii} > 0$. These percentages are presented in Table V. At low positive dilatations, the percentages of UFC, UNSS and SNSS do not show significant difference as compared to the zero dilatation state. However, the probability of SFS reduces significantly giving way to UFS topology, which is non-existent at zero dilatation. As dilatation level increases further, richness in the topology of compressible flows is severely reduced. At high positive dilatation value of 1.4, the only existing topologies are UN/UN/UN and UFS. Eventually at the extreme dilatation value of $\sqrt{3}$ the only existing topology is USN/USN/USN. As a_{ii} increases, it is plausible to expect a decrease in the strength of rotation-rate (w_{ij}). Since the categorization scheme based on $p-q-r$ phase space does not address this issue directly, we seek a confirmation of this expectation. The contribution of normalized rotation-rate in a_{ij} can be gauged by the following quantity:

$$\phi \equiv \frac{w_{ij}w_{ij}}{w_{mn}w_{mn} + s_{mn}s_{mn}}. \tag{2.9}$$

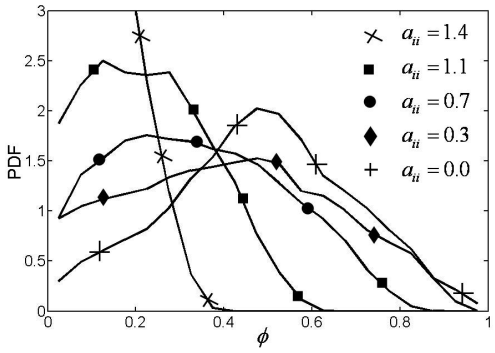

(a)

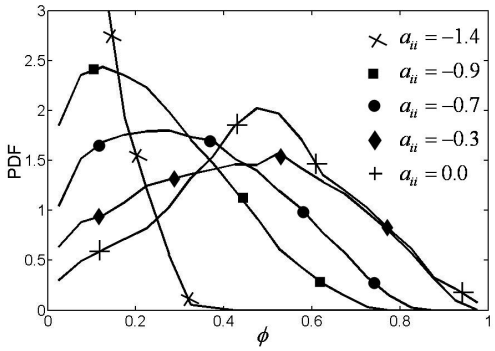

(b)

Fig. 6. Conditional PDFs of $\phi \equiv \frac{w_{ij}w_{ij}}{s_{mn}s_{mn}+w_{mn}w_{mn}}$ at different levels of normalized dilatation from Case A simulation: (a) positive a_{ii}; and (b) negative a_{ii}.

In Figure 6a we present conditional PDFs of ϕ at different levels of normalized dilatation. As a_{ii} increases from zero to $\sqrt{3}$, the PDFs shift leftwards clearly indicating that the rotation-rate is decreasing. Thus, at high positive values of a_{ii} – even though we see considerable focal structures (see Table V)– we can conclude that the contribution of rotation-rate in a_{ij} monotonically reduces.

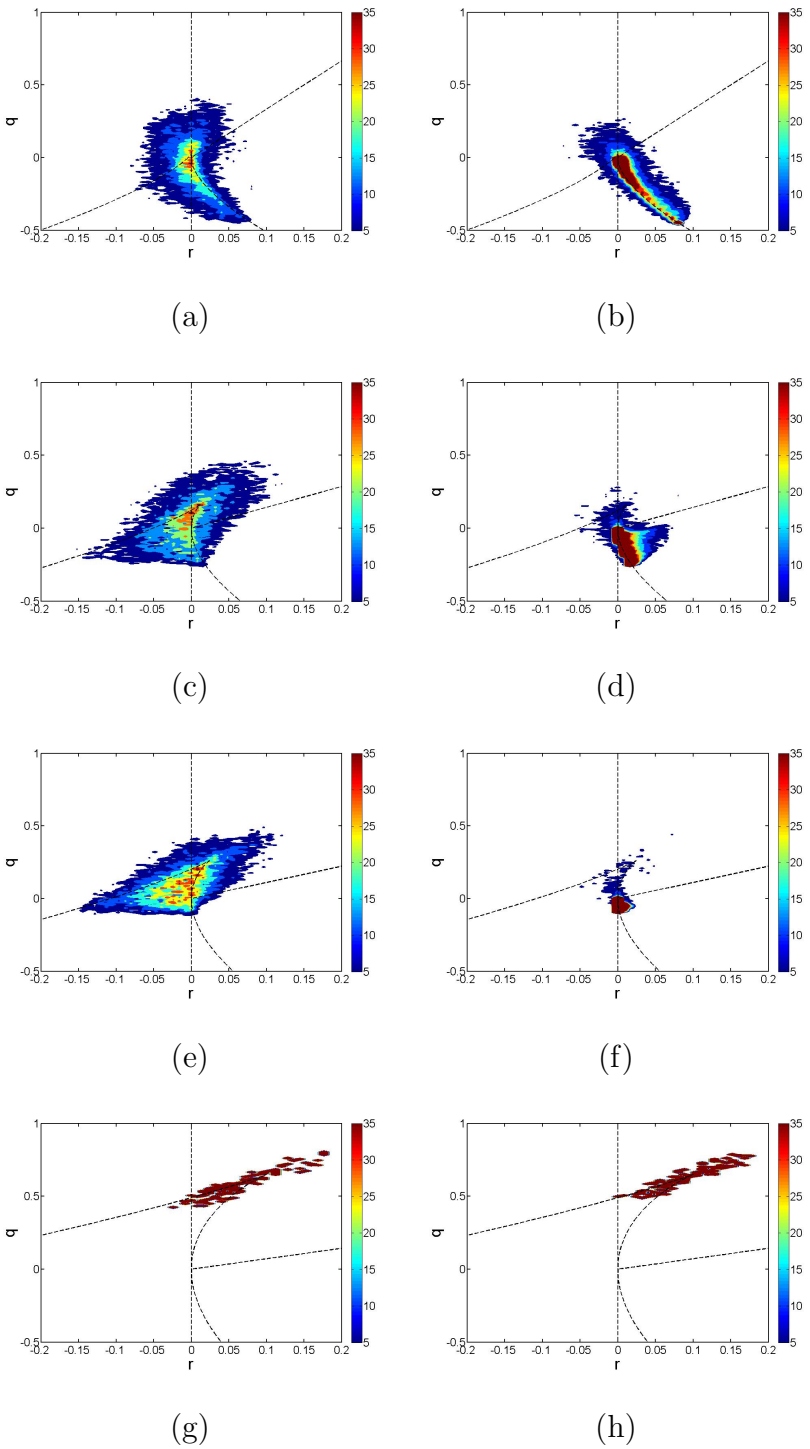

Fig. 7. Conditional joint PDF of q and r as seen in Case A simulation (left column) and HEE model simulation (right column). Value of a_{ii} changes from top to bottom in the following order: -0.3, -0.7, -0.9 and -1.4.

Table VI. Percentage of various flow topologies conditioned upon different negative dilatation levels from Case A simulation

a_{ii}	UFC	UN/S/S	SN/S/S	SFS	SFC	SN/SN/SN	SSN/SSN/SSN
-0.3	22.4	14.6	17.1	30.3	15.4	0.0	0.0
-0.7	11.1	2.7	33.5	21.8	30.1	0.8	0.0
-0.9	2.7	0.2	37.6	18.3	37.9	3.3	0.0
-1.4	0.0	0.0	2.7	0.5	45.4	51.4	0.0
-1.7	0.0	0.0	0.0	0.0	0.0	0.0	100.0

c. Negative dilatation

We present the conditional joint PDFs of q and r at various negative dilatation values in Figures 7a, 7c, 7e and 7g. In these figures, a_{ii} varies from -0.3 to -1.4. The overall variation in shape and location of the joint distributions is similar to what we observed for positive dilatation values: (i) the shape of the distribution changes from being tear shaped at low negative dilatations to an elliptical shape, which keeps shrinking with increasing magnitude of normalized dilatation, (ii) at extreme negative dilatation of $-\sqrt{3}$ all fluid elements get concentrated at the cusp of surfaces $S1a$ and $S1b$. At $a_{ii} = -\sqrt{3}$ all the eigenvalues of the velocity gradient tensor are real, equal and negative and the associated topology is SSN/SSN/SSN. Despite the overall similarity between the trends for positive and negative dilatational values, distributions at negative dilatation show a distinct feature. At moderate/high dilatations (Figures 7c and 7e), there is a distinct higher preference for the points to gather along the $S1b$ curve near the origin. The eigenvalues of a_{ij} associated with the origin on a negative $q - r$ plane are $(0, 0, -1)$ and is suggestive of formation

of shocklets in the flow field. This eigenvalue set is one of the stable solutions of pressure-released velocity gradient dynamics [39].

In Table VI we present the percentage occurrence of various topologies at different negative dilatation levels. Moving from zero to negative dilatations, SFC and SN/SN/SN are the new topologies that emerge. As dilatation assumes higher negative dilatations, the topologies that dominate incompressible turbulence regime disappear. At high negative dilatations, SN/SN/SN and SFC are the predominant flow patterns. At the extreme negative dilatation $a_{ii} = -\sqrt{3}$ the topology is unique (SSN/SSN/SSN) with the three eigenvalues being equal, real and negative $\left(-1/\sqrt{3}, -1/\sqrt{3}, -1/\sqrt{3}\right)$. Again, just like the case for extreme positive dilatation, the uniqueness of this set can easily be demonstrated using simple algebra. However, unlike the state at $a_{ii} = \sqrt{3}$, the unique eigenvalue set at $a_{ii} = -\sqrt{3}$ is not one of the stable solutions of pressure-released velocity gradient dynamics [39]. Also, similar to the observation made at positive dilatation values, we observe that as a_{ii} assumes higher negative values, normalized rotation-rate monotonically decreases from $a_{ii} = 0$ to $a_{ii} = -\sqrt{3}$ (Figure 6b).

Thus we conclude that the joint PDFs of the second and third invariants of normalized velocity gradient tensor are strongly dependent on normalized dilatation value. At zero dilatation the distribution has a tear drop shape and is very similar to the distribution seen in incompressible turbulence. As the dilatation level increases (positive or negative), we see a drastic departure from this shape. The distributions get increasingly more localized on the p-plane with increasing magnitude of normalized dilatation, leading to a reduction in the variety of observed flow patterns. At either extreme of normalized dilatation ($-\sqrt{3}$ and $\sqrt{3}$), the distribution shrinks to the cusp of surfaces $S1a$ and $S1b$ and is associated with a unique topology with all the eigenvalues being real and equal. Moreover, an increase in the magnitude of nor-

malized dilatation is associated with a tendency of monotonic decrease in normalized rotation-rate.

2. Dependence of conditional statistics on Mach and Reynolds number

Lee [38] demonstrates that conditional statistics of strain-rate eigenvalues and vorticity alignment tendencies in compressible turbulence remains largely independent of Reynolds number and Mach number of the flow. In this sub-section, we examine the influence of initial Reynolds number and initial Mach number on the conditional statistics of invariants. We make comparisons between different cases listed in Table II. Case A is compared with Case B to examine the effects of Reynolds number. Case A is compared with Case C to infer the effects of initial Mach number.

Using figures similar to Figures 4–7, we qualitatively examine the conditional joint distributions of the second and third invariants for Cases B and C. In Case C, which has a lower initial Mach number ($M_t = 0.43$), very high positive or very high negative dilatations are rarely seen [38]. In the absence of adequate sample size, statistics for $a_{ii} > 1$ and $a_{ii} < -1$ is not available for this case. Otherwise, various qualitative features of distribution and general trends seen in Cases B and C are very similar to what we observed in Case A. We do not include the joint distribution contours from Cases B and C here, however, we present quantitative comparisons between the three cases in terms of the conditional percentage of various topologies. In Table VII we present the conditional percentages at zero dilatation. In Tables VIII and IX, percentages at positive and negative dilatations are included.

a. Effect of Reynolds number on topology

In Tables VII – IX, we compare Case A and Case B to infer the influence of Reynolds number on the percentage occurrence of flow patterns. At zero and almost all positive

Table VII. Percentage of various flow topologies conditioned upon zero dilatation from different simulation cases. In each cell below, percentages are presented in the following order: (UFC, UN/S/S, SN/S/S, SFS)

	Case A	Case B	Case C
a_{ii}	($Re_\lambda = 55.6$, $M_t = 0.70$)	($Re_\lambda = 80.0$, $M_t = 0.70$)	($Re_\lambda = 55.6$, $M_t = 0.43$)
0	(26, 25, 7, 43)	(25, 26, 7, 42)	(27, 25, 6, 43)

Table VIII. Percentage of various flow topologies conditioned upon different positive dilatation levels from different simulation cases. In each cell below, percentages are presented in the following order: (UFC, UN/S/S, SN/S/S, SFS, UFS, UN/UN/UN)

	Case A	Case B	Case C
a_{ii}	($Re_\lambda = 55.6$, $M_t = 0.70$)	($Re_\lambda = 80.0$, $M_t = 0.70$)	($Re_\lambda = 55.6$, $M_t = 0.43$)
0.3	(24, 31 3, 21, 20, 0)	(23, 33, 4, 22, 17, 0)	(27, 32, 5, 24, 12, 0)
0.7	(22, 34, 1, 6, 37, 1)	(21, 39, 1, 7, 31, 1)	(27, 38, 1, 8, 26, 1)
1.1	(10, 26, 0, 0, 53, 11)	(11, 28, 0, 0, 51, 11)	-
1.4	(0, 2, 0, 0, 60, 38)	(0, 1, 0, 0, 60, 39)	-

Table IX. Percentage of various flow topologies conditioned upon different negative dilatation levels from different simulation cases. In each cell below, percentages are presented in the following order: (UFC, UN/S/S, SN/S/S, SFS, SFC, SN/SN/SN)

	Case A	Case B	Case C
a_{ii}	($Re_\lambda = 55.6$, $M_t = 0.70$)	($Re_\lambda = 80.0$, $M_t = 0.70$)	($Re_\lambda = 55.6$, $M_t = 0.43$)
-0.3	(22, 15, 17, 30, 15, 0)	(22, 15, 20, 28, 15, 0)	(26, 14, 20, 27, 13, 0)
-0.7	(11, 3, 34, 22, 30, 1)	(11, 3, 36, 22, 28, 1)	(10, 2, 36, 20, 31, 1)
-0.9	(3, 0, 38, 18, 38, 3)	(3, 0, 40, 17, 37, 3)	(2, 0, 36, 12, 48, 3)
-1.4	(0, 0, 3, 1, 45, 51)	(0, 0, 0, 0, 57, 43)	-

dilatations the percentage values from Case B simulation are very close to those from Case A simulations except at $a_{ii} = 0.7$. At this dilatation, an increase in Reynolds number increases the probability of UNSS topology. At various negative dilatations in Table IX, the agreement is generally good except at $a_{ii} = -1.4$. While at lower Reynolds number (Case A), UN/UN/UN is the most dominant topology, at higher Reynolds number (Case B), SFC emerges as the most dominant topology. Since the sample size at $a_{ii} = -1.4$ is quite small, this aberration may be a statistical error. Over all, Reynolds number (in the range investigated) appears to have negligible effect on topology conditioned on normalized dilatation.

b. Effect of Mach number on topology

We compare Case A and Case C results in Tables VII–IX to infer the effects of initial Mach number. As mentioned above, Case C simulation does not offer adequate

samples at high positive/negative dilatations. Thus, this comparison is naturally restricted to low and moderate dilatation levels. In Table VII we observe that Mach number has no effect on the topology of the flow field conditioned upon zero dilatation. At non-zero dilatations also, there are no significant differences between the two cases except at $a_{ii} = -0.9$. At this dilatation, the probability of SFC topology is higher than what is seen in Case A. On the basis of these observations, we conclude that turbulent Mach number (in the range investigated) does not appear to influence the conditional topology.

C. HEE model computations of invariants and local topology

Velocity gradient evolution is a highly non-linear process. Understanding this process is of paramount importance, as it holds the key to many turbulent processes of practical interest like mixing, intermittency, cascading, etc. While DNS results do provide an almost time-continuous, domain-spanning data of this evolution, it is often difficult to develop in-depth physical insights with such large volumes of data. For this reason, there has always been a need to have simple Lagrangian dynamical models that can offer an approximate, though a more direct way to probe the evolution of velocity gradients in a flow field. However, such models require adequate validation before they can be employed for wider purposes. Restricted Euler equation is one such model [4] for incompressible velocity gradient dynamics. It has been used with considerable success [28, 6] and being continuously improved [40, 7, 30, 31, 32]. REE, however, is not useful for compressible velocity gradients. To the authors' knowledge, the only available dynamical model for compressible velocity gradient dynamics is the homogenized Euler equation model [26]. The model shows considerable success in predicting strain-rate statistics in compressible turbulence [26]. In this section, we

examine whether the model can capture the various characteristics of compressible velocity gradient invariants discussed in Section C.

We numerically solve the HEE equation employing the same initial conditions as described in [26]. To study the HEE results, we adopt an approach similar to what we employed for analyzing the DNS results in Section C. We condition the HEE solution upon various levels of normalized dilatation and examine the joint statistics of the second and third invariants of the normalized velocity gradient tensor (a_{ij}) at different dilatation levels.

In Figures 5 and 7, we present the conditional joint PDF of q and r obtained from HEE computations. The dilatation level ranges from -1.4 to 1.4. At zero dilatation the HEE model accurately predicts the tear-drop shape of the distribution at zero dilatation (discussed in detail in [26]). As the dilatation level changes, HEE distributions show changes in shape and location with respect to the various partitioning curves (see Figures 1 – 3). The underlying trend of these changes is similar to the DNS behaviour in Figures 5 and 7. As normalized dilatation assumes a higher positive value, the HEE distributions shrink and clearly show the tendency to get concentrated near the cusp of surfaces $S1a$ and $S1b$. On the other hand, at moderate/high negative dilatations, HEE distributions show a pronounced tendency to concentrate near the origin. This is reminiscent of the behaviour observed in DNS at moderate/high negative dilatations (see Figure 7c). However, HEE clearly overestimates this behaviour.

Next we perform a quantitative evaluation of the HEE model. We compare the HEE computations against DNS in terms of the probability of occurrence of various topologies. In Tables X – XII, we present the percentage of various topologies computed from the HEE solution at different levels of dilatation. First we consider the topologies at zero dilatation (Table X). The percentage occurrence of SN/S/S

Table X. Percentage of various flow topologies conditioned upon zero dilatation from HEE computations

UFC	UN/S/S	SN/S/S	SFS
44.3	13.2	4.2	38.2

Table XI. Percentage of various flow topologies conditioned upon different positive dilatation levels from HEE computations

a_{ii}	UFC	UN/S/S	SN/S/S	SFS	UFS	UN/UN/UN	USN/USN/USN
0.3	28.2	17.1	1.8	18.5	32.6	1.8	0.0
0.7	18.4	15.2	0.2	1.9	60.8	3.5	0.0
1.1	13.8	8.3	0.0	0.0	72.4	5.5	0.0
1.4	0.0	0.0	0.0	0.0	78.1	21.9	0.0
1.7	0.0	0.0	0.0	0.0	0.0	0.0	100.0

and SFS predicted by HEE are close to the corresponding percentages seen in Case A DNS simulation (Table IV). The model also correctly predicts UFC and SFS as the most dominant topologies. However, it overestimates the probability of UFC.

In Table XI we present the HEE data at positive dilations. A comparison against corresponding DNS results (Table V), clearly suggests the failure of the HEE model to capture the probabilities accurately. However, the model does capture certain features. HEE correctly predicts UFS as the dominant topology at all moderate/high positive dilatations. At high dilatation ($a_{ii} = 1.4$), the model correctly predicts UN/UN/UN as the second most dominant topology.

Table XII includes the percentage of topologies at various negative dilatations

Table XII. Percentage of various flow topologies conditioned upon differentnegative dilatation levels from HEE computations

a_{ii}	UFC	UN/S/S	SN/S/S	SFS	SFC	SN/SN/SN	SSN/SSN/SSN
-0.3	52.6	10.0	7.5	22.4	7.5	0.0	0.0
-0.7	60.3	7.6	10.2	9.0	12.5	0.3	0.0
-0.9	66.2	6.2	10.1	3.4	13.8	0.3	0.0
-1.4	0.0	0.0	0.0	0.0	77.1	22.9	0.0
-1.7	-	-	-	-	-	-	-

obtained with HEE computations. We compare this table against the DNS data in Table VI. At low negative dilatation ($a_{ii} = -0.3$), HEE correctly predicts UFC as the dominant topology, but clearly overestimates the percentage. At moderate and high dilatation levels, the failure of HEE to estimate the correct percentages is very apparent. However, at high negative dilatation ($a_{ii} = -1.4$), the model correctly identifies SN/SN/SN and SFC as the only existing topologies. At extreme negative dilatation ($a_{ii} = -\sqrt{3}$) HEE does not offer any statistics for comparison.

Based on the foregoing discussion, we conclude that HEE model does not recover the percentage occurrence of various topologies very accurately. However, it captures most of the qualitative trends seen in DNS data. The performance at zero and positive dilatations is, in general, superior to that at negative dilatations. As indicated in [26], inclusion of viscosity and other non-isentropic effects may be required to further improve the HEE model.

D. Conclusions

In this chapter, the dependence of joint statistics of second and third invariants of velocity gradient tensor on dilatation (degree of compression/expansion of a fluid element) in compressible decaying isotropic turbulence is examined using DNS results. Moreover, the exact probabilities of occurrence of various local flow patterns/topologies conditional upon dilatation are computed. The study reveals that the joint statistics of the second and third invariants is highly dependent on normalized dilatation. Invariant statistics conditioned upon zero dilatation is very similar to the behavior seen in incompressible turbulence but changes drastically as dilatation assumes higher positive/negative values. It is found that at high positive and negative dilatations, the dominant topologies are entirely different from those seen in incompressible turbulence. While unstable focus stretching and unstable node/unstable node/unstable node dominate at high positive dilatations, stable focus compressing and stable node/stable node/stable node topologies are dominant at large negative dilatations. As the extreme levels of normalized dilatations are reached ($\pm\sqrt{3}$), the variety in the observed flow patterns is further reduced. The only observed flow pattern at $\sqrt{3}$ and $-\sqrt{3}$ is unstable star node/unstable star node/unstable star node and stable star node/stable star node/stable star node, respectively. Furthermore, it is found that the conditional behavior of invariants is insensitive to Reynolds number and Mach number (at least in the considered range). Additionally in this part of the dissertation, the above-mentioned findings are employed to evaluate the performance of a recently developed velocity gradient model – homogenized Euler equation (HEE). It is found that the HEE model qualitatively captures many features seen in DNS. However, the quantitative performance is not very accurate, especially at negative dilatation values.

CHAPTER III

HOMOGENIZED EULER EQUATION: A MODEL FOR COMPRESSIBLE VELOCITY GRADIENT DYNAMICS*

The principal objective of this chapter is to develop a velocity-gradient model for turbulent compressible flows along the lines of the incompressible restricted Euler equation (REE) model. This model -called the homogenized Euler equation (HEE) – is derived from energy and state equations by invoking uniform velocity-gradient assumption [4]. Furthermore the model is validated by comparing: (i) the asymptotic behaviour against fixed-points of Burgers turbulence [39]; (ii) the incompressible-limit behaviour against incompressible DNS results [5, 12] and (iii) strain-rate statistics at intermediate dilatations against compressible DNS results [38]. Comparisons are also made with the asymptotic REE results to highlight the improvements achieved by the HEE model in the incompressible limit.

This chapter is organized as follows. In Section B the homogenized Euler equation (HEE) is developed. Section C contains a discussion of the numerical method and establishes the various velocity-gradient statistics of interest. In Section D the model results are presented, and the performance of the model is evaluated against known turbulence behaviour.

A. Homogenized Euler equation

In this section we develop the homogenized Euler equation and highlight the involved assumptions. For an inviscid calorically perfect gas without any heat source, the

*Reprinted with permission from "Homogenized Euler equation: A model for compressible velocity gradient dynamics" by S. Suman and S. S. Girimaji, 2009, *Journal of Fluid Mechanics*, 620, 177–194, Copyright[2009] by Cambridge University Press.

conservation of mass, momentum and energy equations are:

$$\frac{\partial \rho}{\partial t} + \frac{\partial (\rho V_k)}{\partial x_k} = 0, \tag{3.1}$$

$$\frac{\partial V_i}{\partial t} + V_k \frac{\partial V_i}{\partial x_k} = -\frac{1}{\rho}\frac{\partial p}{\partial x_i}, \tag{3.2}$$

$$\frac{\partial T}{\partial t} + V_k \frac{\partial T}{\partial x_k} = -T(n-1)\frac{\partial V_i}{\partial x_i}, \tag{3.3}$$

where n is the ratio of specific heats; V_i, p, ρ and T represent velocity, pressure, density and temperature. For a perfect gas the three thermodynamic variables are related through the following state equation:

$$p = \rho R T. \tag{3.4}$$

Any attempt to formulate a velocity-gradient model for a general perfect gas flow field would lead to a very high degree of complexity. As a first step we restrict our consideration to a flow field which has a uniform entropy distribution. With this assumption the state equation (3.4) simplifies to the following form:

$$p = C\rho^n, \tag{3.5}$$

where C is constant both in time and space. This assumption significantly simplifies the formulation and yet captures the influence of a thermodynamically evolving pressure field on velocity gradient dynamics. In later works we will ease the uniform entropy assumption to develop models for more complex flows. Nonetheless, we will compare the model performance against decaying non-isentropic turbulence data to investigate the practical utility of the new model. We will also compare the model against Burgers turbulence which represents an extreme limit of compressible flow.

1. Equation for the velocity gradients

We now derive the evolution equation for the primary quantity of interest, the velocity gradient tensor, A_{ij}:

$$A_{ij} \equiv \frac{\partial V_i}{\partial x_j}. \tag{3.6}$$

Equation (3.2) is re-written using (3.5) as

$$\frac{\partial V_i}{\partial t} + V_k \frac{\partial V_i}{\partial x_k} = -\frac{1}{\rho}\frac{\partial (C\rho^n)}{\partial x_i}. \tag{3.7}$$

Taking gradient of this equation leads to an equation for A_{ij}:

$$\frac{\mathrm{d}A_{ij}}{\mathrm{d}t} = -A_{ik}A_{kj} - \frac{\partial}{\partial x_j}\left(\frac{1}{\rho}\frac{\partial (C\rho^n)}{\partial x_i}\right), \tag{3.8}$$

where $\mathrm{d}/\mathrm{d}t$ indicates material derivative. Now, with C and n being constants the pressure Hessian, $\frac{\partial}{\partial x_j}\left(\frac{1}{\rho}\frac{\partial (C\rho^n)}{\partial x_i}\right)$, simplifies to a symmetric form:

$$\frac{\mathrm{d}A_{ij}}{\mathrm{d}t} = -A_{ik}A_{kj} - \frac{Cn}{n-1}\frac{\partial^2 g}{\partial x_i \partial x_j}, \tag{3.9}$$

where $g \equiv \rho^{n-1}$. Closure equation for this symmetric pressure Hessian is next obtained from the mass conservation equation (3.1):

$$\frac{\mathrm{d}}{\mathrm{d}t}\left(\frac{\partial g}{\partial x_i}\right) = -A_{ki}\frac{\partial g}{\partial x_k} - (n-1)\,A_{kk}\frac{\partial g}{\partial x_i} - (n-1)\,g\frac{\partial A_{kk}}{\partial x_i}, \tag{3.10}$$

$$\begin{aligned}\frac{\mathrm{d}}{\mathrm{d}t}\left(\frac{\partial^2 g}{\partial x_i \partial x_j}\right) &= -A_{kj}\tfrac{\partial^2 g}{\partial x_i \partial x_k} - A_{ki}\tfrac{\partial^2 g}{\partial x_k \partial x_j} - \tfrac{\partial A_{ki}}{\partial x_j}\tfrac{\partial g}{\partial x_k} - (n-1)\,A_{kk}\tfrac{\partial^2 g}{\partial x_i \partial x_j} \\ &\quad - (n-1)\,\tfrac{\partial A_{kk}}{\partial x_i}\tfrac{\partial g}{\partial x_j} - (n-1)\,\tfrac{\partial A_{kk}}{\partial x_j}\tfrac{\partial g}{\partial x_i} - (n-1)\,\tfrac{\partial^2 A_{kk}}{\partial x_i \partial x_j} g.\end{aligned} \tag{3.11}$$

2. Central assumption of HEE

As discussed in Chapter I, it is our objective to construct a simple autonomous dynamical system of equations which can capture the essential features of nonlinear velocity

gradient dynamics in compressible turbulence. The success of REE for incompressible flows clearly demonstrates that much insight can be obtained in homogeneous systems wherein the velocity gradients are constant in space [4]:

$$\frac{\partial A_{ij}}{\partial x_k} \equiv 0. \tag{3.12}$$

This is the central assumption of our model. Subject to this assumption, (3.9) and (3.11) simplify substantially to:

$$\frac{\mathrm{d}A_{ij}}{\mathrm{d}t} = -A_{ik}A_{kj} - P_{ij}, \tag{3.13}$$

$$\frac{\mathrm{d}P_{ij}}{\mathrm{d}t} = -P_{ik}A_{kj} - P_{kj}A_{ki} - (n-1)\,P_{ij}A_{kk}, \tag{3.14}$$

where

$$P_{ij} \equiv \frac{Cn}{n-1}\frac{\partial^2 g}{\partial x_i \partial x_j} \tag{3.15}$$

is the pressure Hessian tensor. Equations (3.13) and (3.14) form a closed set of 15 ordinary differential equations in 15 unknowns. We refer to this equation set as the homogenized Euler equation model. It is important here to point out major differences between the HEE and REE formulations. The original REE invokes a more serious assumption in which the pressure Hessian is simplified to only its isotropic component:

$$\frac{\partial}{\partial x_j}\left(\frac{1}{\rho}\frac{\partial p}{\partial x_i}\right) = \frac{1}{\rho}\frac{\partial^2 p}{\partial x_i \partial x_j} = -\frac{A_{mn}A_{nm}}{3}\delta_{ij}. \tag{3.16}$$

This assumption is invoked for the mathematical benefit of yielding a closed set of equations. It must be pointed out that the term 'homogenized' in HEE does not indicate any homogenization procedure. Here, homogeneous refers to the fact that the velocity gradients are (nearly) invariant in space. Homogenization procedure on the other hand refers to the mathematical limit of setting the heterogeneity scale to infinity, thus rendering the problem homogeneous.

Some attempts have been made in literature to include anisotropic contributions [29, 32] in REE. These involve other assumptions which have their own limitations. The HEE, on the other hand, does not require any further assumptions regarding the pressure Hessian. The full Hessian in its natural form is included in the model. This is possible due to the invocation of state and energy equations, which are not used in the REE.

3. Velocity gradient dynamics in Burgers turbulence

In the context of nonlinear turbulence processes, it is relevant to mention the significance of Burgers equation. Burgers turbulence represents the extreme state of compressible turbulence in which pressure effects are negligible in comparison with the inertial effects. For this reason Burgers turbulence is also called the pressure-released turbulence. Burgers turbulence is known [41] to provide a reasonably accurate representation of very high Mach number Navier–Stokes turbulence in (i) high density flows with polytropic index less than unity and (ii) low density flows with polytropic index larger than unity. Due to its simplicity, Burgers equation is often used as a test bed to evaluate new turbulence theories [42, 43]. Burgers turbulence also captures some important aspects of the energy cascade mechanism and intermittency seen in Navier–Stokes turbulence. Girimaji et al. [44] demonstrate that the spectral energy transfer and the triadic interactions displayed by Burgers equation are similar to that in Navier–Stokes turbulence. Recently, Bikkani et al. [39] investigated the dynamics of three dimensional Burgers equation to probe the role of pressure in incompressible flows. One key result in [39] is that Burgers-turbulence velocity gradients exhibit two stable fixed-point families given by:

$$(\alpha, \beta, \gamma, \omega_\alpha, \omega_\beta, \omega_\gamma) = \left(\varphi, 0, \varphi - 1, 0, \pm 2\sqrt{\varphi - \varphi^2}, 0\right); \tag{3.17}$$

$$(\alpha, \beta, \gamma, \omega_\alpha, \omega_\beta, \omega_\gamma) = \left(\tfrac{1}{\sqrt{3}}, \tfrac{1}{\sqrt{3}}, \tfrac{1}{\sqrt{3}}, 0, 0, 0\right), \tag{3.18}$$

where ω_α, ω_β and ω_γ are the components of vorticity along the eigenvectors corresponding to the strain-rates eigenvalues: α; β; and γ. The term φ is a free parameter which depends on initial conditions only. It is reasonable to conclude that these fixed-points represent the turbulent velocity-gradient behaviour in the limit of very large Mach number.

B. HEE normalization and conditional statistics

Inviscid incompressible velocity gradient dynamics exhibit finite-time singularity [28, 7] rendering numerical computations difficult. In this section, we first present the normalized version of HEE which circumvents the finite-time singularity problem by rescaling time. Then we proceed to describe the manner in which statistics are gathered and present the rationale for conditional averaging based on dilatational level.

1. Normalization and rescaling

We define the normalized velocity gradient tensor as:

$$a_{ij} \equiv \frac{A_{ij}}{\epsilon} \quad \epsilon \equiv \sqrt{A_{mn}A_{mn}}. \tag{3.19}$$

The quantity a_{ij} contains all the geometrical information about the velocity gradient tensor and has the advantage of being bounded ($-1 \leq a_{ij} \leq 1$). The substitution of a_{ij} in (3.13), however, results in the appearance of ϵ, which itself can diverge in finite time. To eliminate ϵ from the equations the evolution is considered in rescaled time, t', such that $dt' \equiv dt/\tau$, where $\tau \equiv 1/\epsilon$. With these change of variables, (3.13) and

(3.14) take the following form:

$$\frac{\mathrm{d}a_{ij}}{\mathrm{d}t'} = a_{ij}a_{mn}a_{kn}a_{mk} + \tau^2 a_{ij}a_{mn}P_{mn} - a_{ik}a_{kj} - \tau^2 P_{ij}; \tag{3.20}$$

$$\frac{\mathrm{d}\tau}{\mathrm{d}t'} = \tau a_{mn}a_{kn}a_{mk} + \tau^3 a_{mn}P_{mn}; \tag{3.21}$$

$$\frac{\mathrm{d}P_{ij}}{\mathrm{d}t'} = -P_{ik}a_{kj} - P_{kj}a_{ki} - (n-1)\,P_{ij}a_{kk}. \tag{3.22}$$

This set has the same number of equations as the un-normalized form. The equations are computationally well-behaved even if the un-normalized velocity gradients diverge in finite time. The normalized equations (3.20)–(3.22) are now employed to examine velocity-gradient geometry. As in [7], time integration of (3.20)–(3.22) is performed using fourth-order Runge–Kutta scheme with a specified set of initial conditions for each realization or particle. A particle is "created" by assigning randomly generated values for initial A_{ij}. A random number generator that produces uniformly distributed numbers between -1 and 1 is employed for the purpose. Initial τ is set to unity for all particles. The initial P_{ij} is chosen as in the REE model:

$$P_{ij(t=0)} = -\frac{A_{mn}A_{nm}}{3}\delta_{ij}. \tag{3.23}$$

Starting from this initial condition, P_{ij} then evolves according to (3.22).

2. On the nature of HEE

The HEE, REE and Burgers velocity-gradient models are all autonomous dynamical equation sets with one or more stable fixed-point families. The evolution and asymptotic behaviour of the REE velocity gradients are described in detail in [28]. The incompressibility constraint makes REE transient behaviour analytically tractable. The transient behaviour of Burgers and the HEE model do not appear to be as easily amenable to analytical examination. As mentioned earlier, the asymptotic behaviour

of Burgers velocity gradient dynamics is given in [39]. Our computations show (more on this in next section) that HEE, like Burgers, yields two distinct velocity gradient stable fixed-points. Starting from specified initial conditions, a typical solution trajectory evolves rapidly with non-monotonic changes in dilatation and approaches one of two fixed-points at long times. While the asymptotic geometry of the velocity gradient tensor is important, the transient dynamics also yields crucial insight into turbulence processes. We characterize the transient dynamics conditioned upon the current value of normalized dilatation. Normalized dilatation quantifies the degree of compression of a fluid element, as it represents the rate of change of density. Velocity-gradient statistics conditioned on dilatation provides a basis for comparison of HEE against DNS data.

To minimize the influence of initial conditions, statistics are gathered after an initial time lapse, T:

$$T = \frac{1}{(\tau a_{mn} a_{kn} a_{mk} + \tau^3 a_{mn} P_{mn})_{t'=0}}. \tag{3.24}$$

From (3.24), T can be seen as one velocity gradient turn-over time.

3. Conditional statistics

We perform HEE calculations with an ensemble of fluid particles in order to obtain statistics of various quantities of interest. The normalized velocity gradient tensor (a_{ij}) is separated into its symmetric and anti-symmetric parts: the strain-rate tensor (s_{ij}) and the rotation-rate tensor (w_{ij}). The symbols α, β and γ are assigned to the three eigenvalues of s_{ij} such that $\alpha \geq \beta \geq \gamma$. The sum of these eigenvalues is the dilatation (a_{ii}) or the measure of the rate of change in element volume. In compressible flows, the normalized dilatation, a_{ii}, can vary within the algebraic limits of $-\sqrt{3}$ to $\sqrt{3}$. Expanding fluid elements are characterized by positive dilatation

values whereas contracting ones by negative dilatation values. Ratios between the strain-rate eigenvalues help in visualizing the change in shape of the fluid element. Each of the eigenvalues is normalized as follows:

$$\alpha^* = \frac{\alpha}{\sqrt{\alpha^2+\beta^2+\gamma^2}} \quad \beta^* = \frac{\beta}{\sqrt{\alpha^2+\beta^2+\gamma^2}} \quad \gamma^* = \frac{\gamma}{\sqrt{\alpha^2+\beta^2+\gamma^2}}. \tag{3.25}$$

Another point of interest is the orientation of the vorticity vector, ω. This is examined in terms of the cosine of the angles that the vorticity vector makes with the eigenvectors of (i) the strain-rate tensor and (ii) the pressure Hessian tensor, P_{ij} . Eigenvalues of the pressure Hessian tensor are represented by the symbols α_p, β_p and γ_p such that $|\alpha_p| \geq |\beta_p| \geq |\gamma_p|$ [45]. We also examine the three invariants of the normalized velocity gradient tensor, a_{ij}. The definitions of these invariants are [11]:

$$\begin{aligned} p &\equiv -a_{ii}; \\ q &\equiv \tfrac{1}{2}\left(p^2 - s_{ij}s_{ji} - w_{ij}w_{ji}\right); \\ r &\equiv \tfrac{1}{3}\left(-p^3 + 3pq - s_{ij}s_{jk}s_{ki} - 3w_{ij}w_{jk}s_{ki}\right). \end{aligned} \tag{3.26}$$

C. Results and discussion

In this section we compare the performance of the HEE model against some established analytical and numerical results. We first examine the asymptotic states of the HEE equation and discuss their relation to the stable fixed-points of Burgers velocity gradient dynamics. Next we compare the performance of the HEE in the incompressible limit against incompressible turbulence DNS. Here we also make comparisons with REE results. Finally we compare HEE against compressible DNS results at various intermediate levels of dilatation.

1. Asymptotic behaviour of HEE

As mentioned earlier, the numerical integration of the HEE equations reveal two asymptotic states for the normalized velocity gradient tensor. The normalized dilatations of the two fixed-points are approximately 1.7 and -1. All particles going to the fixed-point with the normalized dilatation value of 1.7 have a vorticity-free three-dimensional isotropic expansion-wave structure:

$$(\alpha, \beta, \gamma, \omega_\alpha, \omega_\beta, \omega_\gamma) \approx \left(\tfrac{1}{\sqrt{3}}, \tfrac{1}{\sqrt{3}}, \tfrac{1}{\sqrt{3}}, 0, 0, 0\right). \tag{3.27}$$

For all the particles in this asymptotic state we observe that the inertial term is much larger than the pressure term: $\|A_{ik}A_{kj}\| >> \|P_{ij}\|$ referring to (3.13). Clearly, this is a pressure-released limit of the HEE. It is then reasonable to compare this solution to the pressure-released Navier–Stokes (Burgers turbulence) fixed-point behaviour given in (3.17) and (3.18). This HEE pressure-released fixed-point is identical to (3.18).

All particles reaching the other asymptotic state ($a_{ii} = -1$) have an one-dimensional compression wave-like structure with negligible vorticity:

$$(\alpha, \beta, \gamma, \omega_\alpha, \omega_\beta, \omega_\gamma) \approx (0, 0, -1, 0, 0, 0). \tag{3.28}$$

This solution happens to be a special case of the first fixed-point (3.17) of Burgers dynamics with parameter φ =0. Despite this agreement, we do not classify this HEE asymptotic state as a pressure-released behaviour. Our computations show that in this asymptotic state the inertia terms are not convincingly large enough as compared to the pressure terms ($\|A_{ik}A_{kj}\| \approx 5\,\|P_{ij}\|$).

Overall, it can be concluded that in the pressure-released or high-Mach number limit, the HEE reproduces asymptotic Burgers turbulence behviour.

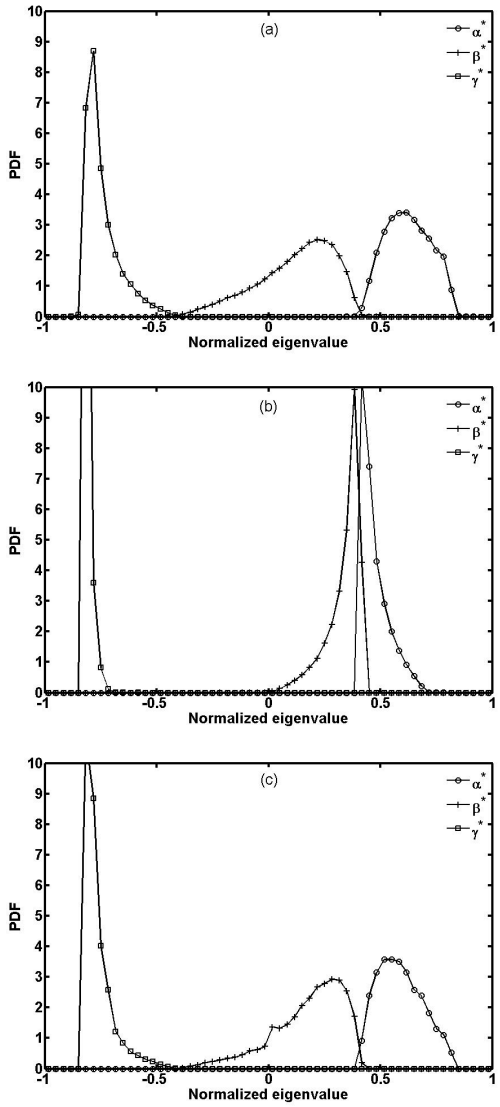

Fig. 8. Probability density functions (PDF) of normalized strain-rate eigenvalues (α^*, β^*, γ^*). (a) Incompressible DNS, (b) asymptotic REE and (c) zero-dilatation HEE.

2. HEE in incompressible limit

Now we will examine HEE at the other limiting case, incompressible turbulence. The HEE results conditioned upon zero dilatation can be interpreted as the incompressible-limit behaviour of the HEE model. We compare this behaviour against DNS results of incompressible decaying isotropic turbulence [37]. We also include the asymptotic REE results in this discussion to highlight the relative improvements achieved with the HEE model in predicting incompressible turbulence behavior.

Alignment of vorticity vector with respect to the eigenvectors of the strain-rate tensor is of much physical significance as it quantifies the extent of vortex stretching in turbulent flows. The information about the sign and magnitude of strain-rate eigenvalues helps us understand cascading due to self straining. In Figures 8 and 9 we present probability density functions of the normalized strain-rate eigenvalues (α^*, β^*, γ^*) and the cosine of the angles vorticity makes with the corresponding eigenvectors. While the probability density functions completely describe the distributions of the quantities of interest, the peaks can be interpreted as the most probable values. The success of asymptotic REE has been limited to qualitatively predicting the following two most-probable features of incompressible turbulence: (i) the intermediate eigenvalue is small but positive, and (ii) vorticity aligns best with the eigenvector corresponding to the intermediate eigenvalue. The REE probability density functions do not recover the broad distributions seen in DNS. The HEE model, on the other hand, not only reproduces the most probable values seen in DNS, but recovers the entire range of distributions in Figures 8 and 9.

Next, we compare joint distribution of the second and third invariants of a_{ij} (3.26). The associated topology of the velocity gradient tensor can be inferred with knowledge of the coordinates (q, r) on the $p = 0$ plane for incompressible flows [11].

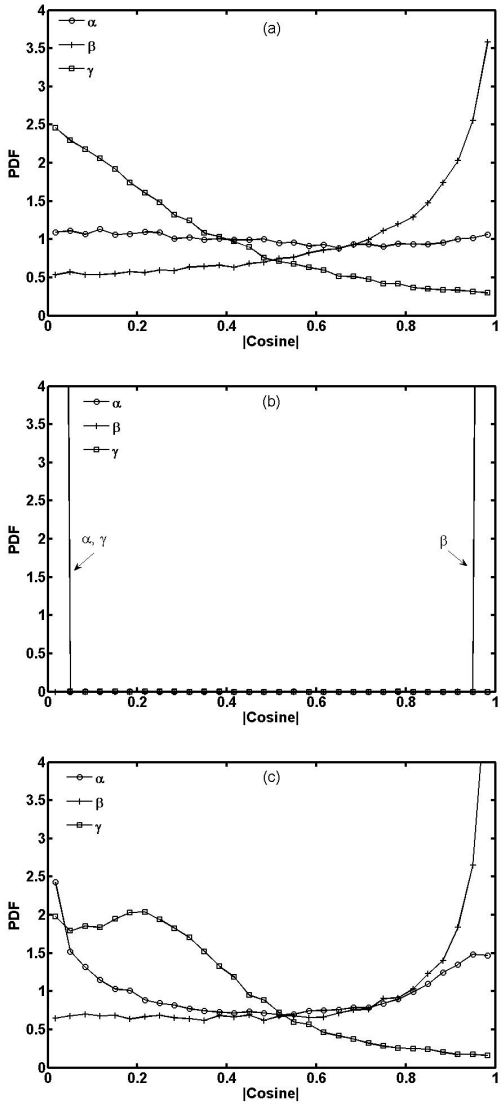

Fig. 9. Probability density functions of the cosines (magnitude) of the angles between vorticity and strain-rate eigenvectors. (a) Incompressible DNS, (b) asymptotic REE and (c) zero-dilatation HEE.

Chen et al. [22] and Soria et al. [12] investigate the dominant local topologies at the dissipating scales of motion in mixing layers in terms of the invariants. Soria et al. [12] plot joint number density of un-normalized invariants rather than joint probability density function. The joint probability density function of q and r computed from isotropic decay DNS data (Figure 10a) has two prominent features: (i) a significant amount of data lies in the lower-right quadrant concentrated along the curve $q = -\sqrt[3]{27r^2/4}$ (Vieillefosse line), and (ii) the bulk of data lies almost uniformly distributed over a roughly elliptical region in the upper-left quadrant. These features have been observed in DNS of a variety of flows and are fairly independent of initial conditions ([12]–[22]). The local topologies corresponding to the distributions in the upper-left and the lower-right quadrants are stable-focus-stretching and unstable-node-saddle-saddle. While the asymptotic REE does capture the first feature seen in DNS, it completely fails to recover the second. The asymptotic REE joint probability density function is completely concentrated on the curve $q = -\sqrt[3]{27r^2/4}$ (Figure 10b). Failure to show any topology in the upper-left quadrant has been one of the major shortcomings of the REE model, and it has attracted considerable research attention [29, 32]. The HEE model on the other hand convincingly recovers both the aforementioned features of the $q - r$ distribution seen in DNS (see Figure 10c). Evidently, the HEE results conditioned on zero dilatation capture the richness of topology observed in incompressible flows much better than the asymptotic REE results.

It is reasonable to attribute the observed superiority of HEE over REE to the inclusion of anisotropic portion of the pressure Hessian tensor. We can further validate the HEE model by examining how vorticity is oriented with respect to the eigenvectors of the pressure Hessian tensor. Eulerian analysis of incompressible flows [45] suggests that at points of maximum enstrophy, vorticity aligns with the eigenvector

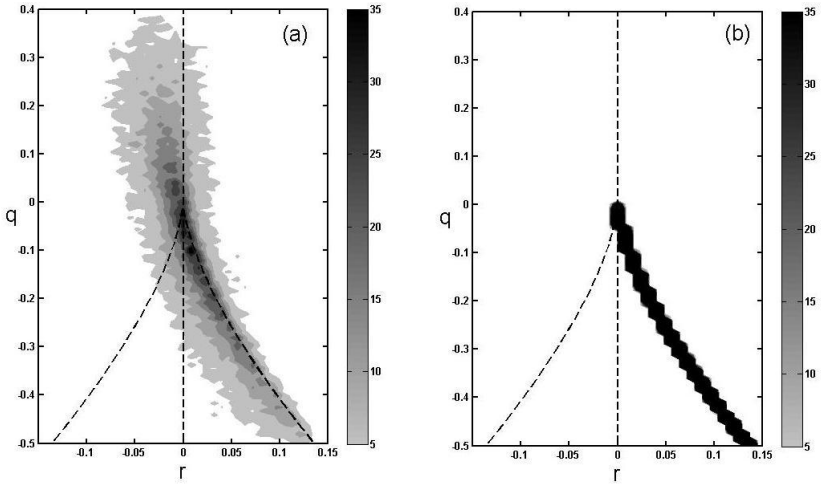

(a) (b)

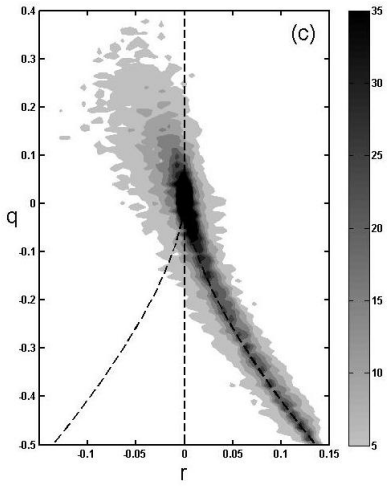

(c)

Fig. 10. Joint probability density function of the second and third invariants (q, r). (a) Incompressible DNS, (b) asymptotic REE and (c) zero-dilatation HEE.

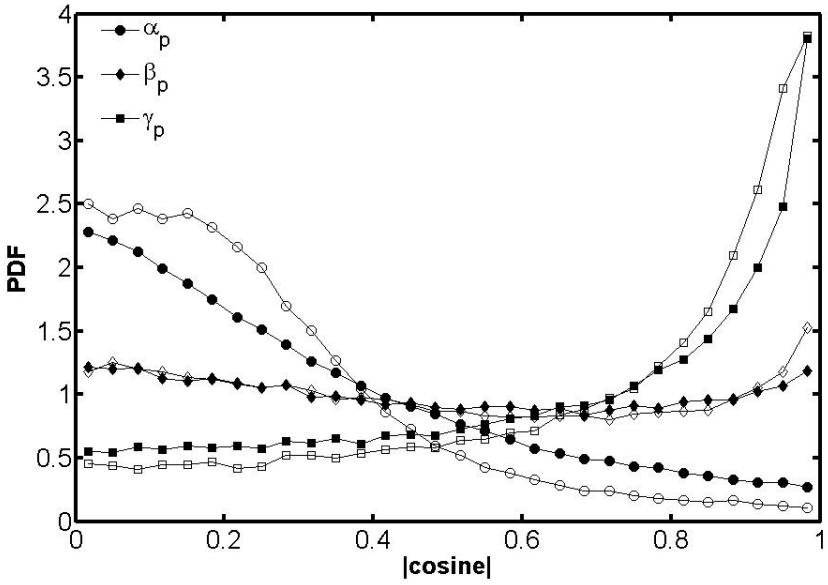

Fig. 11. Probability density functions of the cosines (magnitude) of the angles between vorticity and pressure Hessian eigenvectors. Closed symbols: incompressible DNS. Open symbols: zero-dilatation HEE.

of the pressure Hessian tensor associated with the smallest eigenvalue magnitude. Based on this insight we categorize the pressure Hessian eigenvalues as α_p, β_p and γ_p such that $|\alpha_p| \geq |\beta_p| \geq |\gamma_p|$. This basis of categorization is different from the one followed by Kalelkar [46], wherein the pressure Hessian eigenvalues are categorized by arranging them simply in descending order of value. In Figure 11 we plot the probability density functions of the cosine of the angles between vorticity and pressure Hessian eigenvectors. Similar to what has been observed by Ohkitani et al. [45] in inviscid flows, the DNS also shows a distinct preference of vorticity to align with the eigenvector of γ_p - the eigenvalue with the smallest magnitude. The HEE model accurately recovers not only this trend but the entire distributions seen in DNS. It should be noted that the REE model has an isotropic pressure Hessian tensor and hence does not lend itself to this important examination.

Based on the foregoing discussion we summarize that the HEE model in its incompressible limit accurately recovers the incompressible turbulence behaviour seen in DNS. Moreover, with a more accurate description of the pressure Hessian tensor, the HEE model shows significant improvements over the REE model.

3. HEE at intermediate dilatations

Having established that the HEE model captures the turbulence behaviour reasonably well in the extreme Mach number limits, we now examine its validity at intermediate levels of dilatation. The model results will now be compared against decaying compressible isotropic turbulence DNS data. Although the model development invokes the isentropic assumption, we would like to compare it against general non-isentropic turbulence. Therefore, the decaying turbulence initial conditions are as given in [38] rather than [47], which is expressly for isentropic turbulence. As is standard procedure in REE literature, we compare DNS data against HEE results obtained from statistically un-biased randomly-generated velocity gradient initial conditions. As the HEE equations constitute a non-linear dynamical system, the asymptotic velocity gradient structure will be independent of the initial condition. We do expect the levels of dilatational kinetic energy and dilatational dissipation to depend on initial conditions and initial turbulent Mach number [48, 38]. However, the velocity gradient structure conditioned on local dilatation is expected to be weakly dependent on initial conditions and turbulent Mach number [38]. To ensure that initial conditions do not unduly influence the model-data comparison, the HEE statistics are gathered only after finite time-elapse corresponding to several turn-over times. We would like to point out at the very outset that this comparison between non-isentropic DNS and HEE results from randomly generated initial conditions constitute a very rigorous test of the proposed model.

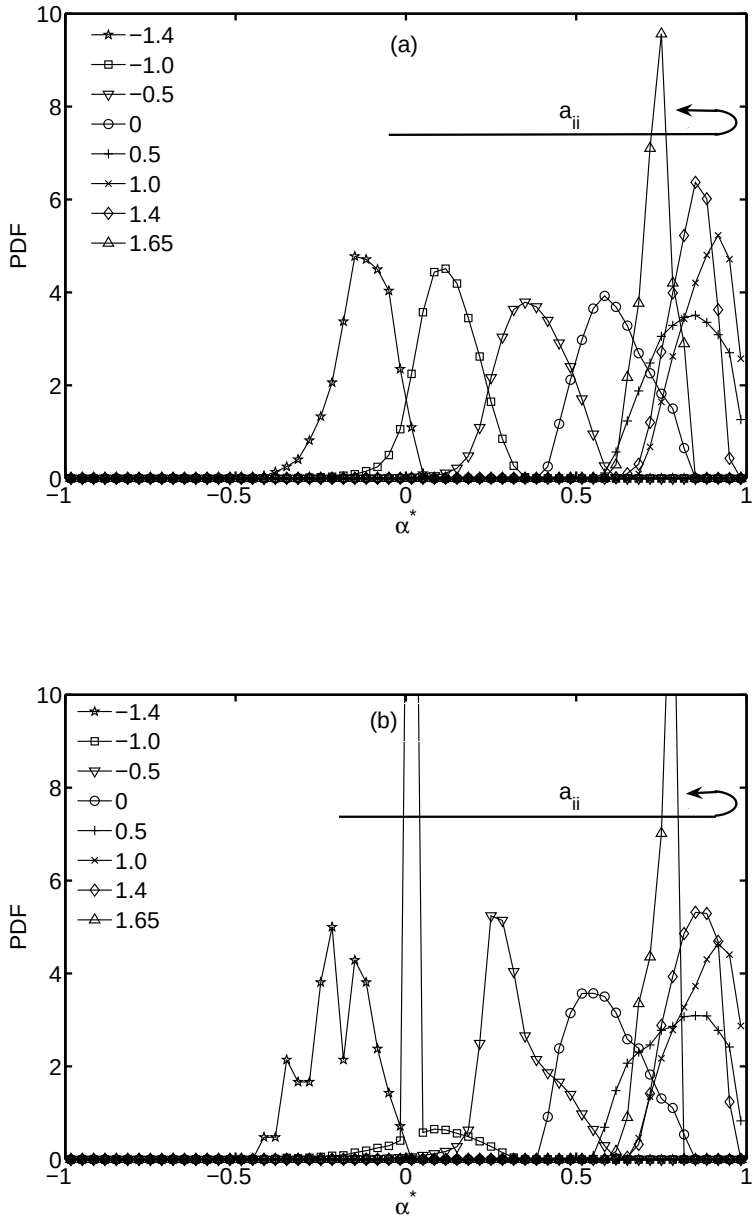

Fig. 12. Probability density functions of normalized largest strain-rate eigenvalue (α^*) conditioned on various values of a_{ii} . (a) Compressible DNS (b) HEE.

As in REE, in HEE velocity gradient tensor is computed following a fluid particle. In addition, in HEE, pressure Hessian is also computed explicitly from an evolution equation. Both in REE and HEE the velocity field is not considered and hence the kinetic energy evolution cannot be computed. Since REE and HEE are inviscid models, dissipation is also not known. Hence DNS and HEE comparison is restricted to velocity gradient alignment angles and invariant maps [4, 5, 28, 29].

The HEE computations of the probability density functions of the strain-rate eigenvalues are compared against decaying compressible turbulence DNS data of Lee [38]. The DNS velocity-gradient statistics are computed at the peak of dissipation in a simulation with initial values of turbulent Mach number and Taylor-scale Reynolds number of 0.88 and 55.6, respectively. The probability density functions are conditioned on various values of a_{ii} ranging from -1.4 to 1.65. Figures 12(a), 13(a) and 14(a) show the probability density functions of the normalized eigenvalues (α^*, β^* and γ^*) computed from DNS data. Each of these probability density functions is a single-peaked distribution with a moderate spread around the peak. For example, the probability density function of the largest eigenvalue conditioned on $a_{ii} = -1.4$ has a peak at $\alpha^* = -0.15$ with a spread in the range: $-0.4 < \alpha^* < 0.1$.

The DNS probability density functions of the intermediate eigenvalue (β^*) shift monotonically from left to right as a_{ii} increases. The corresponding shifts for the largest (α^*) and the smallest (γ^*) eigenvalues are non-monotonic. The arrows placed on the corresponding figures indicate the direction of these shifts with increasing a_{ii}. For the largest eigenvalue, the reversal in the direction of shift happens at a high positive a_{ii}, whereas for the smallest eigenvalue the reversal happens at a high negative a_{ii}. All these features observed in DNS are very well recovered by HEE in Figures 12(b), 13(b) and 14(b). Remarkably, the values of dilatation at which the trends reverse are captured very accurately by HEE.

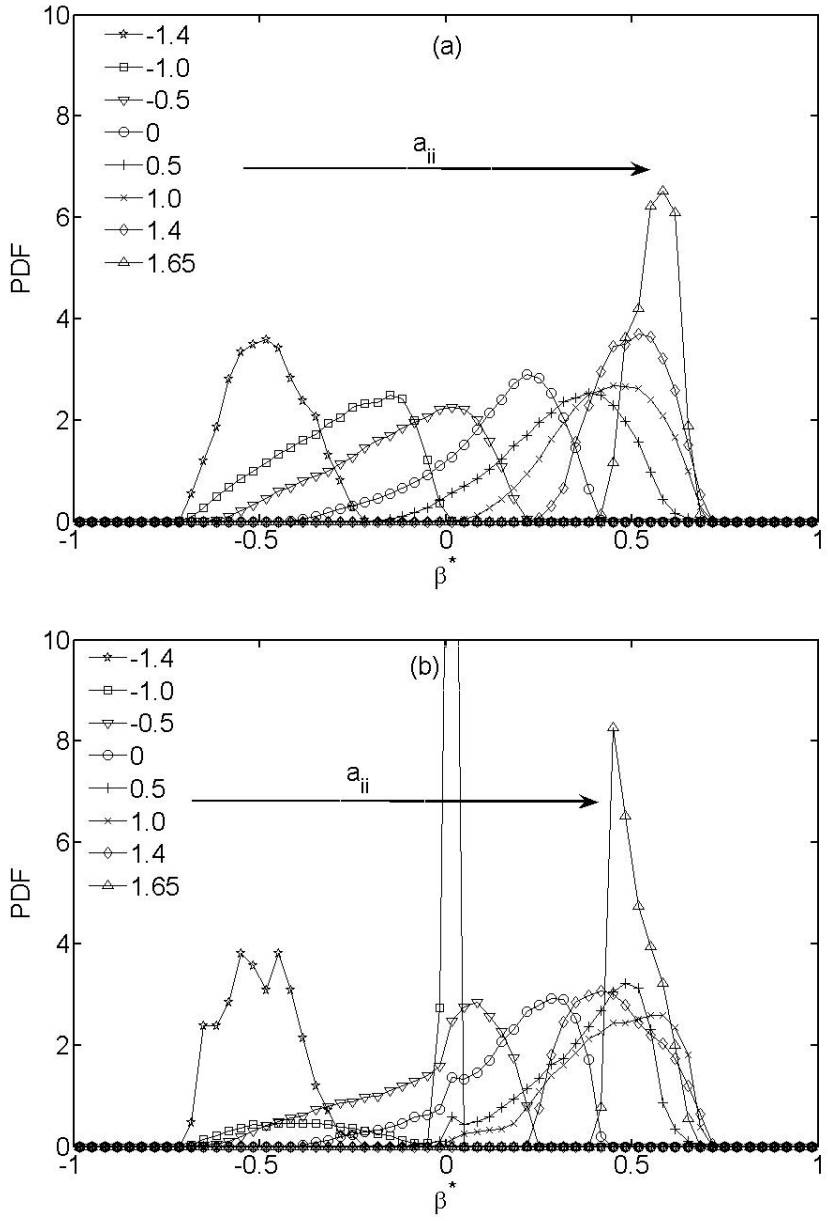

Fig. 13. Probability density functions of normalized intermediate strain-rate eigenvalue (β^*) conditioned on various values of a_{ii} . (a) Compressible DNS (b) HEE.

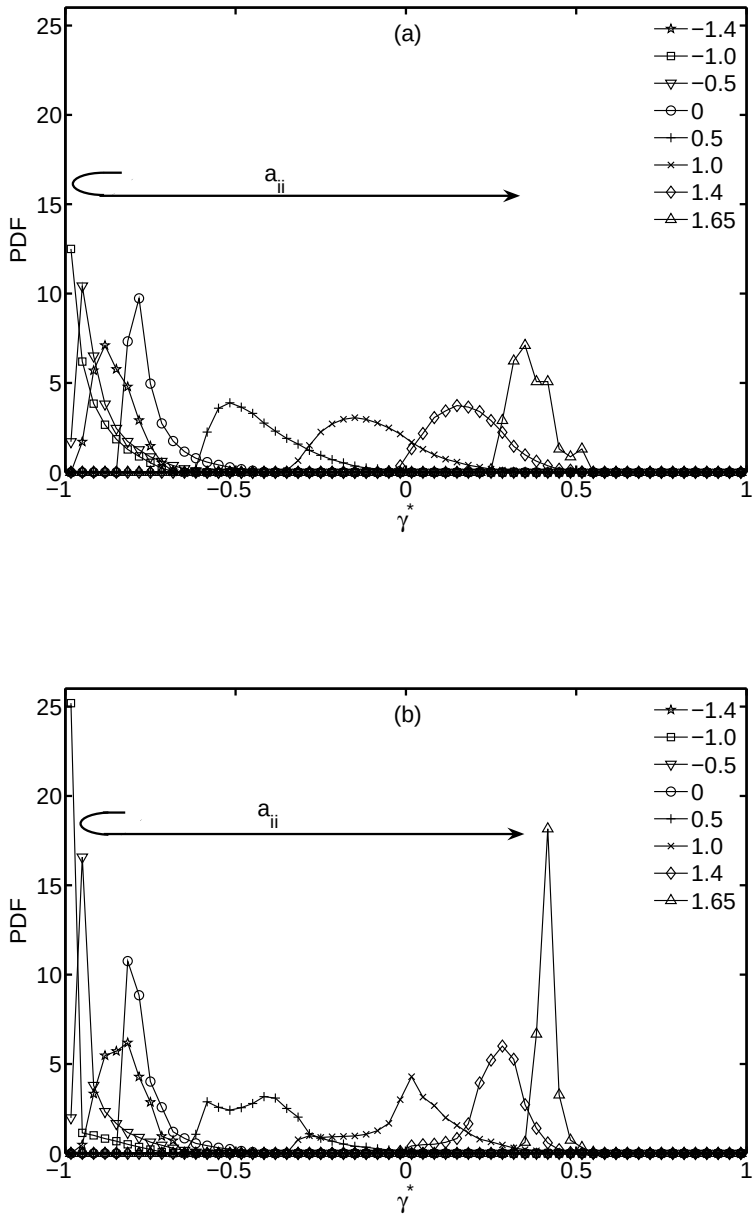

Fig. 14. Probability density functions of normalized smallest strain-rate eigenvalue (γ^*) conditioned on various values of a_{ii}. (a) Compressible DNS (b) HEE.

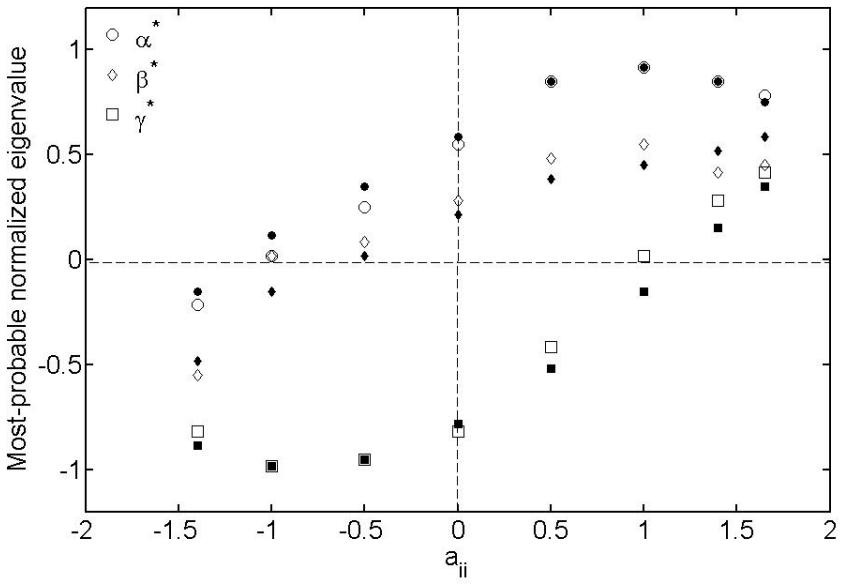

Fig. 15. Most-probable normalized strain-rate eigenvalues (α^*, β^*, γ^*) vs. a_{ii}. Closed symbols: Compressible DNS. Open symbols: HEE.

Next we compare the shapes of the probability density functions. It is clear that the HEE does not recover exactly the shapes of the probability density functions seen in DNS. However, there are some ranges of a_{ii} over which the agreement is good. For the largest eigenvalue the HEE distributions become increasingly more accurate as a_{ii} approaches higher positive values. The HEE probability density functions for the intermediate eigenvalue are fairly close to their DNS counterparts at moderately-negative and moderately-positive dilatations. The distinct asymmetry of the β^* probability density functions seen in DNS at moderate dilatations is well reproduced by HEE. For the smallest eigenvalue the agreement between the DNS and HEE distributions gets better at high negative dilatations.

With Figure 15 we take a closer look at the dependence of most-probable strain-rate eigenvalues (peaks of the probability density functions in Figures 12–14) on normalized dilatation. The agreement between the HEE and DNS values is gen-

erally good with an exception at $a_{ii} = -1$. At this dilatation the HEE computations show that the strain-rate tensor is under severe uni-axial compression with $(\alpha^*, \beta^*, \gamma^*) \approx (0.02, 0.02, -0.98)$, which is somewhat different from the DNS behaviour $[(\alpha^*, \beta^*, \gamma^*) \approx (0.12, -0.15, -0.98)]$. One of the possible reasons for this discrepancy could be the role of viscosity. HEE computations reveal that almost all contracting particles with $a_{ii} = -1$ are associated with very large velocity-gradient magnitudes and hence sizable viscous effects. It is plausible that dissipation and viscous effects would dominate the dynamics in these regions. In these high dissipation regions, the isentropic assumption is also questionable.

D. Conclusions

Under the assumptions of uniform velocity gradients in an inviscid compressible and isentropic flow field, we develop a model - the homogenized Euler equation (HEE) - for describing compressible velocity gradient dynamics. The medium is assumed to be a calorically perfect gas. Coupling between the energy and momentum equation is invoked through the perfect gas state and energy equations. The pressure Hessian evolves as dictated by thermodynamic considerations. In contrast to the restricted Euler equation (REE), the anisotropic pressure Hessian effects are retained intact in this approach. The model comprises of 15 ordinary differential equations in 15 unknowns. Computations are performed for an ensemble of random initial velocity gradient tensors. We study various statistics pertaining to the structure of the velocity gradient tensor conditioned upon normalized dilatation. HEE results in the incompressible limit compare very well against direct numerical simulation (DNS) results of incompressible decaying isotropic turbulence. Moreover, in this limit the HEE computations are much improved over the asymptotic REE results. At vari-

ous non-zero dilatations the HEE very well captures many features of the principal strain-rate statistics seen in compressible DNS. The HEE behviour in the high-Mach number (pressure-released) limit is consistent with Burgers velocity gradient dynamics. The HEE is put forward as a useful model to describe velocity gradient dynamics in compressible turbulence.

CHAPTER IV

ENHANCED HOMOGENIZED EULER EQUATION FOR MODELING COMPRESSIBLE VELOCITY GRADIENT DYNAMICS

In Chapter III we developed a model for compressible velocity gradient dynamics – homogenized Euler equation (HEE). The model relies on the central assumption that the higher gradients of velocity gradient tensor are negligible. This assumption removes all the non-local terms in the pressure Hessian evolution equation and leads to a closed set of ordinary differential equations. An important feature of the HEE model is that, unlike restricted Euler equation (REE), both isotropic and anisotropic portions of the pressure Hessian tensor evolve in time. The HEE model results conditioned upon normalized dilatation show excellent agreement [26] with the behavior seen in DNS of compressible decaying turbulence. However, HEE is not a complete model of compressible velocity gradient dynamics, and it needs improvements. Although HEE results show good agreement with the DNS results of compressible turbulence when various statistics are conditioned upon dilatation, the time evolution of dilatation itself is not captured accurately.

Theoretical analysis and computational evidence [49, 50] of homogeneous isotopic turbulence at low turbulent Mach numbers (M_t) show that the solenoidal component of the velocity field evolves on a fluid scale, whereas the dilatational component evolves on an acoustic time scale. Sarkar et al. [50] further demonstrate that in decaying isotropic turbulence up to $M_t = 0.5$, the statistics of fast changing variables (for example root mean squared value of dilatation or compressible dissipation rate) tend to attain quasi-equilibrium state with respect to the slow changing flow variables (root mean squared value of vorticity or solenoidal dissipation rate). This phenomenon is altogether absent in the HEE model, wherein both dilatational and solenoidal parts

of the velocity gradient tensor evolve on the same time scale – the time scale of fluid motion (discussed in Chapter III). Clearly, the HEE model needs improvement in order to reproduce the actual behavior seen in compressible turbulence. The homogeneous entropy (homentropic) assumption and missing viscous effects are other areas in which the HEE model requires improvement, before it can be employed for wider applications.

Thus the objective of this chapter is to further enhance the original HEE model. Toward this end we (i) modify and improve the modeled pressure Hessian evolution equation to introduce an appropriately defined acoustic time scale in the model, and (ii) model the effects of viscosity in both the velocity gradient and pressure Hessian equations. These enhancements also remove the homentropic constraint of the original model. We evaluate the enhanced model in different flow regimes. At a very small Mach number (incompressible regime), model performance is compared against incompressible DNS results [5]. At a very high Mach number (pressure-released regime), we compare the model results with Burgers velocity gradient dynamics [39]. At moderate subsonic Mach numbers, we evaluate the model against known theoretical and computational results of compressible turbulence [51, 38, 50].

This chapter is organized into 4 sections. In Section B, we develop the enhancement of the HEE model and also identify the non-dimensional parameters of the enhanced model. Section C presents the results of the enhanced model and compares them against known turbulence behavior in various flow regimes.

A. Enhanced homogenized Euler equation

In this section, we modify the modeled pressure Hessian equation and introduce an acoustic time scale into the model. Next we model the missing viscosity effects in both

the velocity gradient and pressure Hessian evolution equations. In the last part of this section, we perform a dimensional analysis of the model and identify its inherent non-dimensional parameters.

1. Inclusion of acoustic time scale

We start with the HEE model equations:

$$\frac{\mathrm{d}A_{ij}}{\mathrm{d}t} = -A_{ik}A_{kj} - P_{ij}; \tag{4.1}$$

$$\frac{\mathrm{d}P_{ij}}{\mathrm{d}t} = -A_{kj}P_{ik} - A_{ki}P_{kj} - (n-1)A_{pp}P_{ij} \tag{4.2}$$

where n is the specific heat ratio of the medium, and A_{ij} and P_{ij} are the velocity gradient and the pressure Hessian tensors:

$$A_{ij} \equiv \frac{\partial V_i}{\partial x_j}; \tag{4.3}$$

$$P_{ij} \equiv \frac{\partial}{\partial x_j}\left(\frac{1}{\rho}\frac{\partial p}{\partial x_i}\right). \tag{4.4}$$

The quantities V_i, p, ρ and n denote velocity, pressure, density and specific heat ratio of the medium. The symbols t and x_i denote time and spatial co-ordinate. Equations (4.1) and (4.2) form a closed set of 18 ordinary differential equations (ODE) modeling the evolution of velocity gradients in a compressible flow. Note that with the above definition of P_{ij} (4.4), the model (4.1)–(4.2) is no more subject to the homentropy constraint under which the HEE model was developed in Chapter III.

As stated in the beginning of this chapter, irrespective of the initial conditions, the trace of velocity gradient tensor or dilatation (A_{ii}) in (4.1) evolves on the same time scale as the solenoidal ($A_{ij} - A_{ii}\frac{\delta_{ij}}{3}$) portion of the tensor. This model behavior is not consistent with the known behavior of compressible turbulence and hence warrants modifications in the HEE model. In order to address this inadequacy of the model

and to suggest improvements, we first examine the evolution equation of A_{ii} in the HEE model. Taking the trace of (4.1) we get:

$$\frac{\mathrm{d}A_{mm}}{\mathrm{d}t} = -A_{mk}A_{km} - P_{mm}. \tag{4.5}$$

The right hand side (rhs) of 4.5 is exact for inviscid flows. Thus, the dependence of the evolution A_{ii} on an acoustic time scale must appear through the evolution equation of the pressure term, P_{mm}. In the HEE model, the quantity P_{mm} evolves through the following modeled equation:

$$\frac{\mathrm{d}P_{mm}}{\mathrm{d}t} = -A_{km}P_{mk} - A_{km}P_{km} - (n-1)A_{pp}P_{mm}. \tag{4.6}$$

Upon inspection we find that the only time scale appearing in the evolution equation of P_{mm} is the time scale $1/|A|$, which is the time scale of fluid motion ($|A| \equiv \sqrt{A_{mn}A_{mn}}$). In low Mach number flows, this time scale is much larger than the acoustic time scale. Thus, the unphysical time evolution of A_{mm} in the HEE model (4.1-4.2) is certainly attributable to the neglect of an acoustic time scale in the evolution equation of the trace of the pressure Hessian tensor, P_{mm}. Thus, an improvement in the HEE model requires a modification or replacement of the modeled equation for P_{mm} by a physically more viable model. In this work we propose an improved model for P_{mm}. For the sake of brevity, we represent P_{mm} by Z. Using this notation, we now express the pressure Hessian tensor as a combination of isotropic ($Z\delta_{ij}/3$) and anisotropic portions (Q_{ij}):

$$P_{ij} = Q_{ij} + Z\frac{\delta_{ij}}{3}. \tag{4.7}$$

Note that a straightforward implication of this decomposition is: $Q_{mm} \equiv 0$.

To arrive at a physically sensible model for Z, we use one assumption of pseudo-sound theory (used earlier by Ristorcelli [52] to derive turbulence models for pressure-

dilatation correlation and compressible dissipation rate). The cornerstone of pseudo-sound theory is the physics that very near to a source of sound, which in our case is a small fluid particle, the fluid behaves as if it were incompressible [52, 53]. This implies that very near to a small fluid particle, pressure is governed by the Poisson equation. In our context this implies:

$$Z \equiv P_{ii} = -A_{lm}A_{ml}. \tag{4.8}$$

Further assuming that the degree of "nearness" increases with the local speed of sound (c) and decreases with the length scale (L) associated with the fluid particle under consideration, we propose a simple prognostic model for the evolution of Z in a compressible flow field

$$\frac{\mathrm{d}Z}{\mathrm{d}t} = -\left(Z + A_{lm}A_{ml}\right)\frac{c}{L}. \tag{4.9}$$

Note that the quantity c/L appearing on the rhs of (4.9) is a measure of a local acoustic time scale. As expected, this prognostic model can now allow the isotropic portion of the pressure Hessian to evolve on an acoustic time scale. We assume c to be constant in our model. The length L, however, is subject to large variations because of intense fluid deformation induced by turbulence. L indeed depends on the deformation history of a fluid element. In Lagrangian analysis, the deformation history of a fluid element is associated with the deformation tensor C_{ij}:

$$C_{ij} \equiv \frac{\partial X_i}{\partial x_j} \tag{4.10}$$

where x and X denote the position vector of the fluid particle in Eulerian and Lagrangian descriptions, respectively. Following the precedence of Jeong et al. [31], we estimate the length scale, L, associated with a fluid element as:

$$L \approx \frac{L_o}{\sqrt{C_{pq}C_{pq}/3}} \tag{4.11}$$

where L_o is the initial length scale associated with the Lagrangian particle. The exact evolution of the deformation tensor (C_{ij}), in turn, is governed by the following equation [31]:

$$\frac{\mathrm{d}M_{ij}}{\mathrm{d}t} = A_{ik}M_{kj} \tag{4.12}$$

where $\mathrm{M} \equiv \mathrm{C}^{-1}$.

Having obtained a new model equation (4.9) for the isotropic portion (4.7) of the pressure Hessian tensor, the trace of (4.2) must be modified. The trace of (4.2) is now redundant. This redundancy is removed by subtracting out the trace of (4.2) leading to the following equation of the anisotropic portion (Q_{ij}) of the pressure Hessian tensor:

$$\begin{aligned} \frac{\mathrm{d}Q_{ij}}{\mathrm{d}t} = & - A_{kj}Q_{ik} - A_{ki}Q_{kj} - (n-1)A_{pp}Q_{ij} \\ & - (-A_{km}Q_{mk} - A_{km}Q_{km})\frac{\delta_{ij}}{3}. \end{aligned} \tag{4.13}$$

Thus, we now have a model for compressible velocity gradient evolution in which the isotropic portion (Z) of the pressure Hessian evolves through (4.9) at an acoustic time scale, and the anisotropic portion (Q_{ij}) evolves through (4.13) at more of a fluid time scale.

We summarize this sub-section as follows. Driven by the need to have a physically correct evolution of dilatation in the HEE model developed in Chapter III, we decompose the pressure Hessian tensor into its isotropic and anisotropic portions (4.7). Based on relevant physical arguments, we develop a new model equation (4.9) for the isotropic portion of the pressure Hessian tensor, allowing it to evolve on an acoustic time scale. The equation for the anisotropic pressure Hessian (4.13) is extracted from the pressure Hessian equation of the HEE model of Chapter III. As a

result, the HEE model is enhanced to the following form:

$$\frac{\mathrm{d}A_{ij}}{\mathrm{d}t} = -A_{ik}A_{kj} - Q_{ij} - Z\frac{\delta_{ij}}{3}; \tag{4.14}$$

$$\begin{aligned}\frac{\mathrm{d}Q_{ij}}{\mathrm{d}t} = &-A_{kj}Q_{ik} - A_{ki}Q_{kj} - (n-1)A_{pp}Q_{ij} \\ &- \left(-A_{km}Q_{mk} - A_{km}Q_{km}\right)\frac{\delta_{ij}}{3};\end{aligned} \tag{4.15}$$

$$\frac{\mathrm{d}Z}{\mathrm{d}t} = -\left(Z + A_{lm}A_{ml}\right)\frac{c}{L}; \tag{4.16}$$

$$\frac{\mathrm{d}M_{ij}}{\mathrm{d}t} = A_{ik}M_{kj}; \tag{4.17}$$

$$L = \frac{L_o}{\sqrt{C_{pq}C_{pq}/3}}; \tag{4.18}$$

$$\mathrm{C} = \mathrm{M}^{-1}. \tag{4.19}$$

Equations (4.14) – (4.19) comprise a closed set of 27 ordinary differential equations (ODEs) modeling the evolution of the velocity gradient tensor in an inviscid compressible and calorically perfect medium.

2. Viscous effects modeling

The model equation set (4.14) – (4.19) is algebraically closed but physically still an incomplete model of compressible velocity gradient dynamics. The model lacks the effects of viscosity on the evolving quantities. In the absence of viscosity, velocity gradient magnitudes evolve to impractically high values. This is reminiscent of the behavior seen in incompressible Euler turbulence [45, 54] and even in the REE model [4, 29]. To make the HEE model applicable for wider practical applications, the effects of viscosity must be included in the model. However, including the exact viscosity terms in a Lagrangian dynamical system like (4.14) – (4.19) is not possible. The exact viscous terms are inherently non-local, and their inclusion will lead to obvious

closure problems. Thus, the effects of viscosity must be modeled.

In the context of modeling incompressible velocity gradient dynamics (REE model), the approach of using a diffusion model [40] along with Lagrangian-Eulerian change in variables [31, 32] has successfully been employed for modeling viscous effects. In this work we follow a similar approach. However it should be noted that modeling viscous effects on compressible velocity gradient dynamics has an important difference, as compared to the viscous effects on incompressible velocity gradient dynamics. In incompressible turbulence, viscosity influences the velocity gradients only through the process of momentum diffusion, and has no direct bearing on the pressure Hessian tensor. The pressure Hessian tensor depends directly on the velocity field through the Poisson equation. In contrast, in compressible turbulence, the evolution of the pressure Hessian tensor is dependent on energy equation [26]. Thus, the pressure Hessian tensor (and in turn the velocity gradient tensor) is subject to the conductive and heating effects of viscosity as well via the energy equation. Thus, a comprehensive account of viscous effects on compressible velocity gradient dynamics requires modeling not only the diffusive action of viscosity in momentum equation but its energy-conducting and viscous-heating effects in energy equation as well. In this work, we ignore the viscous-heating effects. However, we do model the viscous conductive effects in addition to the effects of viscosity, in the momentum/velocity-gradient equation.

It can be easily demonstrated that the exact viscous contribution (Δ_{ij}) in the evolution equation of A_{ij} is:

$$\Delta_{ij} \equiv \frac{\partial}{\partial x_j}\left(\frac{1}{\rho}\frac{\partial \sigma_{ik}}{\partial x_k}\right) \tag{4.20}$$

where ρ and σ_{ij} represent density and the viscous stress tensor. The constitutive

relationship for a compressible Newtonian fluid is:

$$\sigma_{ij} = \mu \left(A_{ij} + A_{ji} \right) + \lambda A_{pp} \delta_{ij}. \tag{4.21}$$

where μ and λ represent the first and second coefficients of viscosity. Using Stoke's hypothesis ($\lambda = -2\mu/3$)[55], the constitutive relationship (4.21) simplifies to:

$$\sigma_{ij} = \mu A_{ij} + \mu A_{ji} - \frac{2}{3} \mu A_{pp} \delta_{ij}. \tag{4.22}$$

Substituting (4.22) in (4.20), we express Δ_{ij} in terms of the velocity gradient tensor, A_{ij}:

$$\Delta_{ij} = \nu \left(\frac{\partial^2 A_{ij}}{\partial x_k \partial x_k} + \frac{1}{3} \frac{\partial^2 A_{pp}}{\partial x_i \partial x_j} \right) \tag{4.23}$$

where $\nu = \mu/\rho$ and the spatial variations in ρ and the μ have been neglected to avoid further complexity in modeling the viscous effects. Clearly, (4.23) has non-local terms (higher gradients of A_{ij}), and these terms require modeling. We attempt to model these viscous terms employing the Linear Lagrangian Diffusion Modeling (LLDM) approach of Jeong et al. [31]. Using Eulerian-Lagrangian change of variables, Δ_{ij} can be expressed as:

$$\begin{aligned} \nu \left[\frac{\partial^2 A_{ij}}{\partial x_k \partial x_k} \right] &+ \nu \left[\frac{1}{3} \frac{\partial^2 A_{pp}}{\partial x_i \partial x_j} \right] \\ &= \nu \left[\frac{\partial^2 A_{ij}}{\partial X_n \partial X_m} \frac{\partial X_n}{\partial x_k} \frac{\partial X_m}{\partial x_k} + \frac{\partial A_{ij}}{\partial X_m} \frac{\partial^2 X_m}{\partial X_n \partial x_k} \frac{\partial X_n}{\partial x_k} \right] \\ &+ \nu \left[\frac{\partial^2 A_{pp}}{\partial X_n \partial X_m} \frac{\partial X_m}{\partial x_j} \frac{\partial X_n}{\partial x_i} + \frac{\partial A_{pp}}{\partial X_m} \frac{\partial^2 X_m}{\partial X_n \partial x_j} \frac{\partial X_n}{\partial x_i} \right] \end{aligned} \tag{4.24}$$

where X and x denote the Lagrangian and Eulerian co-ordinates, respectively. Invoking the assumptions of the LLDM approach [31], we neglect the higher order terms

in (4.24) and arrive at the following approximation:

$$\nu\left[\frac{\partial^2 A_{ij}}{\partial x_k \partial x_k}\right] + \nu\left[\frac{1}{3}\frac{\partial^2 A_{pp}}{\partial x_i \partial x_j}\right] \approx \nu\left[\frac{\partial^2 A_{ij}}{\partial X_n \partial X_m}\frac{\partial X_n}{\partial x_k}\frac{\partial X_m}{\partial x_k}\right] + \nu\left[\frac{\partial^2 A_{pp}}{\partial X_n \partial X_m}\frac{\partial X_m}{\partial x_j}\frac{\partial X_n}{\partial x_i}\right]$$
$$= \nu\left[\frac{\partial^2 A_{ij}}{\partial X_n \partial X_m} C_{nk} C_{mk}\right] + \nu\left[\frac{\partial^2 A_{pp}}{\partial X_n \partial X_m} C_{mj} C_{ni}\right] \quad (4.25)$$

Note that the tensor C_{ij} is the deformation tensor as defined in (4.10). The first term appearing on the rhs of (4.25) involves the second order tensor $C_{mk}C_{nk}$ and is exactly the same term as in incompressible velocity gradient equation [40, 31]. Thus, we treat this term in the same way as modeled by Jeong et al. [31]:

$$\left[\nu C_{mk} C_{nk} \frac{\partial^2 A_{ij}}{\partial X_m \partial X_n}\right] \approx -\frac{C_{pq}C_{pq}}{3\tau_v} A_{ij} \quad (4.26)$$

where the quantity τ_v is a constant to be interpreted as the molecular viscous relaxation time scale.

The second term in (4.25) involves the second gradient of dilatation (A_{pp}) and the fourth order tensor $C_{mj}C_{ni}$. This term is zero in incompressible flows, but may have non-zero contribution in compressible flows. However, the nature of this term being different from the first viscous term in (4.25), it is not very straightforward to extend the diffusion-type modeling approach to this term. In this work, we ignore the effects of this term on compressible velocity gradients. Thus, using (4.26), (4.14) is augmented to the following form:

$$\frac{\mathrm{d}A_{ij}}{\mathrm{d}t} = -A_{ik}A_{kj} - P_{ij} - \frac{C_{pq}C_{pq}}{3\tau_v} A_{ij}. \quad (4.27)$$

The evolution of the quantity $C_{pq}C_{pq}$ appearing in (4.27) has already been included in the model (4.17 and 4.19). However, in an inviscid flow wherein the evolution of $C_{pq}C_{pq}$ is unrestricted, in viscous flows we must impose an upper bound on $C_{pq}C_{pq}$ in accordance with the known limiting behavior of viscous action. At smallest

scales of motion, the fluid is strongly affected by viscous forces. The Reynolds number based at these small scales of motion is restricted to be of order unity [56, 57]:

$$Re \approx 1. \tag{4.28}$$

The Reynolds number is a measure of the relative significance of inertia to the viscous effects. In the context of our velocity gradient model, the relevant Reynolds number can be defined as the ratio of self-stretching (first term on rhs of (4.27) to viscous terms (third term on rhs of (4.27)). A simple order of magnitude analysis of (4.27) leads to an estimate of the order of magnitude of the relevant Reynolds number in our velocity gradient model (more on this in Section C):

$$Re = O\left(\frac{|A_{ik}A_{kj}|}{C_{pq}C_{pq}\,|A_{ij}|\,/3\tau_v}\right) \sim O\left(\frac{3\tau_v\,|A|}{C_{pq}C_{pq}}\right) \tag{4.29}$$

where $|A|$ is the instantaneous magnitude of the velocity gradient tensor. Now we employ (4.28) in the limiting regime of viscous action to arrive at a corresponding bound on the magnitude of $C_{pq}C_{pq}$:

$$1 \leq Re \Rightarrow C_{pq}C_{pq} \leq 3\tau_V\,|A|\,.$$

We use this bound on $C_{pq}C_{pq}$ for all our computations discussed in the next sections.

Using a similar modeling approach, we augment the evolution equation of the traceless (anisotropic) portion of the pressure Hessian (4.15) with the conductive effects of viscosity:

$$\begin{aligned}\frac{\mathrm{d}Q_{ij}}{\mathrm{d}t} = &- A_{kj}Q_{ik} - A_{ki}Q_{kj} - (n-1)A_{pp}Q_{ij} - \frac{C_{pq}C_{pq}}{3\tau_p}Q_{ij} \\ &- (-A_{km}Q_{mk} - A_{km}Q_{km})\,\frac{\delta_{ij}}{3}.\end{aligned} \tag{4.30}$$

The quantity τ_p appearing in (4.30) is a constant to be interpreted as the time scale

associated with the (molecular) heat conduction process in the fluid. The relationship between τ_p with τ_v is discussed in the next sub-section.

Note that (4.16), which is the evolution equation of the isotropic portion (Z) of the pressure Hessian, needs no viscous model. The tendency of the isotropic portion of the pressure Hessian to impose divergence-free velocity field depends only on the interaction of acoustic and inertial processes, and thus is truly an inviscid effect.

In summary, as a result of the viscous enhancements introduced in this sub-section, the equation set (4.14) – (4.19) modifies to the following form

$$\frac{\mathrm{d}A_{ij}}{\mathrm{d}t} = -A_{ik}A_{kj} - Q_{ij} - Z\frac{\delta_{ij}}{3} - \frac{C_{pq}C_{pq}}{3\tau_v}A_{ij}; \tag{4.31}$$

$$\begin{aligned}\frac{\mathrm{d}Q_{ij}}{\mathrm{d}t} = -A_{kj}Q_{ik} \;&-\; A_{ki}Q_{kj} - (n-1)A_{pp}Q_{ij} - \frac{C_{pq}C_{pq}}{3\tau_p}Q_{ij} \\ &-\; \left(-A_{km}Q_{mk} - A_{km}Q_{km}\right)\frac{\delta_{ij}}{3};\end{aligned} \tag{4.32}$$

$$\frac{\mathrm{d}Z}{\mathrm{d}t} = -\left(Z + A_{lm}A_{ml}\right)\frac{c}{L}; \tag{4.33}$$

$$\frac{\mathrm{d}M_{ij}}{\mathrm{d}t} = A_{ik}M_{kj}; \tag{4.34}$$

$$L = \frac{L_o}{\sqrt{C_{pq}C_{pq}/3}}; \tag{4.35}$$

$$\mathrm{C} = \mathrm{M}^{-1}. \tag{4.36}$$

Equations (4.31) – (4.36) form a coupled set of 27 ODEs. We refer to this equation set as the enhanced homogenized Euler equation (EHEE) and propose it as a model for velocity gradient dynamics in a compressible viscous and calorically perfect medium.

3. Non-dimensional parameters

Similar to the full Navier-Stokes (NS) equation set for compressible flows, the EHEE model (4.31) – (4.36) involves inertial, acoustic and viscous time scales. In order to

better understand the influence of these time scales on compressible velocity gradient dynamics, we must examine the non-dimensional form of the EHEE model. Thus, in this sub-section, we first non-dimensionalize (4.31) – (4.36) and isolate the inherent non-dimensional parameters of the model. Next, we highlight the physical significance of these parameters. Finally we discuss the analogies between the non-dimensional parameters of the EHEE model and those of full Navier–Stokes equations (Mach number, Reynolds number, etc.).

To non-dimensionalize (4.31) – (4.36), we choose a characteristic value of each quantity appearing in these equations. We choose scalars L^* and Z^* as the characteristic values of the length scale (L) and the isotropic part (Z) of the pressure Hessian tensor, respectively. The scalars A^*, Q^* and M^* are chosen as the characteristic values of the magnitudes of the A_{ij}, Q_{ij} and M_{ij} tensors, respectively. Having chosen A^*, the quantity $1/A^*$ can be considered as the characteristic time scale of the fluid motion. Each variable in the model equation set can now be expressed in terms of the normalized variable (denoted by an over bar) and the corresponding characteristic value:

$$\begin{aligned} t = \frac{\bar{t}}{A^*}; \quad L &= \overline{L} L^*; \quad Z = \overline{Z} Z^*; \\ A_{ij} = \overline{A}_{ij} A^*; \quad Q_{ij} &= \overline{Q}_{ij} Q^*; \quad M_{ij} = \overline{M}_{ij} M^*. \end{aligned} \tag{4.37}$$

Since dilatation (A_{ii}) can have a very different magnitude than that of the velocity gradient tensor itself, we need to have another characteristic scalar, χ, to appropriately non-dimensionalize A_{ii}. The quantity χ must be chosen such that:

$$A_{ii} = \chi \overline{A}_{ii} A^*. \tag{4.38}$$

Note that for a strictly incompressible flow, $\chi \equiv 0$.

Substituting (4.37) and (4.38) in (4.31) –(4.36) and subsequently grouping the characteristic quantities together, we are led to the following equations:

$$\frac{\mathrm{d}\overline{A}_{ij}}{\mathrm{d}\bar{t}} = -\overline{A}_{ik}\overline{A}_{kj} - \phi\overline{Q}_{ij} - \psi\overline{Z}\frac{\delta_{ij}}{3} - \frac{1}{Re_M}\overline{A}_{ij}; \tag{4.39}$$

$$\begin{aligned}\frac{\mathrm{d}\overline{Q}_{ij}}{\mathrm{d}\bar{t}} = -\overline{A}_{kj}\overline{Q}_{ik} \;&-\; \overline{A}_{ki}\overline{Q}_{kj} - (n-1)\chi\overline{A}_{pp}\overline{Q}_{ij} - \frac{1}{\theta}\overline{Q}_{ij} \\ &-\; \left(-\overline{A}_{km}\overline{Q}_{mk} - \overline{A}_{km}\overline{Q}_{km}\right)\frac{\delta_{ij}}{3};\end{aligned} \tag{4.40}$$

$$\frac{\mathrm{d}\overline{Z}}{\mathrm{d}\bar{t}} = -\frac{1}{M_M}\left(\overline{Z} + \frac{1}{\psi}\overline{A}_{lm}\overline{A}_{ml}\right)\frac{1}{\overline{L}}; \tag{4.41}$$

$$\frac{\mathrm{d}\overline{M}_{ij}}{\mathrm{d}\bar{t}} = \overline{A}_{ik}\overline{M}_{kj}; \tag{4.42}$$

$$\overline{L} = \frac{\overline{L}_o}{\sqrt{C_{pq}C_{pq}/3}}; \tag{4.43}$$

$$\mathrm{C} = (\overline{\mathrm{M}}\mathrm{M}^*)^{-1}. \tag{4.44}$$

where the five non-dimensional parameters have the following definitions:

$$\begin{aligned}\phi \equiv \frac{Q^*}{A^{*2}}; \qquad \psi \equiv \frac{Z^*}{A^{*2}}; \\ Re_M \equiv \frac{3\tau_v A^*}{C_{pq}C_{pq}}; \quad \theta \;\equiv\; \frac{3\tau_p A^*}{C_{pq}C_{pq}}; \quad M_M \equiv \frac{A^*L^*}{c}.\end{aligned} \tag{4.45}$$

The single most important non-dimensional parameter appearing in (4.39) – (4.44) is $M_M \equiv \frac{c}{A^*L^*}$. This really is a gradient Mach number. The parameter M_M appears in (4.41) and directly determines the tendency of the isotropic portion of the pressure Hessian to impose incompressibility on the fluid particle. Clearly, M_M is a ratio of the acoustic and inertial time scales in the model. Accordingly, we call M_M the model Mach number (M_M). In compressible homogeneous isotropic turbulence, the relevant Mach number is the turbulent Mach number (M_T), which is defined as

[58, 50]:

$$M_T \equiv \sqrt{\frac{u_i u_i}{nRT}} \tag{4.46}$$

where u_i and T are characteristic fluctuating velocity and characteristic mean temperature values and R is gas constant. Since our model equation set for velocity gradients does not have an explicit appearance of velocity, it is not straightforward to provide an exact relationship between M_M and the turbulent Mach number. However, using order of magnitude arguments, we can estimate a relationship between the two Mach numbers:

$$M_T \approx \sqrt{3} M_M. \tag{4.47}$$

Certainly, M_M can be considered a parameter analogous to M_T, as the former is indeed the ratio between the relevant inertial and acoustic time scales in the model.

The parameter Re_M appearing with the last term in rhs of (4.39) determines the importance of viscous terms relative to the inertial terms. Thus Re_M is analogous to the conventional definition of the Reynolds number (Re). The definition of Re_M in (4.45) clearly shows that an increase in τ_v should effectively simulate an increased Reynolds number effect in the EHEE model (and vice-versa). Similarly, the coefficient (θ) appearing in the rhs of (4.40) represents the ratio of thermal conduction terms to inertial terms in the modeled equation. In the exact non-dimensional Navier–Stokes energy equation, the coefficient of conduction term is $\frac{n}{RePr}$ [59], where n and Pr represent the specific heat ratio and Prandtl number of the gaseous medium. Taking a cue from this known fact, we can relate Re_M and θ through the following relationship:

$$\tau_p = \tau_v \frac{n}{Pr} \tag{4.48}$$

where n represents the specific heat ratio of the medium. All EHEE simulation results presented in the next section employ (4.48).

Table XIII. Various non-dimensional parameters in EHEE model and their analogy with the non-dimensional parameters of full compressible Navier-Stokes (NS) equations.

Parameter in EHEE model	Parameter definition	Physical interpretation	Analogous parameter in exact NS equations
M_M	$\frac{A^* L^*}{c}$	$\frac{\text{inertial time scale}}{\text{acoustic time scale}}$	Mach number
Re_M	$\frac{3\tau_v A^*}{C_{pq}C_{pq}}$	$\frac{\text{inertial terms}}{\text{viscous terms}}$	Reynolds number (Re)
θ	$\frac{3\tau_p A^*}{C_{pq}C_{pq}}$	$\frac{\text{inertial terms}}{\text{conduction terms}}$	$\frac{n}{RePr}$
ϕ	$\frac{Q^*}{A^{*2}}$	$\frac{\text{Anisotropic pressure Hessian terms}}{\text{Inertial terms}}$	-
ψ	$\frac{Z^*}{A^{*2}}$	$\frac{\text{Isotropic pressure Hessian term}}{\text{Inertial term}}$	-

The non-dimensional quantity ϕ appearing in (4.39) represents the relative importance of anisotropic pressure Hessian terms to the inertial terms in the evolution equation of A_{ij}. Similarly, ψ – appearing in (4.39) and (4.41) – is the ratio of isotropic pressure Hessian terms to the inertial terms. The order of magnitude of ϕ and ψ must depend on the Mach number regime of the flow. In very low Mach number flows, wherein the pressure field becomes increasingly dependent on velocity field via the Poisson equation, both ϕ and ψ should be order unity. On the other hand, at large Mach numbers, ϕ and ψ must scale as $1/\left(M_M\right)^2$. Table XIII summarizes the discussion of this sub-section.

B. Model evaluation

In this section we evaluate the EHEE model by comparing the model results against known turbulence behavior (DNS and analytical results) in different Mach number and Reynolds number regimes. The variable Mach number and Reynolds number effects are simulated by appropriately changing various non-dimensional parameters identified in Section A (see Table XIII). In the small Mach number regime, the EHEE model recovers the known incompressible turbulence behavior (Sub-section 1). On the other extreme, at an extremely high Mach number, the model behavior resembles Burgers or pressure-released velocity gradient dynamics (Sub-section 2). In the intermediate Mach number regime, we evaluate the model in terms of various Mach number effects on the dilatational and solenoidal components of A_{ij} (Sub-section 3). Lastly, we evaluate the model in terms of various Reynolds number effects on dilatational and solenoidal statistics (Sub-section 4).

All EHEE results are obtained by performing time integration of (4.31) – (4.36). We employ the fourth-order Runge-Kutta method for the purpose. We evaluate the model in terms of statistics of various pertinent quantities. Thus computations are performed for an ensemble of initial conditions or "particles" to obtain these statistics. An optimum sample size of 20,000 particles is used to obtain all the EHEE results presented in this chapter. As indicated in Section A, the set of initial conditions for an EHEE simulation must be chosen in accordance with the simulated Mach number and Reynolds number regime. Specific details of the choice of initial conditions for each EHEE simulation is discussed in the respective sub-sections below.

1. Evaluation at low Mach number: Incompressible limit

In incompressible limit, we evaluate the EHEE model in terms of the structure of (i) the velocity gradient and, (ii) the pressure Hessian tensors. Comparisons are made directly against the behavior seen in DNS of decaying isotropic incompressible turbulence [5]. To simulate the incompressible limit of the EHEE model, the set of initial conditions for a "particle" is chosen as follows. We choose the orders of magnitude of the velocity gradient and pressure Hessian tensors as:

$$\begin{aligned} \sqrt{A_{mn}A_{mn}} &\sim 1; \\ Z &= -A_{lm}A_{lm}; \\ \sqrt{Q_{mn}Q_{mn}} &\sim |A_{lm}A_{ml}| \,. \end{aligned} \tag{4.49}$$

Individual components of A_{ij} and Q_{ij} tensors are generated randomly. A random number generator that produces uniformly distributed numbers between -1 and 1 is employed. Both A_{ij} and Q_{ij} are ensured to be traceless initially. The M_{ij} tensor is chosen to be the identity tensor. The value of c is chosen as 100 to have a small enough value of initial Mach number ($M_M = 0.01$) to simulate the incompressible limit of the model. The molecular viscous relaxation time scale (τ_v) is chosen to be 20, and the value of τ_p is set using (4.48). The initial length scale, L_o, is chosen to be unity. The Prnadtl number and specific heat ratio values are chosen as 0.7 and 1.4, respectively.

All EHEE results discussed in this sub-section are obtained at the non-dimensional time, $tA_o = 5$ where $A_o \equiv \sqrt{A_{mn}A_{mn}}$ at $t = 0$. By this time the averaged pseudo-dissipation of the sample, $\langle A_{ij}A_{ij}\rangle$, reduces to less than one-tenth of its initial value, and thus the non-linear and viscous processes are expected to be in full effect.

We first consider the eigenvalues of the strain-rate tensor S_{ij} ($\equiv (A_{ij} + A_{ji})/2$)

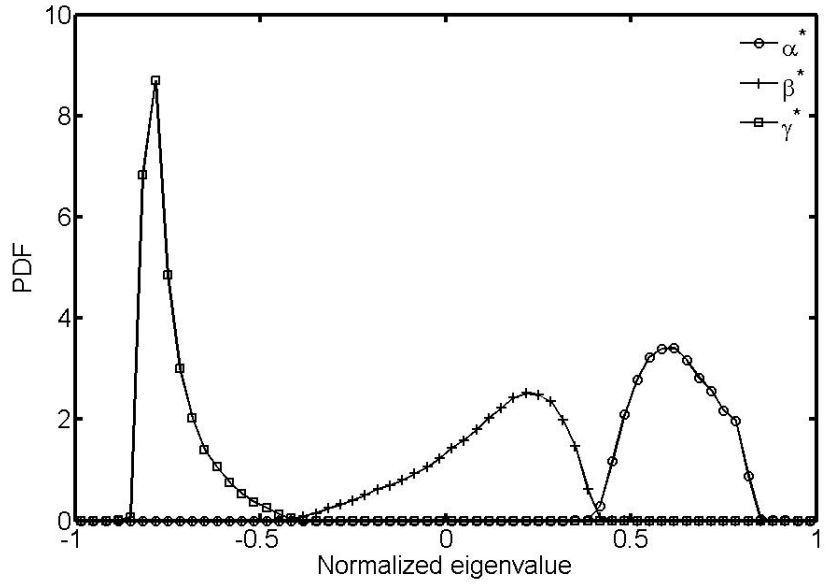

(a)

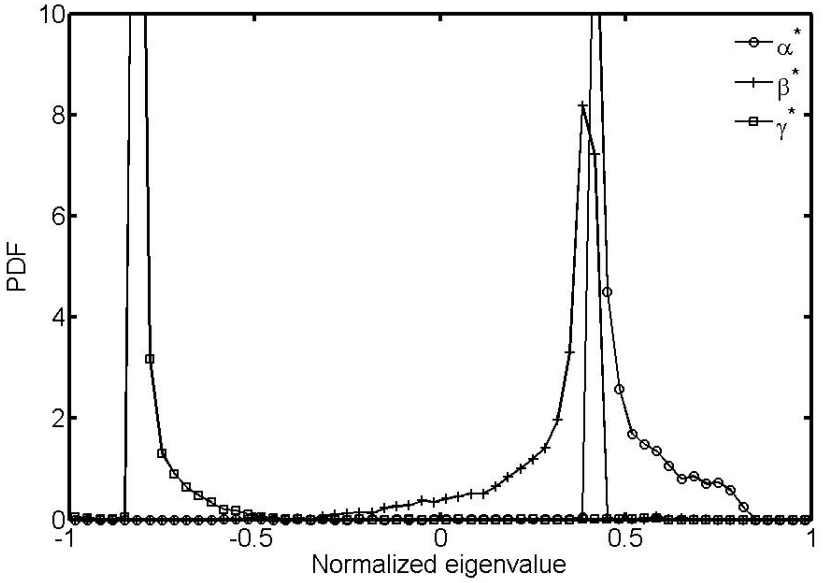

(b)

Fig. 16. Probability density function (PDF) of strain-rate eigenvalues in (a) DNS of incompressible isotropic turbulence, and (b) EHEE simulation at $M_M = 0.01$.

and the alignment tendencies of the vorticity vector (ω) with the eigenvectors of the strain-rate tensor. In several previous studies [5, 54, 45] of incompressible turbulence, two prominent features have been observed: (i) two eigenvalues of the strain-rate tensor are positive, and (ii) vorticity is aligned with the eigenvector corresponding to the smaller positive eigenvalue. Such a preferred structure of the velocity gradient tensor is responsible for intense vortex stretching in incompressible turbulence.

The preferred signs of the strain-rate eigenvalues: α, β, γ ($\alpha \geq \beta \geq \gamma$) [5] and the ratio between these can be studied in terms of the probability density functions (PDF) of the normalized form of these eigenvalues:

$$\alpha^* = \frac{\alpha}{\sqrt{\alpha^2+\beta^2+\gamma^2}} \quad \beta^* = \frac{\beta}{\sqrt{\alpha^2+\beta^2+\gamma^2}} \quad \gamma^* = \frac{\gamma}{\sqrt{\alpha^2+\beta^2+\gamma^2}}. \tag{4.50}$$

On the other hand, the vorticity alignment tendency can be studied in terms of the cosine of the angle between the vorticity vector and the corresponding eigenvector of the strain-rate tensor.

In Figure 16(a), we present the probability density functions α^*, β^* and γ^* as seen in DNS of incompressible decaying isotropic turbulence. In Figure 17(a) PDFs of the cosine of the angle between the vorticity vector and the strain-rate eigenvectors are presented. In Figures 16(b) and 17(b) the corresponding results obtained with EHEE computations are presented. The EHEE model indeed captures the high probability of the two eigenvalues (α and β) to be positive. Moreover, similar to the behavior seen in DNS, the vorticity vector in the EHEE computations clearly shows a very high probability to align with the eigenvector corresponding to the intermediate strain-rate eigenvalue.

Next we consider the pressure Hessian tensor. Analysis and simulation of incompressible Euler flows by Ohkitani et al. [54] and Ohkitani et al. [45] demonstrate that in regions of intense vortex stretching, the vorticity vector must be well aligned with

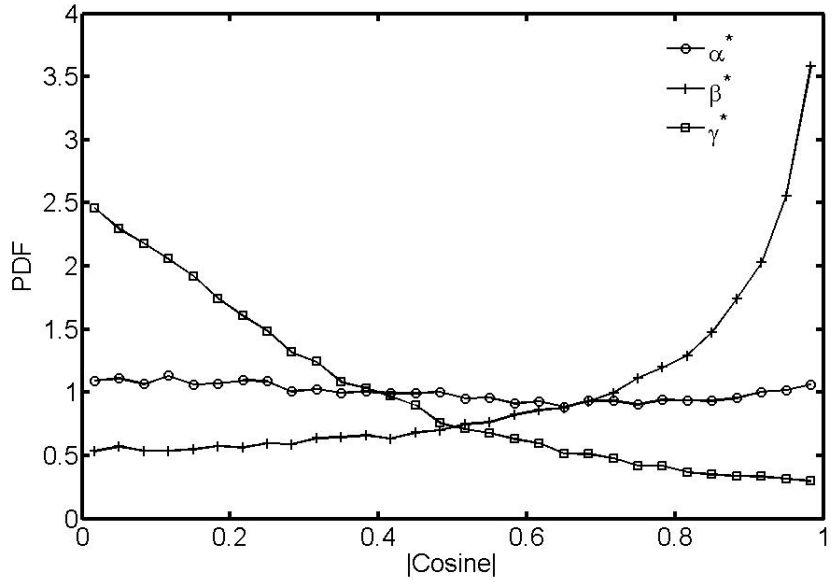

(a)

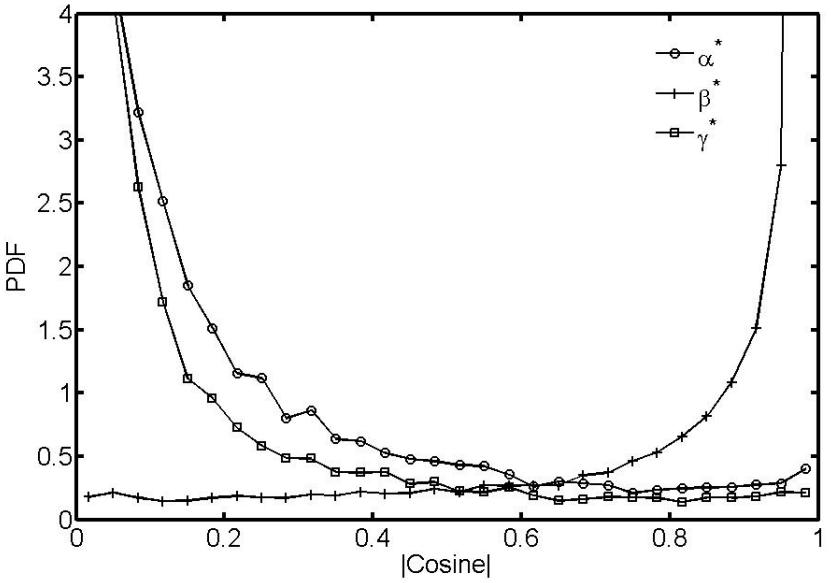

(b)

Fig. 17. PDF of cosine of the angle between vorticity vector and strain-rate eigenvectors in (a) DNS of incompressible isotropic turbulence, and (b) EHEE simulation at $M_M = 0.01$.

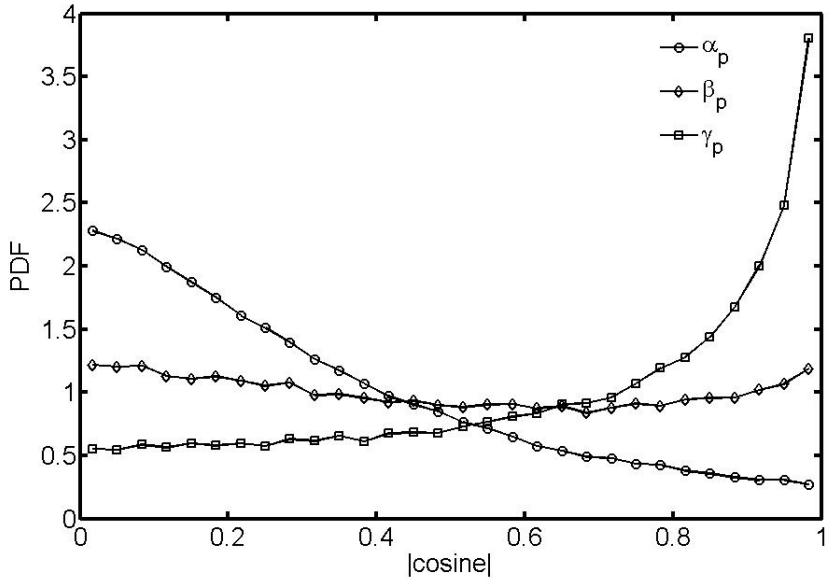

(a)

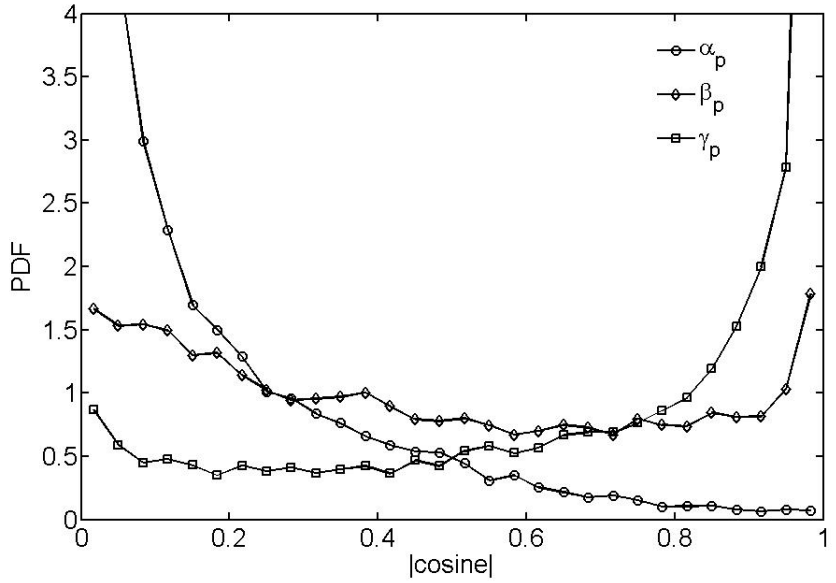

(b)

Fig. 18. PDF of cosine of the angle between vorticity vector and pressure Hessian eigenvectors in (a) DNS of incompressible isotropic turbulence, and (b) EHEE simulation at $M_M = 0.01$.

one of the eigenvectors of the pressure Hessian tensor. This behavior is observed in DNS of incompressible turbulence as well. In Figure 18(a), we present the PDFs of the cosine of angle between the vorticity vector and the eigenvectors corresponding to the eigenvalues (α_p, β_p, γ_p) of the pressure Hessian tensor as seen in DNS. Note that $|\alpha_p| \geq |\beta_p| \geq |\gamma_p|$ [45]. In Figure 18(b) we present the alignment tendency of the vorticity vector with the anisotropic portion of the pressure Hessian tensor (Q_{ij}) seen in EHEE model. Similar to the behavior seen in Figure 18(a), the vorticity vector shows high propensity to align with the γ_p eigenvector of the Q_{ij} tensor.

We further evaluate the model in terms of the joint statistics of the second (q) and third (r) invariants of the normalized velocity gradient tensor. For incompressible turbulence these invariants are defined as in (2.8). Knowledge about velocity gradient invariants can be employed to infer the local topology of a flow field [11]. In Figures 19(a) and 19(b) we present the joint PDFs of q and r as seen in DNS and EHEE computations. The distribution in Figure 19(a) has two prominent features: (i) a significant amount of data lies in the lower right region along the curve $q = \sqrt[3]{27r^2/4}$ (Vieillefosse line); and (ii) the bulk of data lies almost uniformly distributed over a roughly elliptical region in the upper left quadrant. The local topologies associated with these regions are stable-focus-stretching (lower-right) and unstable node-saddle-saddle (upper-left). These features are found to be quite universal across a variety of incompressible turbulent flows ([12] – [22]). A close inspection of Figure 19(b) reveals that the EHEE model does not capture the details of the distribution very accurately. However, the model clearly recovers the preferred alignment of the joint distribution along the Vieillefosse line.

Based on the foregoing discussion, we summarize that at a small enough Mach number ($M_M = 0.01$), the EHEE model recovers several features seen in DNS of incompressible turbulence. Moreover, unlike the HEE model developed in Chapter

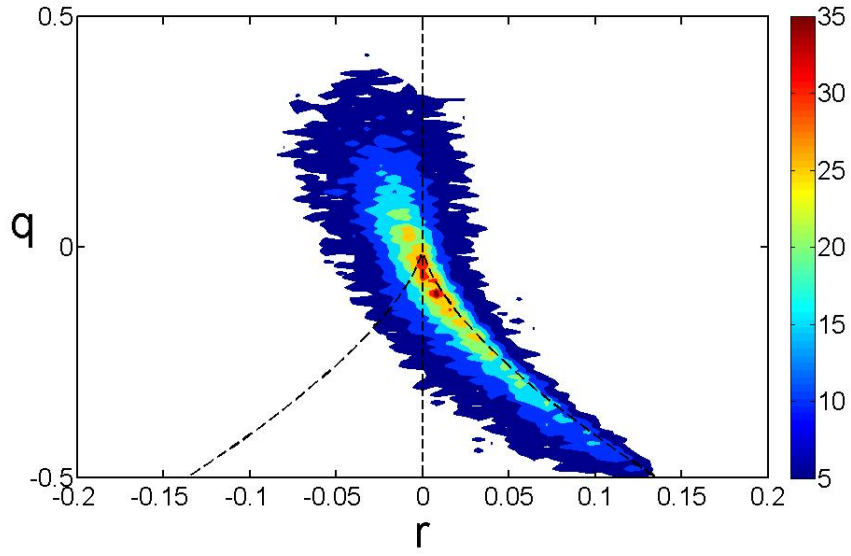

(a)

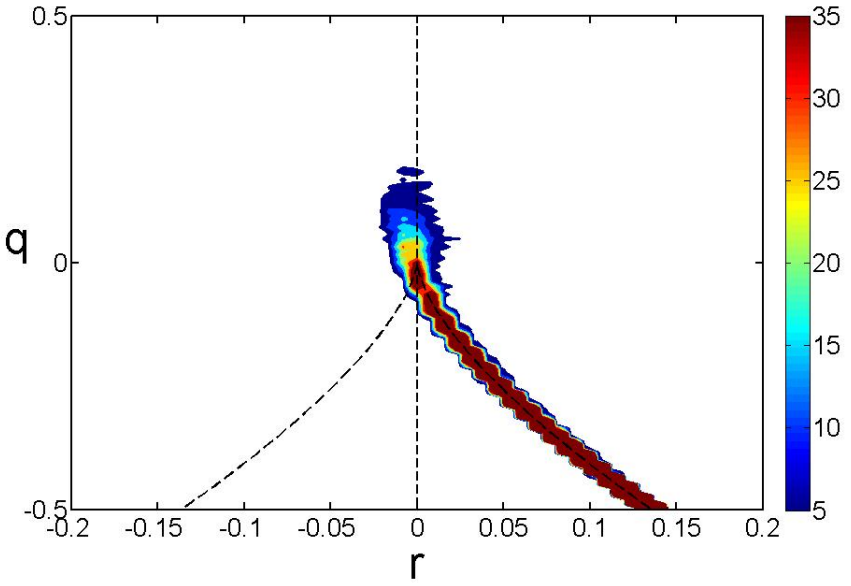

(b)

Fig. 19. Joint PDF of second and third invariants (q, r) of normalized velocity gradient tensor in (a) DNS of incompressible isotropic turbulence, and (b) EHEE simulation at $M_M = 0.01$.

III, the recovery of the incompressible behavior in the EHEE model is not conditional upon the instantaneous value of normalized dilatation. This is a major improvement achieved by the EHEE model.

2. Evaluation at high Mach number: Pressure released limit

In this sub-section, we evaluate the model performance in an extremely high Mach number regime. This regime can also be considered as the pressure-released limit, wherein pressure has negligible influence on the flow field. Bikkani et al. [39] study the evolution of velocity gradient dynamics in such a regime using the Burgers equation. Their study can be considered as the exact pressure released behavior of turbulence, as pressure terms are completely removed from the governing equations. Thus, we will evaluate the EHEE results in high Mach number limit against the results of Bikkani et al. [39].

To simulate the high Mach number behavior, we choose initial $M_M = 10000$. Though this number is too high from a practical viewpoint, nevertheless it is useful to demonstrate the asymptotic ability of the EHEE model to recover pressure-released behavior. As pointed out in Section A, the initial values of the isotropic (Z) and the anisotropic (Q_{ij}) parts of the pressure Hessian terms must be chosen consistent with the simulated high Mach number regime. A simple non-dimensional analysis of the Navier–Stokes equation [59] clearly suggests that at very high Mach numbers the pressure terms scale as $1/(M_a)^2$ of inertia terms, where M_a is the ratio between the relevant acoustic and inertial time scales. Accordingly, in our EHEE simulation we choose the initial values Z and $\sqrt{Q_{mn}Q_{mn}}$ as:

$$\begin{aligned} |Z| &\sim \frac{|A_{lm}A_{ml}|}{(M_M)^2}; \\ \sqrt{Q_{mn}Q_{mn}} &\sim \frac{|A_{lm}A_{ml}|}{(M_M)^2}. \end{aligned} \tag{4.51}$$

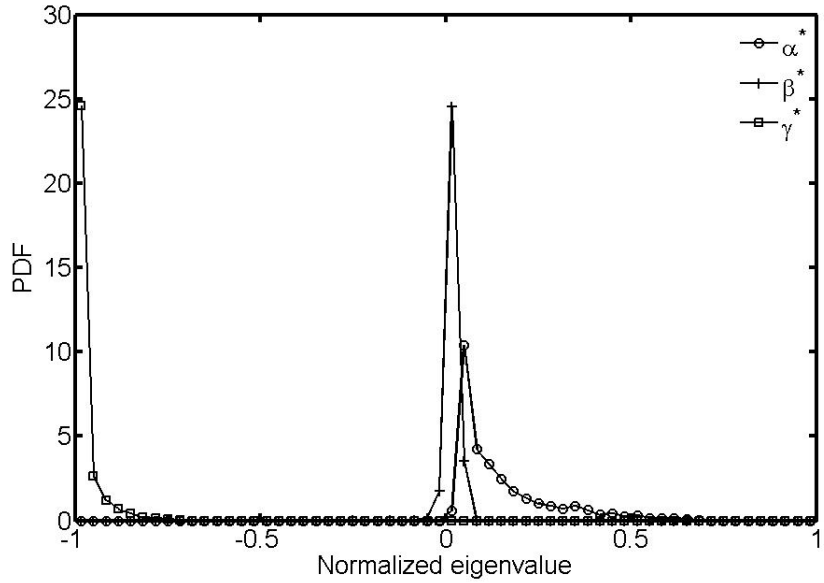

(a)

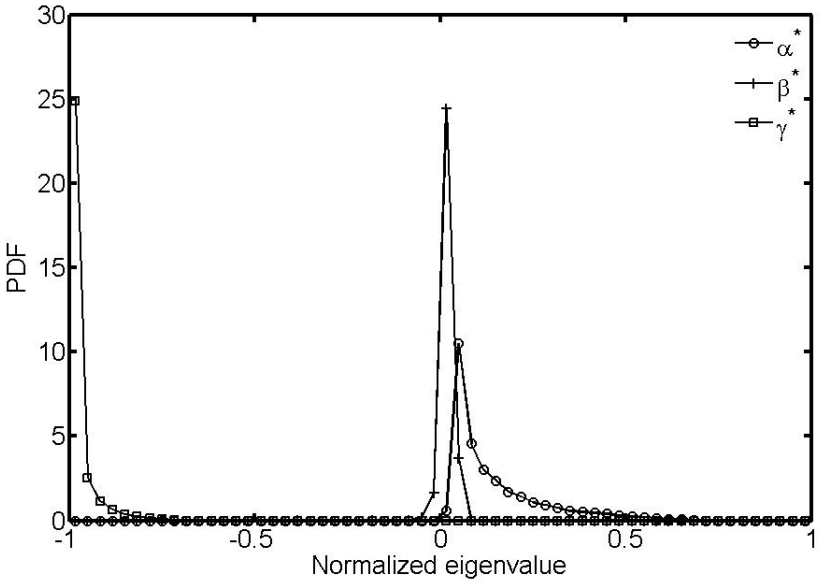

(b)

Fig. 20. PDF of strain-rate eigenvalues for particles undergoing gradient steepening (velocity gradient magnitude 10 times the initial value) in (a) Burgers velocity gradient dynamics, and (b) EHEE simulation at $M_M = 10000$.

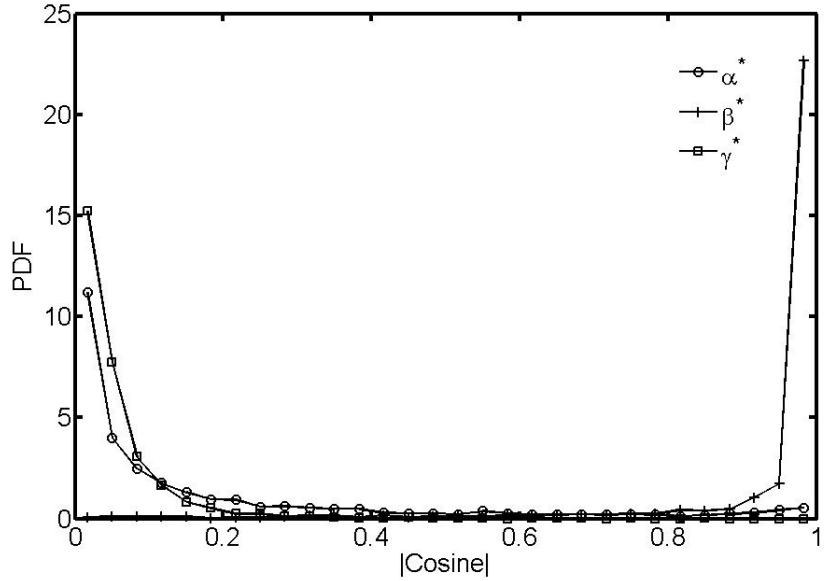

(a)

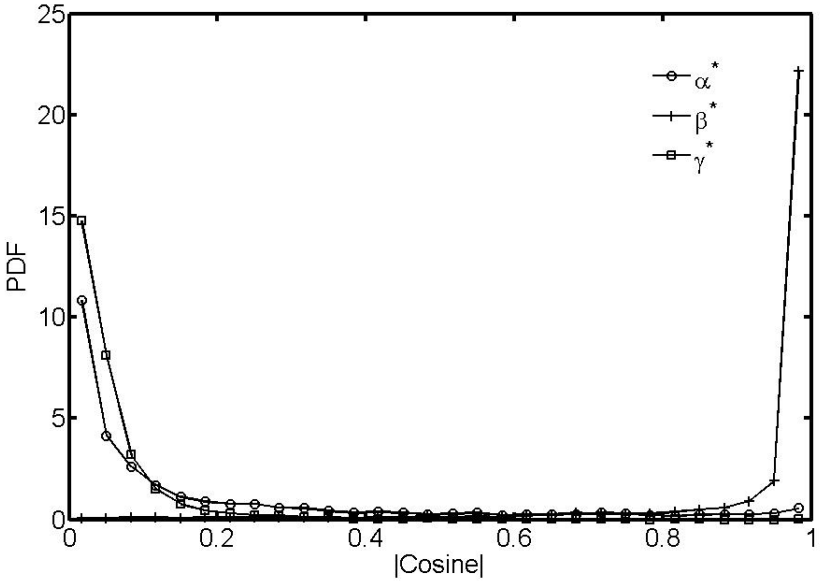

(b)

Fig. 21. PDF of cosine of angle between vorticity vector and strain-rate eigenvectors for particles undergoing gradient steepening (velocity gradient magnitude 10 times the initial value) in (a) Burgers velocity gradient dynamics, and (b) EHEE simulation at $M_M = 10000$.

Moreover, as the analysis of Bikkani et al. [39] assumes inviscid dynamics, we set τ_v (and τ_p) to be infinity (very large number) in our simulations. This removes the influence of viscosity terms in the EHEE model (4.31) – (4.36). The value of sound speed (c) is set to a low value of 0.0001 to achieve an initial Mach number (M_M) of 10000. The initial values of all other quantities are chosen to be the same as described in Sub-section 1 for the incompressible limit simulation.

Computations and analysis of Bikkani et al. [39] show that the pressure-released turbulence has bimodal behavior. In their computations, approximately 70% of the particles undergo gradient steepening, and the other 30% undergo gradient smoothening. The velocity gradient structures associated with these two modes of behavior are vastly different from each other. Again, we study the structure of the velocity gradient tensor in terms of the PDFs of strain-rate eigenvalues and cosines of the angles between the vorticity vector and strain-rate eigenvectors. In Figures 20(a) and 21(a), we present the PDFs of the normalized strain-rate eigenvalues (4.50) and the cosine of the angle between the vorticity vector and the strain-rate eigenvectors for the particles undergoing gradient steepening (results sampled at an instant when $\sqrt{A_{mn}A_{mn}}$ reaches 10 times its initial value). In Figures 22(a) and 23(a) we present results from Burgers dynamics for particles undergoing gradient smoothening (results sampled at an instant when $\sqrt{A_{mn}A_{mn}}$ reaches one-tenth of its initial value). These PDFs clearly show the tendency of Burgers dynamics to approach the stable fixed points of the inviscid Burgers velocity gradient dynamics [39]. In Figures 20(b), 21(b), 22(b) and 23(b) we present the corresponding results obtained with the EHEE model in high Mach number limit. The EHEE results in these figures are in complete agreement with those of Burgers dynamics. Moreover, in EHEE simulations we find that the ratio of the number of particles undergoing gradient steepening to that undergoing gradient smoothening is indeed 70 : 30, which is the same as observed in

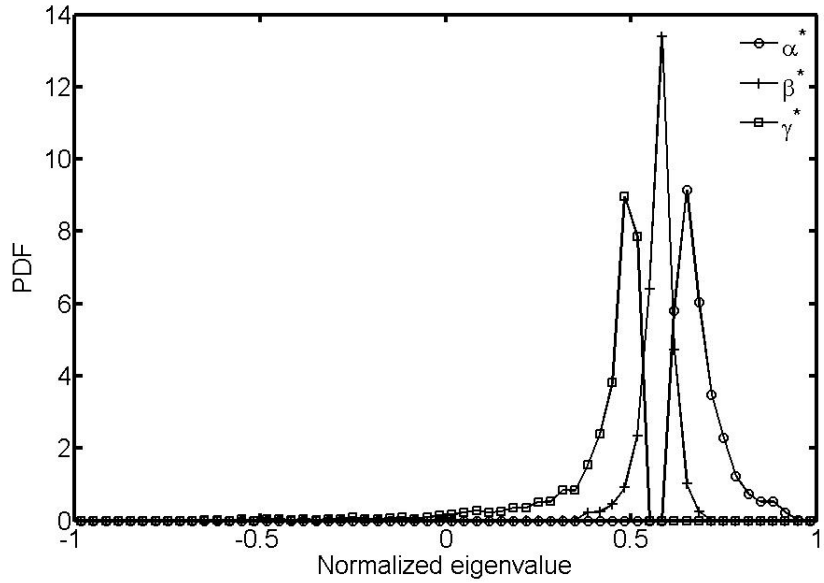

(a)

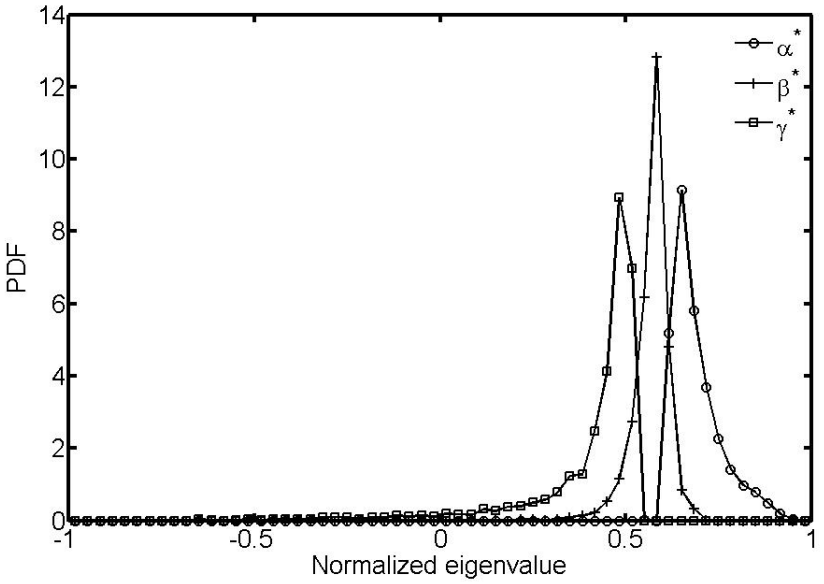

(b)

Fig. 22. PDF of strain-rate eigenvalues for particles undergoing gradient smoothening (velocity gradient magnitude one-tenth of the initial value) in (a) Burgers velocity gradient dynamics, and (b) EHEE simulation at $M_M = 10000$.

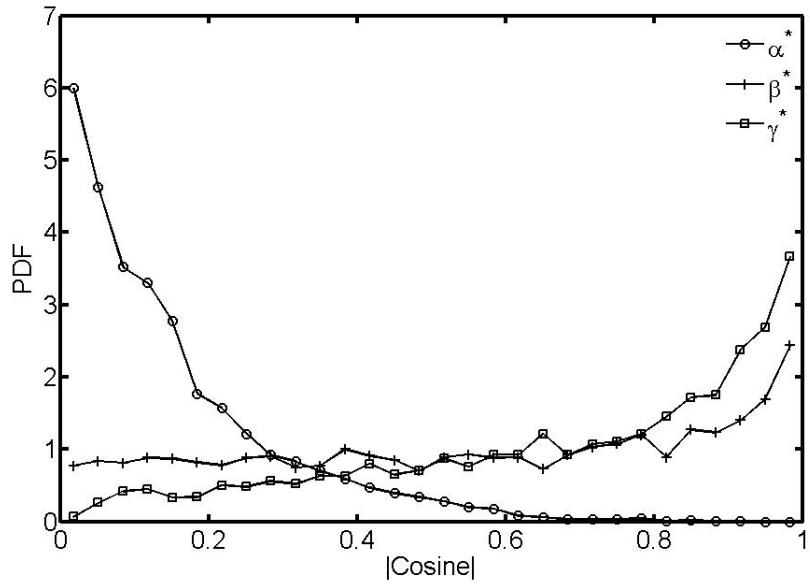

(a)

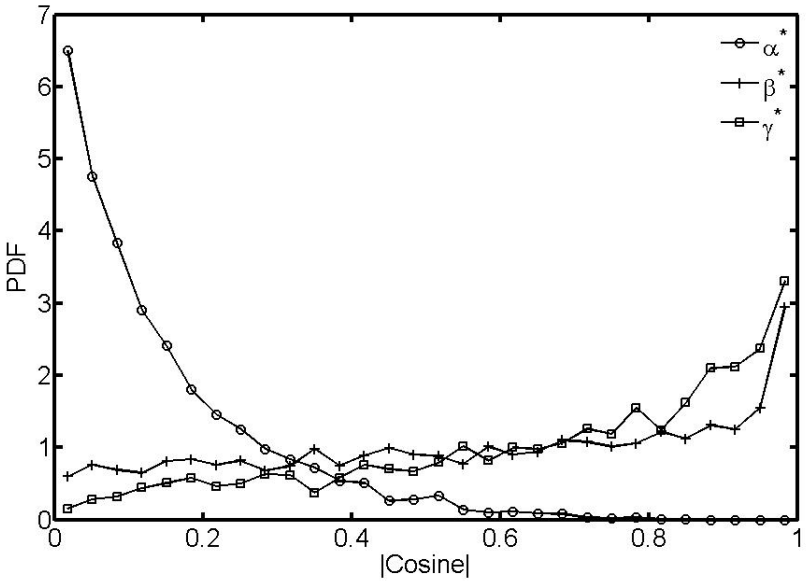

(b)

Fig. 23. PDF of cosine of angle between vorticity vector and strain-rate eigenvectors for particles undergoing gradient smoothening (velocity gradient magnitude one-tenth of the initial value) in (a) Burgers velocity gradient dynamics, and (b) EHEE simulation at $M_M = 10000$.

Burgers dynamics by Bikkani et al. [39]. Thus, we conclude that at an extremely high Mach number, EHEE exactly recovers the pressure-released behavior of compressible velocity gradient dynamics.

3. Evaluation at intermediate Mach numbers

In this sub-section, we evaluate the performance of the EHEE model at moderate subsonic Mach numbers. A series of comparisons is performed against DNS results of compressible decaying isotropic turbulence [51, 50, 38]. Specifically, we evaluate the model in terms of the influence of Mach number on the statistics of (i) vorticity (ω_i), and (ii) dilatation (A_{ii}). EHEE computations are performed at three representative initial Mach numbers: $M_M = 0.1$, 0.2, and 0.3. These values are chosen to have a reasonable comparison with the available DNS results of compressible turbulence, which employ turbulent Mach number as parameter (see 4.47). We restrict our comparisons over a low sub-sonic Mach number regime, as considerable understanding and significant volume of DNS studies are available in this regime. For the EHEE simulation results presented in this sub-section, a desired value of initial M_M is achieved by appropriately choosing a value for sound speed, c (see 4.45). Initial values of the pressure Hessian components are chosen such that $\phi \approx 0.01$ and $\psi \approx 0.01$ (see definitions in (4.45)). The value of τ_v is chosen to achieve a desired value of Re_M. For all the EHEE simulations discussed in this section, Re_M is chosen to be 35.4 (unless specified otherwise). Note that these values are chosen to match the initial conditions specified in [51] and [38].

a. Effect of Mach number on solenoidal and compressible dissipation

In homogeneous turbulence, the root mean square (rms) of vorticity and dilatation are proportional to solenoidal dissipation (ϵ_S) and compressible dissipation (ϵ_C) of

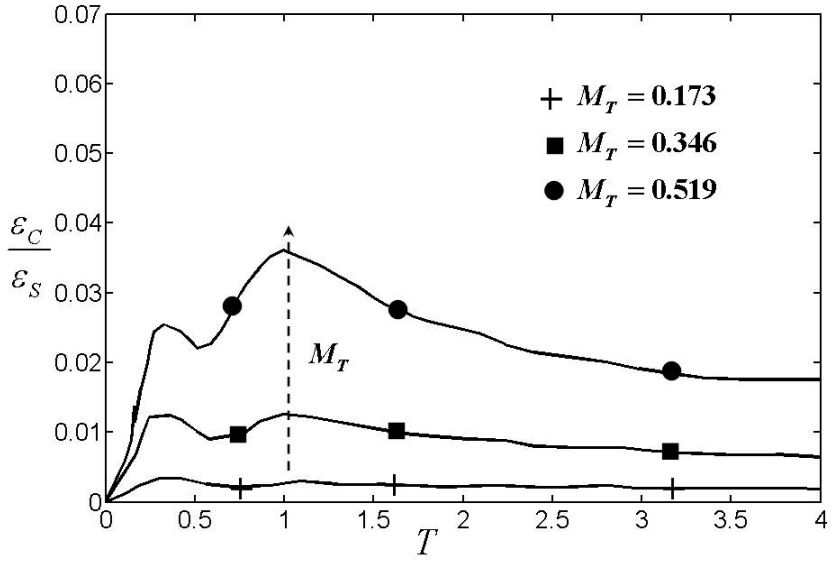

(a)

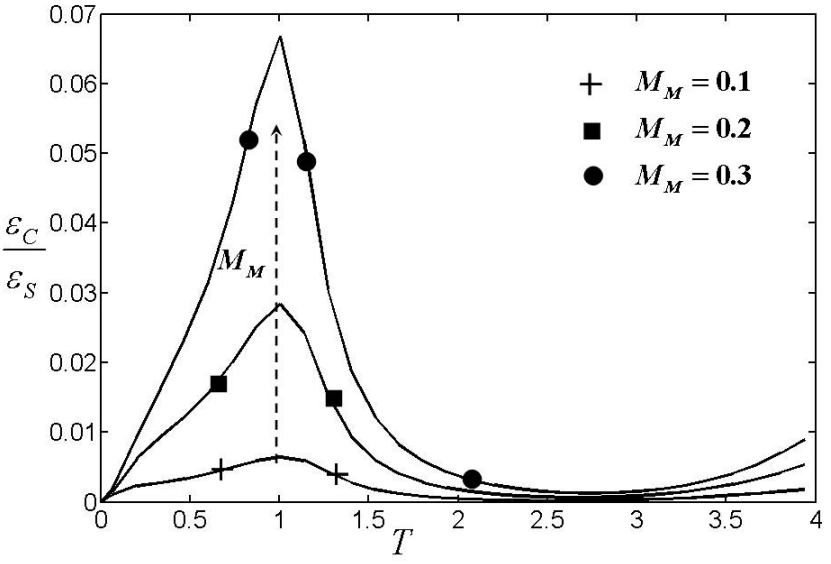

(b)

Fig. 24. Effect of Mach number on the time evolution of ϵ_C/ϵ_S in (a) DNS of compressible isotropic turbulence, (b) EHEE simulations.

turbulent kinetic energy [50]:

$$\epsilon_S = \frac{\mu}{\langle\rho\rangle}\left\langle\omega_i^{'}\omega_i^{'}\right\rangle; \tag{4.52}$$

$$\epsilon_C = \frac{4\langle\mu\rangle}{3\langle\rho\rangle}\left\langle d^{'2}\right\rangle \tag{4.53}$$

where μ and ρ denote dynamic viscosity and density and $d \equiv A_{ii}$. ($\langle\zeta\rangle$, $\zeta^{'}$ denote Reynolds mean and fluctuation of any flow variable ζ).

Theoretical analysis and computational results of homogeneous isotropic compressible turbulence [50, 51, 38] show that in low sub-sonic Mach number regime the effect of Mach number on solenoidal dissipation is negligible. On the other hand, compressible dissipation (ϵ_C) shows a strong dependence on turbulent Mach number [50]. In Figure 24(a)* we present evolution of the ratio, ϵ_C/ϵ_S seen in DNS of Lee et al. [51] with an initial turbulent Mach number as the parameter. The figure clearly demonstrates that an increase in Mach number increases ϵ_C/ϵ_S, or equivalently $\left\langle d^{'}d^{'}\right\rangle / \left\langle\omega_i^{'}\omega_i^{'}\right\rangle$ (see definitions in 4.53). Theoretical analysis of Sarkar et al. [50] estimates that ϵ_C tends toward a quasi-equilibrium value with respect to ϵ_S with turbulent Mach number (M_T) as a scaling factor:

$$\epsilon_C \propto M_T^2 \epsilon_S. \tag{4.54}$$

With $\langle\mu\rangle$ and $\langle\rho\rangle$ being constants for homogeneous turbulence, (4.54) is essentially a relationship between the rms values of vorticity and dilatations:

$$\left\langle d^{'}d^{'}\right\rangle = \eta M_T^2 \left\langle\omega_i^{'}\omega_i^{'}\right\rangle \tag{4.55}$$

where η is a constant. In Figure 25(a) we plot the results presented in Figure 24(a)

*Reprinted with permission from [51]. Copyright[1991], American Institute of Physics.

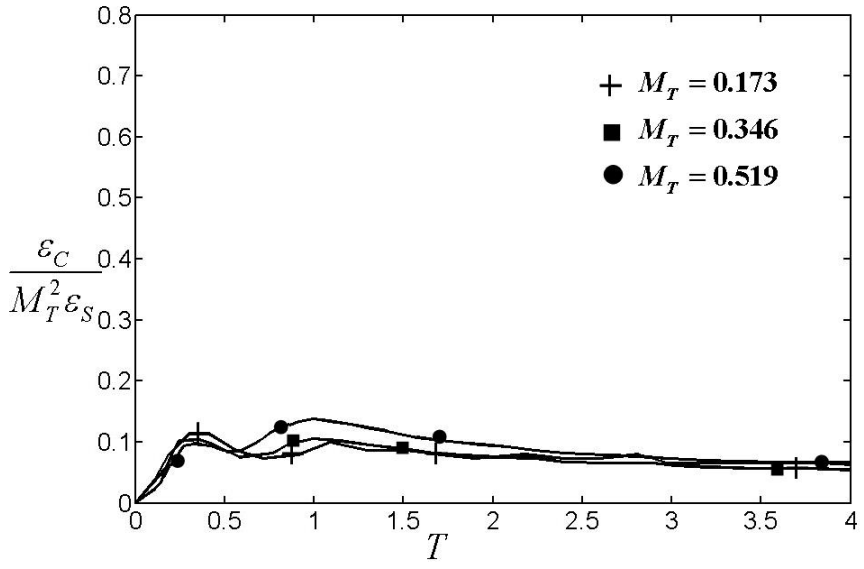

(a)

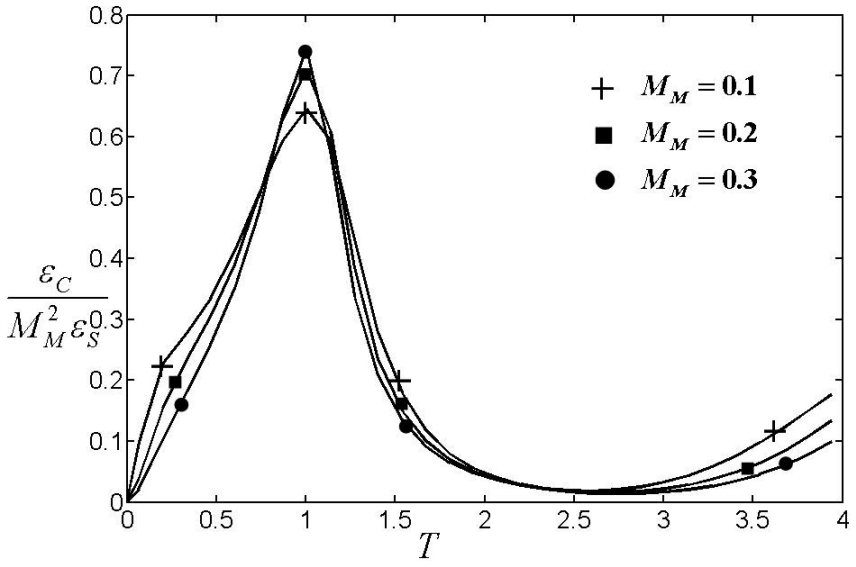

(b)

Fig. 25. Effect of Mach number on the time evolution of ϵ_C/ϵ_S normalized by the initial value of Mach number in (a) DNS of compressible isotropic turbulence, and (b) in EHEE simulations.

normalized by the initial value $(M_T)^2$. Indeed, with this normalization all the curves collapse representing the existence of $(M_T)^2$ scaling suggested by Sarkar et al. (4.54). Note that in Figures 24(a) and 25(a), time on the x-axis has been re-normalized (to a new time variable T) as compared to the original presentation of Lee et al. [51]. Lee et al. [51] present the results over a defined acoustic time scale. The value of this time scale at the instant when ϵ_C/ϵ_S attains its maxima (approximately the same for all Mach number simulations) is used to renormalize the time axis in Figures 24(a) and 25(a).

We now consider EHEE results and qualitatively examine them with respect to the DNS behavior discussed above. In Figure 26 we present the evolution of $\langle \omega_i' \omega_i' \rangle$ (equivalent to ϵ_S) computed with the EHEE model. Clearly, the model qualitatively recovers the behavior seen in DNS: initial Mach number has negligible influence on $\langle \omega_i' \omega_i' \rangle$. In Figure 24(b) we present the evolution of $\langle d' d' \rangle / \langle \omega_i' \omega_i' \rangle$ (equivalent to ϵ_C/ϵ_S) from EHEE computations. Similar to the trend seen in DNS (Figure 24(a)), an increase in Mach number significantly increases the value of $\langle d' d' \rangle / \langle \omega_i' \omega_i' \rangle$ in the EHEE simulations as well. Furthermore, we check to see if the EHEE model recovers the Mach number scaling (4.55). In Figure 25(b), we plot $\langle d' d' \rangle / \langle \omega_i' \omega_i' \rangle$ compensated by $(M_M)^2$. Indeed, this compensation makes the curves collapse together. This is in agreement with the behavior seen in DNS (Figure 25(a)).

b. Effect of Mach number on skewness and flatness of vorticity and dilatation

We further evaluate the model in terms of higher order moments – skewness and flatness – of vorticity and dilatation PDFs. Skewness (S_ζ) and flatness (F_ζ) for any

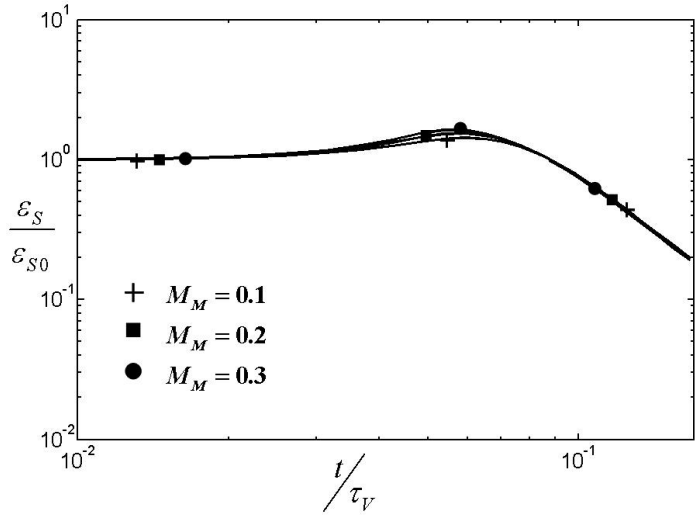

Fig. 26. Effect of Mach number on the time evolution of solenoidal dissipation rate (ϵ_S) in EHEE simulations.

variable ζ are defined as:

$$S_\zeta \equiv \frac{\langle \zeta'^3 \rangle}{\langle \zeta'^2 \rangle^{3/2}}; \qquad F_\zeta \equiv \frac{\langle \zeta'^4 \rangle}{\langle \zeta'^2 \rangle^2}. \tag{4.56}$$

The DNS study of Lee et al. [51] suggests that skewness and flatness of each component of vorticity vector in homogeneous isotropic turbulence is very similar to those of a Gaussian distribution. Thus $S_{\omega_i} \approx 0$, and $F_{\omega_i} \approx 3$. Furthermore, both S_{ω_i} and F_{ω_i} remain unchanged as the Mach number increases. On the other hand, skewness and flatness of dilatation (S_d, F_d) are highly dependent on Mach number. Both S_d and F_d show significant departure from the Gaussian distribution as Mach number increases. At non-zero Mach numbers, compression events are more favored than expansions leading to negative S_d values. Also, dilatation has a considerably flatter distribution resulting in F_d being greater than that of Gaussian distribution. Furthermore, as

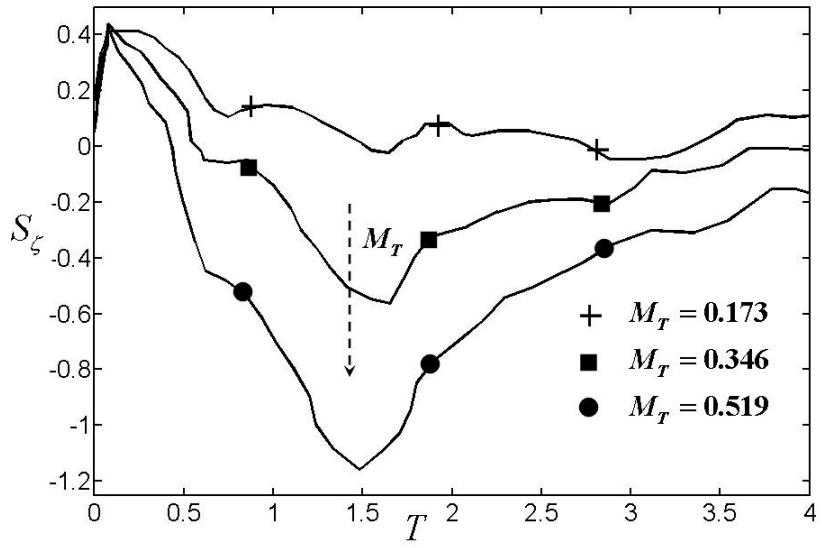

(a)

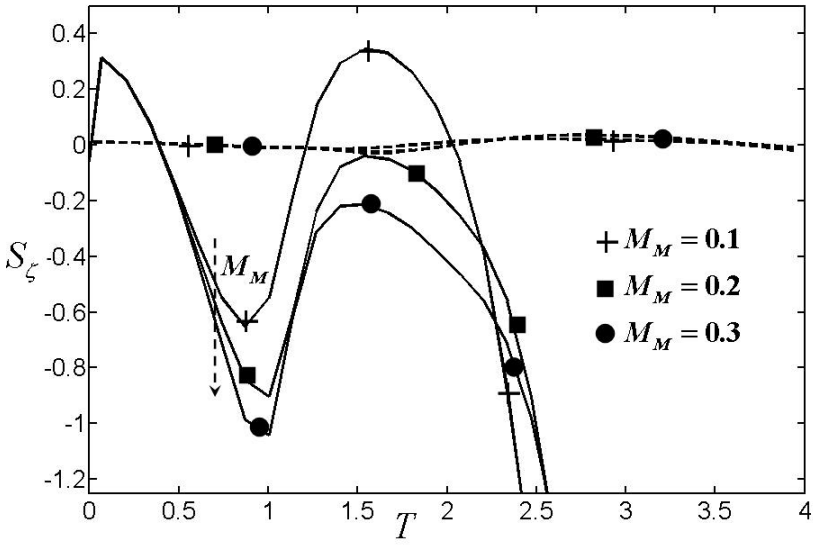

(b)

Fig. 27. Effect of Mach number on time evolution of skewness of dilatation (A_{ii}) in (a) DNS of compressible isotropic turbulence, and (b) EHEE simulations. The dashed curves in (b) represent skewness of vorticity (ω_i).

Mach number increases, dilatation distribution gets more negatively skewed, and the flatness of dilatation further increases. These findings of Lee et al. [51] are reproduced in Figures 27(a)* and 28(a)* in re-normalized time, T.

To examine the corresponding EHEE performance, we present the model results in Figures 27(b) and 28(b). The dashed curves represent the time evolution of skewness and flatness of vorticity in Figures 27(b) and 28(b), respectively. We observe that indeed a change in Mach number influences neither skewness nor flatness of vorticity (curves corresponding to different Mach numbers overlap). This is in line with expected behavior. Furthermore, at initial times ($T \leq 1.5$), the skewness and flatness at all Mach numbers are indeed close to those of Gaussian distribution ($S_{\omega_i} = 0$, $F_{\omega_i} = 3$). However, at later times the flatness evolutions become erratic and the model computations show no qualitative agreement with the DNS results.

The solid curves in Figures 27(b) and 28(b) represent the skewness and flatness of the dilatation PDF. The facts that the dilatation PDF in compressible turbulence has negative skewness and a flatness value more than that of a Gaussian distribution are very well captured by the EHEE model. Moreover, the model correctly recovers the following trends: (i) skewness becomes increasingly more negative, and (ii) flatness becomes increasingly more positive with an increase in the Mach number. At earlier times ($T \leq 1.5$), the behavior shown in EHEE computations is indeed very similar to that seen in DNS. However, at later times, like vorticity, the model performance deteriorates as evolutions of both S_d and F_d become erratic. The inconsistent behavior of statistics at these late times may be due to the neglected dilatation related viscous effects in the EHEE model (4.25).

---

*Reprinted with permission from [51]. Copyright[1991], American Institute of Physics.

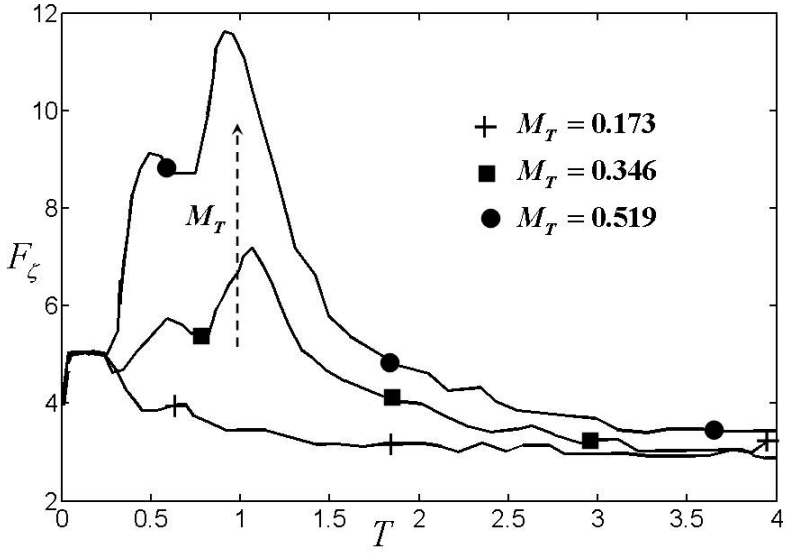

(a)

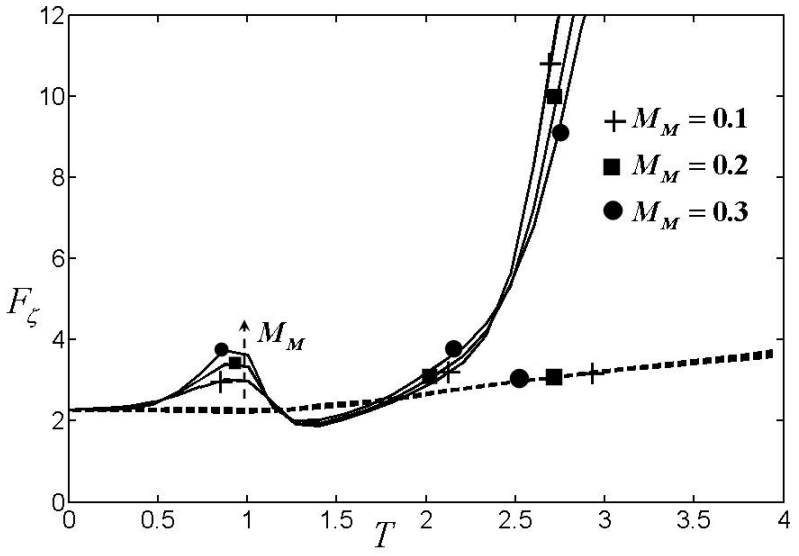

(b)

Fig. 28. Effect of Mach number on time evolution of flatness of dilatation (A_{ii}) in (a) DNS of compressible isotropic turbulence, and (b) EHEE simulations. The dashed curves in (b) represent flatness of vorticity (ω_i).

4. Evaluation in terms of Reynolds number effects

A well-known effect of a decreased Reynolds number on turbulence is to inhibit the process of velocity gradient steepening. Consequently, kinetic energy dissipation, ϵ ($\equiv (\epsilon_S + \epsilon_C)$) decreases with decreased Reynolds number. Lee et al. [51] further demonstrate that a reduction in Reynolds number causes a decrease in magnitudes of skewness (S_d) and flatness (F_d) of the dilatation PDF. In Figures 29(a), 29(b), and 29(c), we demonstrate the capability of the EHEE model in capturing these effects. In each of these figures, results have been shown from two different simulations. These simulations differ only in terms of the value of τ_v or, equivalently, the effective Reynolds number (see Section A, (4.45)). In Figure 29(a), we show the evolution of ϵ. A reduction in τ_v clearly reduces dissipation rate, ϵ. This is in line with the expected behavior. In Figures 29(b) and 29(c) we demonstrate the time evolution of skewness and flatness of dilatation. In both figures, the moderating effect of decreased Reynolds number is clearly seen. Based on these observations, we conclude that the EHEE model recovers the general effects of Reynolds number on compressible turbulence.

C. Conclusions

The recently developed dynamical model for compressible velocity gradient dynamics – homogenized Euler equation (HEE) – is enhanced further by (i) introducing an acoustic time scale to correctly capture the physics of dilatational portion of velocity gradient field, and (ii) adding viscosity terms to capture finite Reynolds number effects. These enhancements are necessary to address the shortcomings of the original HEE model. An acoustic time scale is introduced in the model by modifying the pressure Hessian evolution equation in the model. This modification brings in an explicit appearance of Mach number (ratio of acoustic and fluid velocity time scales)

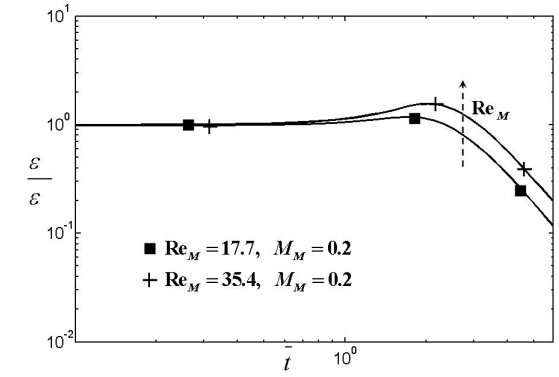

(a)

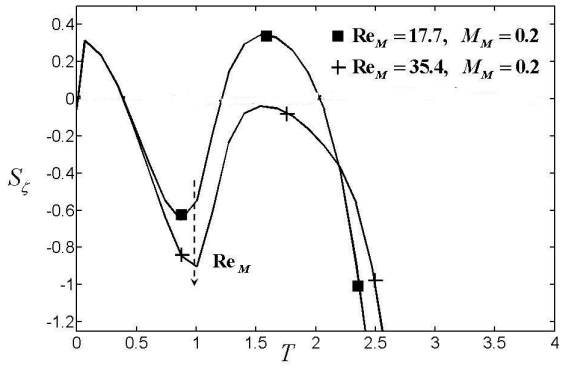

(b)

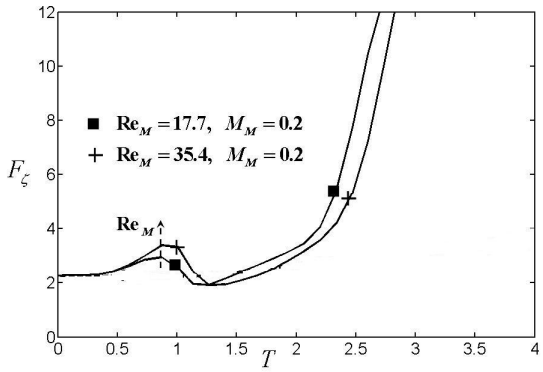

(c)

Fig. 29. Effect of Reynolds number on time evolution of (a) total dissipation rate ($\epsilon_S + \epsilon_C$), (b) skewness of dilatation (A_{ii}), and (c) flatness of dilatation in EHEE simulations.

in the model. Viscous effects are added to the model using the linear Lagrangian diffusion approximation, which has been earlier used in the context of the restricted Euler equation. Performance of this enhanced model – Enhanced HEE (EHEE) – is evaluated against direct numerical simulation (DNS) results. EHEE shows several improvements over its predecessor. At very low Mach numbers (incompressible limit) the model recovers several features seen in incompressible turbulence. In the very high Mach number limit, the model exactly recovers Burgers (pressure-released) velocity gradient behavior. At intermediate Mach numbers, the model accurately captures various Mach number effects on the statistics of both solenoidal and dilatational portions of the velocity gradient tensor as seen in DNS of compressible turbulence. Similarly, several Reynolds number effects on compressible velocity gradient physics are recovered by the model.

CHAPTER V

SUMMARY AND CONCLUSIONS

The overall goal of this dissertation is to further the current understanding of the effects of compressibility on turbulent velocity gradients. Toward this end this work (i) characterizes the effects of compressibility on turbulent velocity gradients employing direct numerical simulation (DNS) results, and (ii) develops mathematical models to compute the evolution of velocity gradients in compressible turbulence. The study of velocity gradients is key to understanding various non-linear processes of turbulence such as cascading, intermittency, mixing and material element deformation. Such understanding is imperative for the development of high fidelity turbulence closure models for compressible turbulence computations. A brief summary including the major conclusions/findings of this dissertation is presented below.

A. Effects of compressibility on velocity gradient invariants and local topology

In this part of the dissertation, dependence of joint statistics of second and third invariants of velocity gradient tensor on dilatation (degree of compression/expansion of a fluid element) in compressible decaying isotropic turbulence is examined using DNS results. Moreover, the exact probabilities of occurrence of various local flow patterns/topologies conditional upon dilatation are computed. The study reveals that the joint statistics of the second and third invariants are highly dependent on normalized dilatation. Invariant statistics conditioned upon zero dilatation are very similar to the behavior seen in incompressible turbulence but change drastically as dilatation assumes higher positive/negative values. It is found that at high positive and negative dilatations, the dominant topologies are entirely different from those seen in incompressible turbulence. While unstable focus stretching and unstable node/unstable

node/unstable node dominate at high positive dilatations, stable focus compressing and stable node/stable node/stable node topologies are dominant at large negative dilatations. As the extreme levels of normalized dilatations are reached ($\pm\sqrt{3}$), the variety in the observed flow patterns is further reduced. The only observed flow pattern at $\sqrt{3}$ and $-\sqrt{3}$ is unstable star node/unstable star node/unstable star node and stable star node/stable star node/stable star node, respectively. Furthermore, it is found that the conditional behavior of invariants is insensitive to Reynolds number and Mach number (at least in the considered range). Additionally, in this part of the dissertation, the above-mentioned findings are employed to evaluate the performance of a recently developed velocity gradient model – homogenized Euler equation (HEE). It is found that the HEE model qualitatively captures many features seen in DNS. However, the quantitative performance is not very accurate, especially at negative dilatation values.

B. Development of models for compressible velocity gradient dynamics

In the second part of the dissertation, two mathematical models for compressible velocity gradient dynamics are developed. The first model - called the homogenized Euler equation (HEE) - ignores all the non-local effects and is developed under the assumptions of uniform velocity gradients in an inviscid compressible and homentropic flow field. The medium is assumed to be a calorically perfect gas. Coupling between the energy and momentum equation is invoked through the state and energy equations. The pressure Hessian evolves as dictated by thermodynamic considerations. In contrast to the restricted Euler equation (REE), the anisotropic pressure Hessian effects are retained to some level of accuracy in this approach. Computations are performed for an ensemble of random initial velocity gradient tensors. Various

statistics pertaining to the structure of the velocity gradient tensor conditioned upon normalized dilatation are studied. HEE results in the incompressible limit (statistics conditioned on zero dilatation) compare very well against DNS results of incompressible decaying isotropic turbulence. Moreover, in this limit the HEE computations are much improved over the asymptotic REE results. At various non-zero dilatations, the HEE very well captures many features of the principal strain-rate statistics seen in compressible DNS. The asymptotic behavior of HEE is consistent with Burgers velocity gradient dynamics. Despite its excellent performance in capturing several dilatation-conditioned statistics, the HEE model suffers from two important shortcomings. First, the model does not capture the time evolution of dilatation accurately. Second, in the absence of viscous terms, the HEE model fails to correctly recover the magnitudes of velocity gradients.

To address the shortcomings of the HEE model, a second model called the enhanced homogenized Euler equation (EHEE) is developed. In the EHEE model, several non-local pressure and viscous effects are included. The specific enhancements introduced in the EHEE model are: (i) introduction of an acoustic time scale to correctly capture the physics of the dilatational portion of velocity gradient field; and (ii) addition of viscosity effects. An acoustic time scale is introduced in the model by enhancing the existing pressure Hessian evolution equation of the HEE model. This modification brings an explicit appearance of Mach number (ratio of acoustic and fluid time scales) in the EHEE model. Viscous effects are added to the model using the linear Lagrangian diffusion approximation, which has been earlier used in context of the restricted Euler equation. Performance of the enhanced model is evaluated against a range of known turbulence behavior. EHEE shows several improvements over its predecessor. At very low Mach numbers (incompressible limit) the model recovers several features seen in incompressible turbulence. In the very high Mach

number limit, the model exactly recovers Burgers (pressure-released) velocity gradient behavior. At intermediate Mach numbers, the model accurately captures various Mach number effects on the statistics of both solenoidal and dilatational portions of the velocity gradient tensor as seen in DNS of compressible turbulence. Similarly, the model recovers several Reynolds number effects on compressible velocity gradient physics.

REFERENCES

[1] A.E. Perry, and M.S. Chong, *A description of eddying motion and flow patterns using critical point concepts*, Ann. Rev. Fluid Mech. 19 (1987), pp. 125–154.

[2] J.C.R. Hunt, A.A. Wray, and P. Moin, Eddies, stream, and convergence zones in turbulent flows; Center for Turbulence Research Report CTR-S88 1988.

[3] J. Jeong, and F. Hussain, *On the identification of a vortex*, J. Fluid Mech. 285 (1995), pp. 69–94.

[4] P. Vieillefosse, *Local interaction between vorticity and shear in a perfect incompressible fluid*, J. Phys. (Paris) 43 (1982), pp. 837–842.

[5] W.T. Ashurst, A.R. Kerstein, R. Kerr, and C. Gibson, *Alignment of vorticity and scalar gradient with strain rate in simulated Navier–Stokes turbulence*, Phys. Fluids 30 (1987), pp. 2343–2353.

[6] Y. Li, and C. Meneveau, *Origin of Non-Gaussian statistics in hydrodynamic turbulence*, Phys. Lett. 95 (2005), pp. 164502–1 – 4.

[7] S. Girimaji, and C. Speziale, *A modified restricted Euler equation for turbulent flows with mean velocity gradients*, Phys. Fluids 7 (1995), pp. 1438–1446.

[8] B.W. Zeff, D.D. Lanterman, R. McAllister, R. Roy, E.J. Kostelich, and D.P. Lathrop, *Measuring intense rotation and dissipation in turbulent flows*, Nature 421 (2003), pp. 146–149.

[9] S. Girimaji, and S. Pope, *A diffusion model for velocity gradients in turbulence*, Phys. Fluids A 2 (1990), pp. 242–256.

[10] B.J. Delarue, and S.B. Pope, *Application of PDF methods to compressible turbulent flows*, Phys. Fluids 9 (1997), pp. 2704–2715.

[11] M.S. Chong, A.E. Perry, and B.J. Cantwell, *A general classification of three-dimensional flow fields*, Phys. Fluids A 2 (1990), pp. 765–777.

[12] J. Soria, R. Sondergaard, B.J. Cantwell, M.S. Chong, and A.E. Perry, *A study of the fine-scale motions of incompressible time-developing mixing layers*, Phys. Fluids 6 (1994), pp. 871–884.

[13] O.N. Boratav, and R.B. Pelz, *On the local topology evolution of a high-symmetry flow*, Phys. Fluids 7 (1995), pp. 1712–1731.

[14] J.M. Chacin, B.J. Cantwell, and S.J. Kline, *Study of turbulent boundary layer structure using the invariants of the velocity gradient tensor*, Experimental Thermal and Fluid Science 13 (1996), pp. 308–317.

[15] H.M. Blackburn, N.N. Mansour, and B.J. Cantwell, *Topology of fine scale motions in turbulent channel flow*, J. Fluid Mech. 310 (1996), pp. 269–292.

[16] C.B. daSilva, and J.C.F. Pereira, *Invariants of the velocity-gradient, rate-of-strain, and rate-of-rotation tensors across the turbulent/non-turbulent interface in jets*, Phys. Fluids 20 (2008), pp. 055101–1–055101–18.

[17] J. Soria, A. Ooi, and M. Chong, *Volume integrals of the Q–R invariants of the velocity gradient tensor in incompressible flows*, Fluid Dynamics Research 19 (1997), pp. 219–233.

[18] P. O'Neill, and J. Soria, *The relationship between the topological structures in turbulent flow and the distribution of a passive scalar with an imposed mean gradient*, Fluid Dynamics Research 36 (2004), pp. 107–120.

[19] H. Kobayashi, F. Ham, and X. Wu, *Application of a local SGS model based on coherent structures to complex geometries*, International Journal of Heat & Fluid Flow 29 (2008), pp. 640–653.

[20] J.H. Chen, B.J. Cantwell, and N.N. Mansour, The topology and vorticity dynamics of a 3-D plane compressible wake; Tenth Australian Fluid Mechanics Conference, University of Melbourne, 1989.

[21] B.J. Cantwell, G. Lewis, and J. Chen, Topology of 3-D variable density flows; Tenth Australian Fluid Mechanics Conference, University of Melbourne, 1989.

[22] J.H. Chen, M.S. Chong, J. Soria, R. Sondergaard, A.E. Perry, M. Rogers, R. Moser, and B.J. Cantwell, A study of the topology of dissipating motions in direct numerical simulations of time-developing compressible and incompressible mixing layers; Proceedings of the Center for Turbulence Research Summer Program CTR-S90.

[23] H. Maekawa, T. Hiyama, and Y. Matuso, *Study of the geometry of flow patterns in compressible isotropic turbulence*, JSME International Journal 42 (1999), pp. 336–343.

[24] H. Miura, *Analysis of vortex structures in compressible isotropic turbulence*, Computer Physics Communications 147 (2002), pp. 552–555.

[25] S. Pirozzoli, and F. Grasso, *Direct numerical simulations of isotropic compressible turbulence: Influence of compressibility on dynamics and structures*, Phys. Fluids 16 (2004), pp. 4386–4407.

[26] S. Suman, and S.S. Girimaji, *Homogenized Euler equation: A model for compressible velocity gradient dynamics*, J. Fluid Mech. 620 (2009), pp. 177–194.

[27] K. Lee, S.S. Girimaji, and J. Kerimo, *Effect of compressibility on velcoity gradients and small scale structure*, Journal of Turbulence 10 (2009), pp. 1–18.

[28] B. Cantwell, *Exact solution of a restricted Euler equation for the velocity gradient tensor*, Phys. Fluids A 4 (1992), pp. 782–792.

[29] B. Cantwell, *On the behavior of velocity gradient tensor invariants in direct numerical simulations of turbulence*, Phys. Fluids A 5 (1993), pp. 2008–2013.

[30] M. Chertkov, A. Pumir, and B. Shraiman, *Lagrangian tetrad dynamics and phenomenology of turbulence*, Phys. Fluids 11 (1999), pp. 2398–2410.

[31] E. Jeong, and S. Girimaji, *Velocity-gradient dynamics in turbulence: Effect of viscosity and forcing*, Theoretical and Computational Fluid Dynamics 16 (2003), pp. 421–432.

[32] L. Chevillard, and C. Meneveau, *Lagrangian dynamics and statistical geometric structure of turbulence*, Phys. Rev. Lett. 97 (2006), pp. 174501–1–174501–4.

[33] L. Biferale, L. Chevillard, C. Meneveau, and F. Toschi, *Multiscale model of gradient evolution in turbulent flows*, Phys. Rev. Lett. 99 (2007), pp. 214501–1–214501–4.

[34] L. Chevillard, C. Meneveau, L. Biferale, and F. Toschi, *Modeling the pressure Hessian and viscous Laplacian in turbulence: Comparisons with direct numerical simulation and implications on velocity gradient dynamics*, Phys. Fluids 20 (2008), pp. 101504–1–101504–15.

[35] K. Xu, Gas kinetic schemes for unsteady compressible flow simulation; Lecture series 29th Computational Fluid Dynamics, von Karman Institute for Fluid Dynamics, Belgium, February 1988.

[36] K. Xu, *A gas kinetic scheme for the Navier–Stokes equation and its connection with artificial dissipation and Godunov method*, Journal of Computational Physics 171 (2001), pp. 289–335.

[37] J. Kerimo, and S.S. Girimaji, *Boltzmann–BGK approach to simulating weakly compressible 3D turbulence: Comparison between lattice Boltzmann and gas kinetic methods*, Journal of Turbulence 8 (2007), pp. 1–16.

[38] K. Lee, *Heat release effects on decaying homogenous compressible turbulence*, Texas A&M University, 2008.

[39] R. Bikkani, and S.S. Girimaji, *Role of pressure in non-linear velocity gradient dynamics in turbulence*, Phys. Rev. E 75 (2007), pp. 036307–1–8.

[40] J. Martin, A. Ooi, M.S. Chong, and J. Soria, *Dynamics of the velocity gradient tensor invariants in isotropic turbulence*, Phys. Fluids 10 (1998), pp. 2336–2346.

[41] T. Passot, and E. Vzquez-Semadeni, *Density probability distribution in one-dimensional polytropic gas dynamics*, Phys. Rev. E 58 (1998), pp. 4501–4510,.

[42] M. Avellaneda, R. Ryan, and E. Weinan, *PDFs for velocity and velocity gradients in Burgers turbulence*, Phys. Fluids 7 (1995), pp. 3067–3071.

[43] J.P. Bouchaud, and M. Mzard, *Velocity fluctuations in forced Burgers turbulence*, Phys. Rev. E 54 (1996), pp. 5116–5121.

[44] S. Girimaji, and Y. Zhou, *Spectrum and energy transfer in steady Burgers turbulence*, Phys. Lett. A 202 (1995), pp. 1438–1446.

[45] K. Ohkitani, and S. Kishiba, *Non-local nature of vortex stretching in an inviscid fluid*, Phys. Fluids 7 (1995), pp. 411–421.

[46] C. Kalelkar, *Statistics of pressure fluctuations in decaying isotropic turbulence*, Phys. Rev. E 73 (2006), pp. 046301–1 – 10.

[47] J.R. Ristorcelli, and G.A. Blaisdell, *Consistent initial conditions for the DNS of compressible turbulence*, Phys. Fluids 9(1) (1997), pp. 4–6.

[48] G.A. Blaisdell, N.N. Mansour, and W.C. Reynolds, *Compressibility effects on the growth and structure of homogeneous turbulent shear flows*, J. Fluid Mech. 256 (1993).

[49] G. Erlebacher, M.Y. Hussaini, H.O. Kreiss, and S. Sarkar, *The analysis and simulation of compressible turbulence*, Theoretical and Computational Fluid Dynamics 2 (1990), pp. 73 – 95.

[50] S. Sarkar, G. Erlebacher, M. Hussaini, and H.O. Kreiss, *The analysis and modelling of dilatational terms in compressible turbulence*, J. Fluid Mech. 227 (1991), pp. 473–493.

[51] S. Lee, S.K. Lele, and P. Moin, *Eddy shocklets in decaying compressible turbulence*, Phys. Fluids A 3 (1991), pp. 657–664.

[52] J.R. Ristorcelli, *A pseudo-sound constitutive relationship for the dilatational covariances in compressible turbulence*, J. Fluid Mech. 347 (1997b), pp. 37 – 70.

[53] L. Landau, and E. Lifshitz, Fluid mechanics, Pergamon Press, Oxford, 1985.

[54] K. Ohkitani, *Eigenvalue problems in 3D Euler flows*, Phys. Fluids A 5 (1993), pp. 2570–2572.

[55] F. White, Viscous fluid flow , McGraw Hill, Boston, 2006.

[56] A.N. Kolmogorov, *The local structure of turbulence in incompressible viscous fluid for very large Reynolds numbers*, Dokl. Akad. Nauk SSR 30 (1941), pp. 299–303.

[57] S.B. Pope, Turbulent flows, Cambridge University Press, Cambridge, 2000.

[58] T. Passot, and A. Pouquet, *Numerical simulation of compressible homogenous flows in turbulent regime*, J. Fluid Mech. 181 (1987), pp. 441 – 466.

[59] J. D. Anderson, Hypersonic and high temperature gas dynamics, McGraw-Hill, Boston, 1998.

VITA

Sawan Suman received his B. Tech. degree in aerospace engineering from the Indian Institute of Technology - Kanpur, India in 2001. Following that, he worked in the Indian aerospace industry for three years and joined Texas A&M University in 2004 to study turbulence theory and modeling. His research interests include turbulence processes, hypersonic flows, and Boltzmann based equations for fluid dynamics. He can be reached through Dr. Sharath S. Girimaji in the Aerospace Engineering Department at Texas A&M University, College Station, TX 77843-3141, or at sawan.suman@gmail.com.